Friedrich-Alexander-Universität
Faculty of Sciences

Master's Thesis

in Physics

Hydrodynamic Simulations of the Supernova Remnant Puppis A with PLUTO

Marie Prucker

Supervisor: Prof. Dr. Manami Sasaki

Dr. Karl-Remeis-Sternwarte, Astronomical Institute
Friedrich-Alexander-Universität Erlangen-Nürnberg

Submission date: 6th August 2025

Abstract

In this work, a hydrodynamical (HD) model setup for the Galactic core-collapse supernova remnant (SNR) Puppis A is developed, using the PLUTO code. Prior to the description of the HD model setup, the existing X-ray, radio and infrared observations of Puppis A are discussed to derive constraints for the model parameters and the structures of the ambient interstellar medium (ISM). Since Puppis A is known to have a very peculiar rectangular shape in X-rays, the main goal of the HD model is to reproduce the X-ray morphology of the remnant to gain insights on the explosion parameters and the structures in the ambient environment that are responsible for the appearance of Puppis A. The chosen model geometry is a spherical ejecta region surrounded by a higher density torus with an elliptical cross section representing an atomic/molecular cloud. Several different model geometries are tested, first in two-dimensional (2D) cylindrical geometry and subsequently in three-dimensional (3D) Cartesian geometry. The explored parameters are the ejecta mass, the vertical extent of the cloud, as well as the explosion energy, and the density of the ambient ISM. The simulations are directly compared to the observations by means of synthetic X-ray maps in the 0.3-10 keV band, as well as the distribution of emission measure with respect to ionisation timescale and electron temperature to quantitatively describe the plasma conditions. The best results with respect to reproducing the X-ray morphology, especially in the north-eastern part of Puppis A, and the plasma conditions are obtained by assuming an ejecta mass of $5\,M_\odot$ and a kinetic explosion energy of 1.5×10^{51} erg in the initial ejecta region with a radius of 2 pc. The cloud is described as a partial elliptical torus with an angular extent of $\theta = \frac{2}{3}\pi$ at a distance of 10 pc to the centre of the explosion, a vertical extent of 18 pc, and a density of $\sim 200\,\mathrm{cm}^{-3}$. Additionally, density clumping is introduced in the cloud, as well as in the ISM and ejecta. However, it has to be noted that the model is not able to reproduce the exact plasma conditions. The emission measure of the plasma is about two orders of magnitude lower compared to the observations, and a broader distribution in both ionisation timescale and electron temperature is found. For further comparison, the total X-ray spectrum of the remnant between 0.2-5 keV as seen with the eROSITA X-ray telescope is synthesised. The spectrum shows remarkable resemblance to the shape of the observed spectrum, especially at higher energies above 0.7 keV. Below 0.7 keV, an excess in the model spectrum is determined compared to the real data, which is mainly attributed to variations in the absorbing column density.

Contents

1. Introduction

"We are made of star stuff" - this famous quote by the American astronomer and science communicator Carl Sagan is often used in a romantic and almost philosophical way to describe the existence of human life in the entirety of the Universe. However, there is more truth to this statement than might be realised at first glance. What Carl Sagan tried to express in his popular science novel "Cosmos", published in 1980, is that all elements making up organic matter, besides hydrogen and helium, were at some point created within the interior of a dying star and would otherwise not exist.
The deaths of massive stars are among the most extreme and fascinating events in the Universe. They are initiated when a star at least 8 times more massive than the sun depletes the hydrogen it is burning in its core to produce energy and maintain hydrostatic equilibrium. This leads to the onset of a chain of nuclear fusion reactions and subsequently to the collapse of the star's core. In the process, all heavier elements, such as carbon, oxygen, and eventually iron are created. Ultimately, this results in a catastrophic explosion of the star, widely known as core collapse supernova (SN) (Vink, 2020). It should be mentioned that not all SNe result from the core collapse of massive stars. So-called thermonuclear SNe are believed to happen if a white dwarf, the final stage of stars lighter than $8\,M_\odot$, in a binary system accretes mass from its companion, which leads to the disruption of the WD (Seward and Charles, 2010a). However, this shall be discussed in further detail later on in this work.
Supernovae are highly energetic events, in which several solar masses ($M_\odot$) of matter, commonly referred to as ejecta, are expelled into the surrounding space. This includes all the heavier elements that were previously generated by fusion reactions within the star (Vink, 2020). In the explosion, not only matter but also radiation is released. For a few days to weeks, the light emitted by one such event is so bright that it outshines the entire host galaxy and if at close enough distances, is even visible to the naked eye (Seward and Charles, 2010a).
SNe can not only be observed at optical wavelengths, but across the entire electromagnetic spectrum. The same is true for what is left behind once the SN itself has faded: a so-called supernova remnant (SNR). SNRs are observable over several thousands of years and thereby allow to investigate the explosion mechanism of the preceding SN, the interaction of the ejecta with the surrounding interstellar medium (ISM), and on a larger scale the (chemical) enrichment of the ISM through SN feedback, which plays a crucial role in the evolution of galaxies as a whole (Vink, 2020).
A powerful tool to explore the characteristics of the SN progenitor, the explosion itself, and the ISM interacting with the remnant are numerical hydrodynamical simulations. If the model is able to reproduce the observables, it is possible to draw conclusions about parameters such as the initial ejecta mass, the explosion energy, and inhomogeneities in the ambient ISM. A well known example is Tycho's SNR, the remnant of a SN explosion observed in 1572 by the Danish astronomer Tycho Brahe. Today, the shock-heated ejecta are very bright in X-rays and show highly clumpy structures (see Fig. 1). Initially, it was not clear how these structures developed (Chandra X-ray Center, 2019). From three-

dimensional hydrodynamical simulations, it was concluded that the clumps most likely originate directly from the explosion and did not form during the remnant's evolution (Sato et al., 2019).

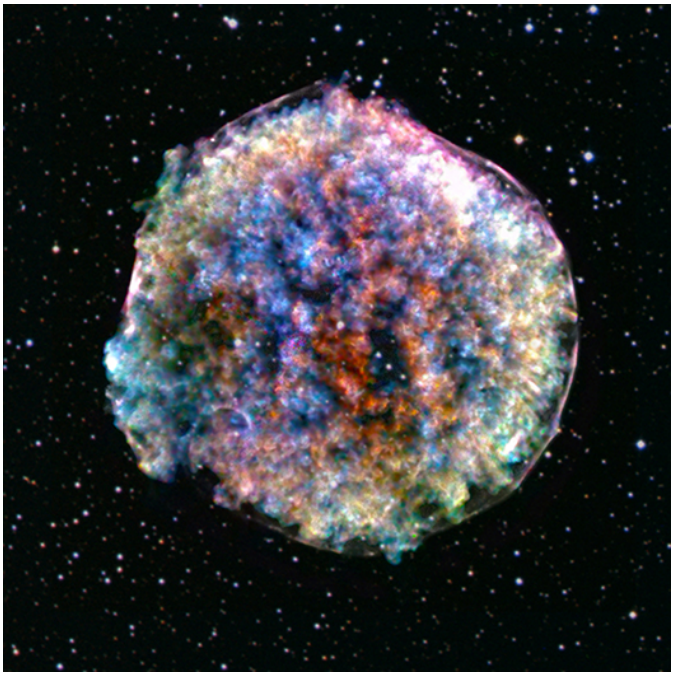

Figure 1: Composite image of the Tycho's SNR. The X-ray data was taken with NASA's Chandra X-ray observatory and the optical data of the stars is part of the Digitized Sky Survey (Chandra X-ray Center, 2019).

Subject of the present study is a different SNR showing a very peculiar morphology in X-rays (Dubner, G. et al., 2013), whose origins yet remain unclear: the well-studied Galactic SNR Puppis A. In this work, a hydrodynamical (HD) model of the SNR Puppis A is developed, with the goal to reproduce the plasma conditions and the observed X-ray morphology of the remnant as best as possible and gain insights about the structure of the inhomogeneous ISM that Puppis A is interacting with. Section 2 provides the astrophysical background about SNe, SNRs and the basics of astrophysical hydrodynamics. In Section 3 the existing observations of Puppis A in X-rays, radio and infrared are summarised, Section 4 serves as an introduction to the numerical code PLUTO, which is used to carry out the hydrodynamical simulations in this work, and in Section 5, the model setup and simulation results are presented. A discussion of the results and an outlook are given in Section 6.

2. Astrophysical background

This chapter serves as an overview of the basic astrophysical principles and processes that this work is based on. Since the overall goal of this study is to develop a hydrodynamical model of a supernova remnant expanding into a highly inhomogeneous interstellar medium (ISM), it is important to understand how supernova remnants are created in the first place, how they evolve over time, and how they interact with the surrounding ISM. Both of these topics will be covered in Sects. 2.1 and 2.2. Moreover, a basic understanding of fluid dynamics and shocks is required, which will be provided in Sect. 2.3.

2.1. The interstellar medium

The interstellar medium (ISM) is the general term for the gas and dust that exists in the space between the stars within galaxies. Typically, it consists to 99 % of gas and less than 1 % of dust. In a normal star-forming galaxy like the Milky Way, the ISM contributes approximately only $10 - 20$ % to the entire mass of the galaxy (Saintonge, 2025). The average ISM density in the Milky Way amounts to around $1\,\mathrm{atom\,cm^{-3}}$. The element abundances are fairly similar to the cosmic abundances with 90 % of hydrogen (H), 10 % of helium (He) and 0.1 % of heavier elements (Seward and Charles, 2010a). By mass, hydrogen makes up around 70 % of the total ISM mass. The temperature and density variations in the ISM are quite severe and range across at least six orders of magnitude, which in turn means that it is not in thermal equilibrium but instead governed by pressure equilibrium (Saintonge, 2025). More specifically, the ISM can be broken down into three different phases, as introduced by McKee and Ostriker (1977): the hot ionised medium, the warm medium (neutral and ionised), and the cold neutral medium, which also accounts for the formation of cold molecular clouds with high densities. To give an example, the physical conditions in these five regimes are summarised in Table 1 for a galaxy like the Milky Way.

Phase	$\boldsymbol{T}$ **[K]**	$\boldsymbol{n}$ **[cm^{-3}]**	**Mass fraction [%]**	**Observable in**
Hot ionised medium	10^6	0.004	3	X-rays, UV absorption lines
Warm medium (ionised)	8×10^3	0.2	12	Optical emission lines, radio emission (non-thermal)
Warm medium (neutral)	6×10^3	0.4	35	H I 21 cm line
Cold neutral medium	80	40	30	H I 21 cm, UV/optical absorption lines, FIR fine-structure lines
Molecular clouds	15	>100	20	Molecular lines (CO), FIR continuum (dust)

Table 1: Typical physical conditions in the ISM for a galaxy similar to the Milky Way. Adapted from Saintonge (2025).

Hot ionised medium The hot ionised medium (HIM) accounts for the largest fraction of the ISM not by mass but by volume because of the low density. In observations, it is traced best by diffuse X-ray emission or UV absorption lines with respect to background sources such as stars or active galactic nuclei (AGN) (Saintonge, 2025). The HIM is heated mainly by shocks created in supernova explosions and is often found to form bubble-like structures within the colder ISM (Saintonge, 2025).

Warm medium The warm medium consists of both a neutral and an ionised component, namely the warm neutral medium (WNM) and the warm ionised medium (WIM). The WNM, similar to the CNM, is traced in observations by 21 cm H I line emission. However, it can be distinguished from the CNM by its larger extent (Saintonge, 2025).

The WIM is composed mostly of ionised hydrogen (H II), which is created through photoionisation by UV emission of hot stars. The WIM is distinguished from H II regions and planetary nebulae, which are also ionised regions in the ISM with similar temperatures to the WIM, mainly by its lower density and distribution throughout a galaxy. Unlike H II regions and planetary nebulae, the WIM is not restricted to a galaxy's disk but also extends into the halo (Saintonge, 2025).

Cold neutral medium The cold neutral medium (CNM) is the phase of the ISM with the lowest temperature but due to its higher densities (see Table 1) accounts for around half of the total mass of the ISM. The atomic hydrogen in the CNM is in the ground state (H I), which is why the cold phase of the ISM is best observed at radio wavelengths via the 21 cm hydrogen line (Saintonge, 2025). The 21 cm line corresponds to a spin flip transition in the ground state of neutral atomic hydrogen, meaning the spin state of proton and electron changes from parallel to anti-parallel and a photon with an energy equivalent to that of the transition is emitted (Seward and Charles, 2010b). By compression of the CNM, molecular clouds can develop with even higher density and lower temperature. Similar to the rest of the ISM, the largest mass fraction in molecular clouds is hydrogen, but in its molecular form (H_2). However, due to the symmetry of the molecule, emission from H_2 is only possible via a quadrupole transition, which requires temperatures well above those found in molecular clouds. As a result, the direct observation of H_2 is not possible. Therefore, molecular clouds are most commonly traced by CO line emission, which is the second most common molecule in the ISM (Saintonge, 2025). Usually, there is also on average 1% of dust present in the colder ISM, which can be observed due to emission in the mid-infrared (MIR) and far-infrared (FIR). Specifically polycyclic aromatic hydrocarbons (PAH), which are tiny grains of carbon, are very well observable in the MIR (Saintonge, 2025).

2.2. Supernovae and supernova remnants

A supernova (SN) is generally known as the catastrophic explosion of a star at the end of its life cycle. They are highly energetic events, which typically release around 10^{51} erg of kinetic energy (Vink, 2020). The outer layers of the respective star are accelerated into space, reaching initial velocities between $10000 - 15000\,\mathrm{km\,s^{-1}}$ and the surrounding ISM as well as the ejecta are heated up to several million degrees, hot enough to emit thermal X-rays (Seward and Charles, 2010a).
In general, a distinction between two types of SNe is made, namely **core collapse (type II)** and **thermonuclear (type Ia)**. Observationally, they can be identified based on their optical light curves and spectra. Figure 2 shows the light curves of four different SNe of both type Ia and type II to illustrate the differences. For type Ia events, the rise of the intensity in the beginning is fairly steep, reaching its maximum within about two weeks. Thereafter, the intensity decreases exponentially with a characteristic time of $\sim 55\,\mathrm{days}$. The light curves of many type Ia events are found to be similar, which indicates that the underlying explosion mechanism and the progenitor stars are similar. Additionally, the maximum brightness is usually nearly the same, which is why they can be used as standard candles for astronomical distance measurements (Seward and Charles, 2010a).

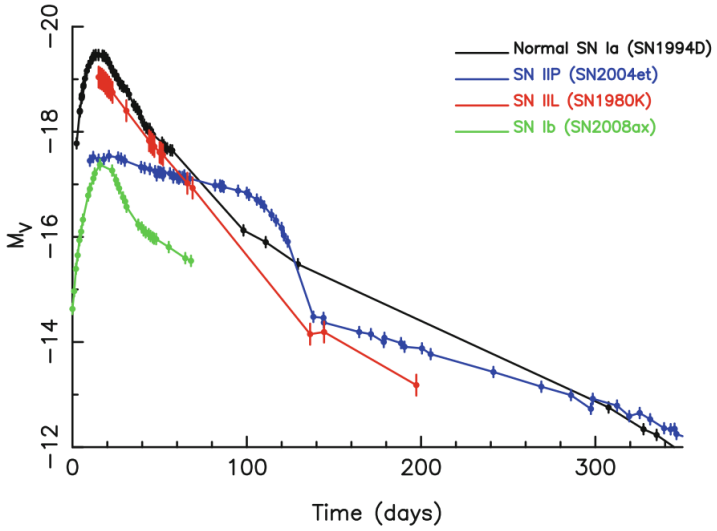

Figure 2: Optical light curves of four different SNe. The black line (SN 1994D) shows the light curve of a typical Ia event, while the blue and red lines belong to type IIP and type IIL, respectively. Additionally, a light curve from a type Ib event is shown in green (Vink, 2020).

In contrast, the optical light curves of type II SNe show more variability between different events and the luminosity is usually lower by around two orders of magnitude compared to type Ia. The initial rise to maximum brightness is less steep, the maximum itself

is broader, and the subsequent decline happens on more irregular timescales. All in all, for type II SNe the light curves are a lot more individual to the respective event, which points at a broader range of progenitor stars and slight variations in the explosion mechanism (Seward and Charles, 2010a). Most commonly, type II SNe are divided into the sub-types IIP and IIL based on the shapes of their light curves (see Fig. 2). In type IIP light curves a plateau is present following the maximum brightness, while in type IIL light curves the luminosity declines linearly after the maximum. Generally, a faster decline after the peak luminosity hints at a smaller amount of ejecta (Vink, 2020).
Regarding the optical spectra, the absence of hydrogen lines in type Ia spectra is the most prominent difference to type II, while in type II spectra hydrogen lines are dominating, suggesting young stars with hydrogen-rich envelopes as progenitors (Seward and Charles, 2010a). To understand where these differences in the light curves and spectra of the two SNe types stem from, the evolution of the progenitor star to the explosion needs to be considered.
On the main sequence, stars maintain hydrostatic equilibrium by fusion of hydrogen to helium within the core. Once hydrogen is depleted, the star is compressed by gravity and helium fusion is triggered, which results in the production of carbon and oxygen. For stars with initial masses of the order of one to a few solar masses, fusion does not continue at this stage. The star is stabilised by electron degeneracy pressure, halting the gravitational collapse. What remains is a so-called white dwarf (WD), a very dense star that has approximately the size of the Earth but the mass of the Sun and cannot evolve any further unless it reaches the Chandrasekhar mass limit of $1.44\,M_\odot$ (Seward and Charles, 2010a). If the star is part of a binary system, this is possible by mass accretion from its companion. Once the star surpasses the Chandrasekhar limit, electron degeneracy pressure can no longer withstand gravity and the collapse continues, which raises pressure and temperature in the core (Seward and Charles, 2010a). If temperature and density of the degenerate matter in the core become high enough ($\rho \approx 3 \times 10^9\,\mathrm{g\,cm^{-3}}$, $T \approx 2 \times 10^8\,\mathrm{K}$), carbon and oxygen fusion is enabled and the heat produced in these fusion reactions can no longer be compensated by neutrino cooling. As a result the nuclear fusion process runs away. Around 10^{52} ergs of energy are released in the subsequent explosion and the star is destroyed entirely (Vink, 2020). This type of explosion is known as a type Ia or thermonuclear SN. In the fusion reactions, a large amount of radioactive ^{56}Ni is created. The slower decline of the type Ia light curve can be explained by the delayed energy release through the decay of ^{56}Ni (Seward and Charles, 2010a).
In the case of high mass stars ($M_{\mathrm{star}} > 10\,M_\odot$), the nuclear fusion continues until an iron core is created, at which point fusion processes are no longer energetically beneficial. Around the core of iron, the star is now made up of onion-like layers, starting with a shell of silicon and sulphur, followed by neon and oxygen, carbon, helium, and finally hydrogen. The density in the core is comparable to that of a WD while the density in the hydrogen envelope is rather low (Seward and Charles, 2010a). Since the iron core cannot produce any more energy but its mass increases continuously by silicon fusion in the surrounding layer, it is compressed further until the iron decomposes into lighter nuclei and finally protons. These protons then capture electrons to generate neutrons and

neutrinos. Thereby the electron degeneracy pressure that has been stabilising the core up to this point is reduced. Eventually, this results in a runaway process, in which the core collapses within milliseconds until it reaches nuclear density (Seward and Charles, 2010a), forming a proto-neutron star (Vink, 2020). A shock wave is created by the energy released from the in-falling matter (Seward and Charles, 2010a). This process is usually referred to as core bounce (Vink, 2020). The shock then propagates through the outer layers of the star until it reaches the surface and matter is ejected. At this point, light can be observed from the explosion: a type II or core collapse SN (Seward and Charles, 2010a). The explosion mechanism for core collapse SNe is not very well understood yet. In most numerical simulations, the shock wave is not powerful enough to reach the surface of the star and stalls. One possible and frequently used explanation to how the explosion still takes place is the revival of the shock by neutrinos, which escape from the proto-neutron star, but even then not all models are successful (Vink, 2020). Depending on the mass of the progenitor, type II SNe usually leave behind a neutron star, or for very massive stars even a black hole (Vink, 2020).

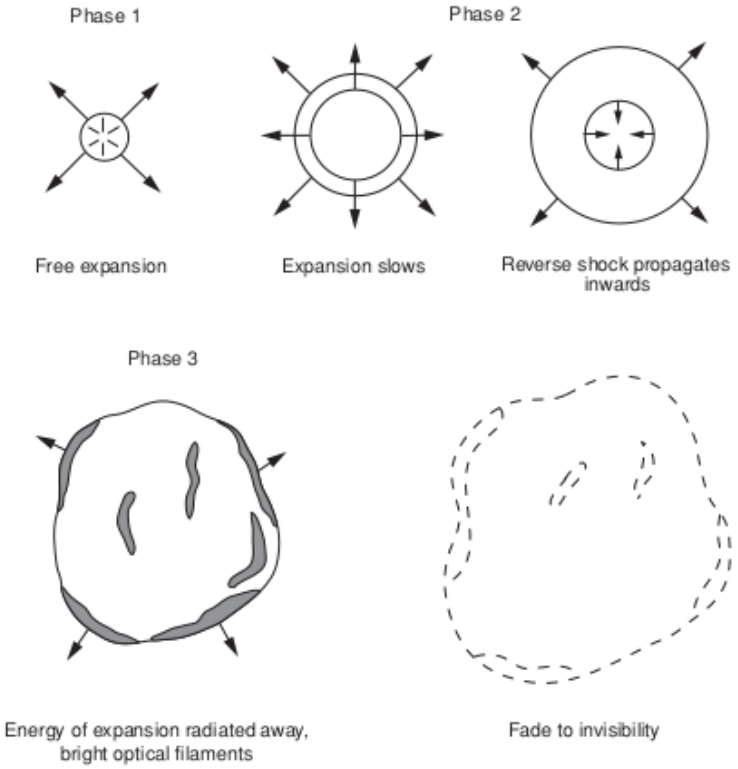

Figure 3: Schematic showing the four phases of SNR evolution (Seward and Charles, 2010a).

For completeness, it should be added that not only type II SNe result from the core collapse of a star, but also types Ib and Ic. Since no hydrogen lines are present in their

spectra, these events are classified as type I. However, the explosion mechanism is closer to type II. The main difference to type II is that, judging from the lack of hydrogen lines in the spectra, type Ib/c events were somehow stripped of the hydrogen envelope. This is possible either by a strong stellar wind or by interaction with a stellar companion (Vink, 2020). The light curve of a type Ib event is shown in Fig. 2. Again, as the light curve declines fairly quickly after maximum, this hints at a smaller amount of ejecta or in this case a high mass loss prior to the SN (Vink, 2020).
In any SN explosion (type I or II) typically around 10^{51} erg of kinetic energy is released into the ambient medium. The ejecta from the former star move supersonically outwards and interact with the ISM, forming a shock wave that heats the plasma. Starting with the first interaction of the ejecta with the ambient ISM, the former supernova transitions to what is commonly referred to as a supernova remnant (SNR). The evolution of SNRs can be divided into four different phases (see Fig. 3), namely the ejecta-dominated phase, the Sedov-Taylor phase, the snow-plough phase and the merging phase (Vink, 2020). The characteristics of these four phases will be discussed in further detail in the following.

2.2.1. Ejecta-dominated phase

The ejecta-dominated (ED) phase is the first evolutionary stage of a SNR. As already briefly mentioned, the ejecta are accelerated outwards in the explosion to velocities exceeding the sound velocity in the ambient medium. This means a shock wave forms, the so-called forward shock, which accelerates, compresses, and heats the ambient medium. In response, the shocked ambient medium pushes back on the ejecta in the same manner, forming a reverse shock that moves back into the ejecta. Forward and reverse shock are separated by a contact discontinuity (Truelove and McKee, 1999).

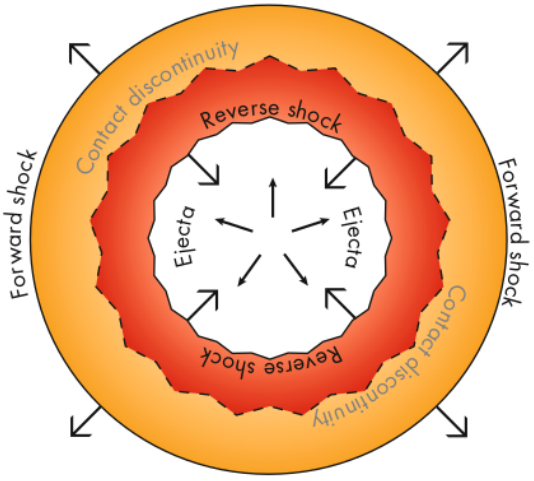

Figure 4: Schematic illustration showing the forward and the reverse shock propagating outward/inwards. The ejecta in the interior expands freely until hit by the reverse shock (Vink, 2020).

The unshocked ejecta in the interior of the remnant expand freely until hit and decelerated by the reverse shock (Truelove and McKee, 1999). This is shown schematically in Fig. 4. In the ED phase, the mass of the ejecta greatly exceeds the mass of the swept up ISM ($M_{\mathrm{ISM}} << M_{\mathrm{ej}}$) and the majority of the energy from the explosion is carried in the cold, freely expanding ejecta (Vink, 2020). Radiative losses in this phase are negligible (Truelove and McKee, 1999).

2.2.2. Sedov-Taylor phase

The second stage in the evolution of a SNR is the Sedov-Taylor (ST) phase. In contrast to the ED phase, the ISM mass swept up by the forward shock is now dominant over the mass of the ejecta ($M_{\mathrm{ISM}} >> M_{\mathrm{ej}}$). The energy is contained as both internal and kinetic energy in the expanding hot shell (Vink, 2020). The material between the forward and reverse shock is compressed and heated enough to emit X-rays. As the reverse shock travels further inwards, it reaches the centre and eventually disperses (Seward and Charles, 2010a). Radiative losses in this phase do not play a role for the dynamical evolution of the remnant and can again be neglected (Truelove and McKee, 1999). This means that the expansion of the remnant is adiabatic for some time. In this case, the Sedov-Taylor solution is applicable to describe the evolution, according to which the radius R of the blast wave is given by

$$R = 14 \left(\frac{E_0}{10^{51}\,\mathrm{erg}} \right)^{\frac{1}{5}} \left(\frac{n}{\mathrm{cm}^{-3}} \right)^{-\frac{1}{5}} \left(\frac{t}{10^4\,\mathrm{yr}} \right)^{\frac{2}{5}} \mathrm{pc} \tag{1}$$

with the explosion energy E_0, the particle number density n of the ambient medium and the age t of the SNR. Evidently, the expansion of the remnant depends only on the initial explosion energy E_0 and the ambient density n (Seward and Charles, 2010a).

In reality, the explosion is unlikely to run symmetrically. Irregularities in the ISM density and stellar winds can influence the remnants evolution and lead to asymmetries. Additionally, hydrodynamical instabilities, specifically **Rayleigh-Taylor instabilities**, occurring at the contact discontinuity cause the ejecta to break into clumps (Seward and Charles, 2010a). The so-called Rayleigh-Taylor instability is a type of hydrodynamical instability, which emerges whenever a medium with low density is accelerated into a medium with high density (Vink, 2020), meaning when the density gradient in the medium and the acceleration point in opposite directions (LeVeque et al., 1998b). At the interface between the two fluids, small perturbations are then amplified, leading to the formation of structures commonly referred to as Rayleigh-Taylor fingers (Vink, 2020). The top of these finger-like structures is often described to be reminiscent of mushroom caps (LeVeque et al., 1998b). Rayleigh-Taylor instabilities are the prominent type of hydrodynamical instabilities to consider in the context of SNRs. They were suspected to arise around the contact discontinuity due to the strong density gradients present there and were later found to occur in decelerating SNR shells in hydrodynamical simulations (Vink, 2020). At the contact discontinuity the higher density ejecta is decelerated by the

lower density shocked ISM (see Sect. 2.2.1), so the acceleration in this case is pointed inwards in the opposite direction of the density gradient. Due to the Rayleigh-Taylor instabilities, the ejecta then forms the typical finger-like structures, extending into the shocked ISM ahead of the contact discontinuity (Seward and Charles, 2010b). Figure 5 displays Rayleigh-Taylor instabilities in 2D simulations of Type Ia SNRs with two different density profiles of the surrounding medium. The Rayleigh-Taylor fingers are more pronounced when the ambient density follows a stellar wind profile, compared to a uniform ambient density. In case of the stellar wind profile, the instabilities become strong enough to even affect the reverse shock. Generally, Rayleigh-Taylor instabilities play a role in enabling the mixing of the shocked ejecta from the SN explosion with the shocked ambient medium, which was confirmed for example in observations of SN 1987A (Vink, 2020).
In addition to the Rayleigh-Taylor instability, the so-called Kelvin-Helmholtz instability is commonly encountered in SNRs. This specific hydrodynamical instability occurs when two layers of fluid move side by side, which is the case at the sides of the Rayleigh-Taylor fingers. The resulting shear is what triggers the Kelvin-Helmholtz instability and causes the fluids to mix (Vink, 2020).

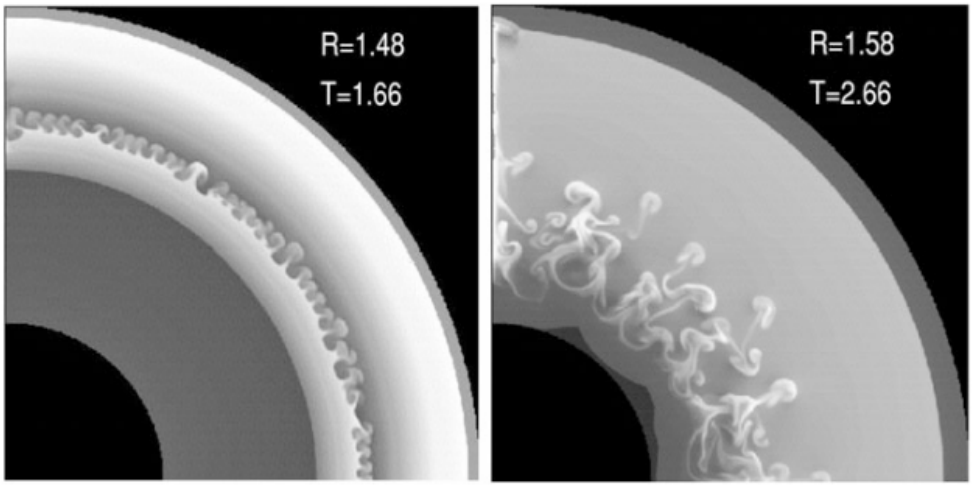

Figure 5: Rayleigh Taylor instabilities in 2D simulations of Type Ia SNRs (Vink, 2020). In the left image, the density profile of the ambient medium is uniform, on the right a stellar wind profile was used. The ejecta density profile is exponential in both cases.

2.2.3. Snow-plough phase and merging phase

The third phase in the evolution of a SNR is called radiative phase (Seward and Charles, 2010a) or snow-plough phase (Vink, 2020). An increasing amount of cold ambient medium is swept up by the remnant as it expands, which causes the temperature behind the shock to drop. Once it has decreased to around 2×10^5 K, recombination of electrons

with carbon and oxygen ions is possible, which enables UV-line emission. This means radiative losses are no longer negligible (Seward and Charles, 2010a). In fact, in this stage the majority of the remnants energy is released through radiation, which means energy conservation can no longer be assumed. The propagation of the forward shock is instead dictated by radial momentum conservation (Vink, 2020). The radiative phase usually lasts for around 10^5 yr (Seward and Charles, 2010a).
Eventually, the forward shock slows down enough to reach a velocity in the range of the sound speed in the ISM. This means the remnant has entered its fourth and final evolutionary stage, the so-called merging phase. The forward shock gradually dissipates and the expansion of the shell now continues at subsonic speeds. The SNR begins to fade and blends back into the surrounding ISM (Vink, 2020).

2.3. Basic principles of astrophysical hydrodynamics

In numerical astrophysics, the interstellar medium is generally described as a compressible fluid. In this context, an overview over the fundamental equations such as the Euler- and Navier Stokes equations will be provided in the following. Additionally, a mathematical description of shocks will be discussed, as this is especially relevant for SNRs.

2.3.1. The Euler equations of classical hydrodynamics

The Euler equations of classical fluid dynamics are a set of partial differential equations that describe inviscid flows in ideal compressible fluids. They can be derived from the conservation laws of mass, momentum and energy (Pringle and King, 2007). In general, a conservation law is a time-dependent system of partial differential equations that according to LeVeque et al. (1998a) can be written as

$$\frac{\partial}{\partial t} q(x,t) + \frac{\partial}{\partial x} f(q(x,t)) = 0, \tag{2}$$

with a m-dimensional vector of conserved quantities $q(x,t)$ and the so called flux function $f(q(x,t))$, a vector-valued function depending on $q(x,t)$. In other terms, each component $q_\mathrm{j}(x,t)$ of $q(x,t)$ corresponds to the density function of the jth conserved physical quantity, the total of which can be obtained at a time t by integrating $q_\mathrm{j}(x,t)$ over the considered spatial interval: $\int_{x_1}^{x_2} q_\mathrm{j}(x,t)\,\mathrm{d}x$. Since the quantities in $q(x,t)$ are conserved, this implies that $\int_{-\infty}^{\infty} q_\mathrm{j}(x,t)\,\mathrm{d}x$ is constant over time.
The jth component of the flux function $f(q(x,t))$ contains the flow rate (= flux) of the jth conserved quantity $f_\mathrm{j}(q(x,t))$ at a point (x,t) (LeVeque et al., 1998a). It should be noted that Eq. 2 describes a one dimensional problem but can be extended to more than one spatial dimension (LeVeque et al., 1998a). In three dimensions, Eq. 2 becomes

$$\frac{\partial}{\partial t} q(\boldsymbol{x},t) + \frac{\partial}{\partial x} f(q(\boldsymbol{x},t)) + \frac{\partial}{\partial y} g(q(\boldsymbol{x},t)) + \frac{\partial}{\partial z} h(q(\boldsymbol{x},t)) = 0, \tag{3}$$

where f, g, and h describe the fluxes in the x, y, and z directions (LeVeque et al., 1998a). In an arbitrary volume V the flux through its surface S at a point $\boldsymbol{x} = (x,y,z)$ is then

calculated via $\mathcal{F}(q(\boldsymbol{x},t)) \cdot \mathbf{n}$, with $\mathcal{F}(q(\boldsymbol{x},t)) = (f,g,h)$ and the normal vector to the surface $\mathbf{n}$. In line with LeVeque et al. (1998a), Eq. 3 subsequently can be rewritten as

$$\frac{\partial}{\partial t} q(\boldsymbol{x},t) + \nabla \cdot \mathcal{F}(q(\boldsymbol{x},t)) = 0. \tag{4}$$

Based on the general approach described above, the derivation of the Euler equations in their differential form from mass, momentum and energy conservation in three dimensions will be summarised in the following. It has to be noted that in the differential form of the equations, it is assumed that $q(\boldsymbol{x},t)$ and the corresponding flux functions are smooth (LeVeque et al., 1998a). How discontinuities in the physical quantities are dealt with will be discussed in Sec. 2.3.2.

Conservation of mass The conservation of mass dictates that any change of mass in an arbitrary volume V has to be equal to the in- or outflow of mass through the surface S of the volume. According to Pringle and King (2007), this can be expressed as

$$\frac{\mathrm{d}}{\mathrm{d}t} \int_V \rho \, \mathrm{d}V = -\int_S \rho \mathbf{u} \cdot \mathbf{dS}, \tag{5}$$

with the mass density ρ, the velocity $\mathbf{u}$, and the vector element on the surface $\mathbf{dS} = \mathbf{n}\mathrm{dS}$, where $\mathbf{n}$ is the normal vector to the surface. The mass flux is given by $f(\boldsymbol{x},t) = \rho(\boldsymbol{x},t)\mathbf{u}(\boldsymbol{x},t)$. Applying Gauss's theorem, Eq. 5 can be rewritten as

$$\frac{\mathrm{d}}{\mathrm{d}t} \int_V \rho \, \mathrm{d}V = -\int_V \nabla \cdot (\rho \mathbf{u}) \, \mathrm{d}V. \tag{6}$$

Equation 6 has to be valid for any volume V. This implies that the following relation holds, which is commonly referred to as the **continuity equation** (Pringle and King, 2007):

$$\frac{\partial}{\partial t} \rho + \nabla \cdot (\rho \mathbf{u}) = 0. \tag{7}$$

Conservation of momentum The total momentum in a given volume V can be calculated by integrating the momentum density, which corresponds to the mass flux $\mathbf{f} = \rho\mathbf{u}$ over the volume V. Similar to the derivation of the continuity equation, following Pringle and King (2007), the rate of change of the total momentum within V is expressed as

$$\frac{\mathrm{d}}{\mathrm{d}t} \int_V \rho \mathbf{u} \, \mathrm{d}V. \tag{8}$$

In addition to the momentum flux across the surface S of the volume V, the surface stress must be considered, which can be written in terms of the stress tensor $\mathbf{T} = T_{ij}$ (Pringle and King, 2007). The stress tensor is defined by taking into account force $F_{ij} = T_{ij}\mathrm{d}S_j$ exerted in this case by the pressure p of the medium surrounding V onto the surface S. This means the stress tensor takes the form $T = -p\delta_{ij}$ (Pringle and King, 2007) or in matrix form $\mathbf{T} = -p\mathbf{I}$, where $\mathbf{I}$ denotes the unit tensor, which leads to the following equation (Dullemond and Springel, 2011):

$$\frac{\mathrm{d}}{\mathrm{d}t} \int_V \rho \mathbf{u} \, \mathrm{d}V = -\int_S \rho \mathbf{u} (\mathbf{u} \cdot \mathbf{n}) \mathrm{d}S - \int_S p \, \mathbf{n} \mathrm{d}S \tag{9}$$

Using Gauss's theorem, this can again be rewritten as

$$\frac{\mathrm{d}}{\mathrm{d}t}\int \rho\mathbf{u}\,\mathrm{d}V = -\int_V \nabla\cdot(\rho\mathbf{u}\otimes\mathbf{u}+p\mathbf{I})\,\mathrm{d}V. \tag{10}$$

This means for any volume V, the relation

$$\frac{\partial}{\partial t}(\rho\mathbf{u}) + \nabla\cdot(\rho\mathbf{u}\otimes\mathbf{u}+p\mathbf{I}) = 0, \tag{11}$$

holds, which is the differential form of the momentum conservation law in a compressible fluid (Dullemond and Springel, 2011).

Conservation of energy The total energy in a volume V can be expressed as the volume integral over the energy density $E_\mathrm{t} = \rho(e+\frac{1}{2}u^2)$, which is composed of the kinetic energy and the internal energy e. According to energy conservation, the rate of change of the total energy

$$\frac{\mathrm{d}}{\mathrm{d}t}\int_V \rho\left(e+\frac{1}{2}u^2\right)\mathrm{d}V \tag{12}$$

is equal to the net energy flux across the surface S of the volume (Dullemond and Springel, 2011). Additionally, the work exerted on the volume by the pressure of the surrounding gas needs to be taken into account (Dullemond and Springel, 2011), which results in

$$\frac{\mathrm{d}}{\mathrm{d}t}\int_V \rho\left(e+\frac{1}{2}u^2\right)\mathrm{d}V = -\int_S \rho\left(e+\frac{1}{2}u^2\right)\mathbf{u}\cdot\mathbf{dS} - \int_S p\mathbf{u}\cdot\mathbf{dS}. \tag{13}$$

If Gauss's theorem is applied, Eq. 13 can be rewritten as

$$\frac{\mathrm{d}}{\mathrm{d}t}\int_V \rho\left(e+\frac{1}{2}u^2\right)\mathrm{d}V + \int_V \nabla\cdot\left[\left(\rho e+\frac{1}{2}\rho u^2+p\right)\mathbf{u}\right]\mathrm{d}V = 0. \tag{14}$$

Again, Eq. 14 has to be true for any volume V, which yields the differential form of the energy conservation equation for compressible fluids (Dullemond and Springel, 2011):

$$\frac{\partial}{\partial t}\rho\left(e+\frac{1}{2}u^2\right) + \nabla\cdot\left[\left(\rho e+\frac{1}{2}\rho u^2+p\right)\mathbf{u}\right] = 0. \tag{15}$$

If the definition of the total energy density E_t is inserted, Eq. 16 can be written in a condensed form as

$$\frac{\partial}{\partial t}E_\mathrm{t} + \nabla\cdot\left[\left(E_\mathrm{t}+p\right)\mathbf{u}\right] = 0. \tag{16}$$

In three dimensions, Eqs. 7, 11, and 16 constitute a system of five partial differential equations: the Euler equations of classical fluid dynamics. If the vector $q(x,t)$ and the flux functions $\mathcal{F}(q(\boldsymbol{x},t)$ are defined as

$$q(\boldsymbol{x},t) = \begin{pmatrix} \rho(\boldsymbol{x},t) \\ \rho(\boldsymbol{x},t)\mathbf{u}(\boldsymbol{x},t) \\ E(\boldsymbol{x},t) \end{pmatrix}, \quad \mathcal{F}(q(\boldsymbol{x},t)) = \begin{pmatrix} \rho\mathbf{u} \\ \rho\mathbf{u}\otimes\mathbf{u} + p\mathbf{I} \\ \mathbf{u}(E+p) \end{pmatrix}^T \tag{17}$$

then the Euler equations can be written following the general structure of Eq. 3 (LeVeque et al., 1998a):

$$\frac{\partial}{\partial t}\begin{pmatrix} \rho \\ \rho\mathbf{u} \\ E \end{pmatrix} + \nabla\cdot\begin{pmatrix} \rho\mathbf{u} \\ \rho\mathbf{u}\otimes\mathbf{u} + p\mathbf{I} \\ (E+p)\mathbf{u} \end{pmatrix}^T = 0. \tag{18}$$

Since there are five equations, but six variables (ρ, u_1, u_2, u_3, e, and p), the pressure needs to be expressed as a function of the density ρ and the internal energy e to provide closure to the system. This is done via an equation of state, which most commonly is the ideal gas equation

$$p = \frac{R}{\mu}\rho T, \tag{19}$$

where R is the gas constant, μ is the mean molecular weight of the gas, and T is the temperature (Pringle and King, 2007). By making use of a few additional relations, equation 19 can be rewritten in terms of the internal energy e and the adiabatic index $\Gamma = \frac{c_\mathrm{p}}{c_\mathrm{v}}$. Here, c_v is the specific heat at constant volume and c_p the specific heat at constant pressure. Additionally, for an ideal gas

$$\frac{R}{\mu} = c_\mathrm{p} - c_\mathrm{v} \tag{20}$$

as well as

$$e = c_\mathrm{v} T \tag{21}$$

are true (Pringle and King, 2007). Combining all of the above equations with Eq. 19 results in

$$p = \rho e(\Gamma - 1), \tag{22}$$

which is the required expression for p as a function of ρ and e (Pringle and King, 2007). It should be noted that in the derivation of the Euler equations presented here, effects like viscosity, thermal conduction, radiative transfer, and external forces like gravity are neglected, which is often a valid approximation in astrophysical hydrodynamics (Wolschin, 2021). Considering these effects would mean adding additional terms to the respective conservation laws:

Source terms The basic assumption, that is made in the derivation of the Euler equations is that the integral of the respective conserved quantity over the total volume changes only due to the flux through the surface of the volume. However, this is often not accurate. In parts, the conserved quantity may also be created or destroyed within the volume, which is also referred to as source or sink of the quantity. This

introduces so called source terms $S(q(\boldsymbol{x}, t))$ into Eq. 3, which contain the increase or decrease of the respective conserved quantity (LeVeque et al., 1998a):

$$\frac{\partial}{\partial t} q(\boldsymbol{x}, t) + \nabla \cdot \mathcal{F}(q(\boldsymbol{x}, t)) = S(q(\boldsymbol{x}, t)). \tag{23}$$

Examples of effects, that can be the cause of source terms are chemical reactions within the flow or ionisation (lead to a separate mass continuity equation for each species), external forces like gravity (source term in momentum and energy equations), radiative heat transfer (source term in the energy equation), and geometric source terms as a result of the reduction of a problem to lower dimensions by means of spherical or cylindrical symmetry (LeVeque et al., 1998a).

Dissipative fluxes Dissipative effects, like fluid viscosity or heat conduction, are also not yet taken into account in the Euler equations. These effects usually depend on the gradient of $q(\boldsymbol{x}, t)$ and introduce additional flux components in the conservation law, so called dissipative fluxes (LeVeque et al., 1998a). If both fluid viscosity and thermal conduction are added to the conservation laws, the result are the **Navier-Stokes equations** of classical fluid dynamics (LeVeque et al., 1998a).

2.3.2. Shocks

A shock occurs, when a compressible medium moves faster than the local signal speed, which in the adiabatic case is equal to the speed of sound c_s within the medium and, as discussed by Vink (2020), can be expressed as

$$c_\mathrm{s} = \sqrt{\left(\frac{\partial p}{\partial \rho}\right)} = \sqrt{\Gamma \frac{p}{\rho}}. \tag{24}$$

As previously, p denotes the pressure, ρ the mass density, and Γ the adiabatic index of the gas. As far as supernova remnants are concerned, most commonly a monoatomic, non-relativistic gas can be assumed, which means $\Gamma = \frac{5}{3}$ (Vink, 2020). In more technical terms, a shock can be described as a transition layer in a medium, where the physical properties, such as pressure, density, and velocity change abruptly (Vink, 2020). For supernova remnants, the length scale of the transition layer is so small, that it can't be resolved. In contrast, the mean free path of particle collisions is very large and on the scale of the size of the SNR itself. Therefore, shocks in supernova remnants are referred to as collisionless shocks (Vink, 2020). The consequences thereof will be discussed later on in this chapter.

Mathematically, shocks can be treated as a discontinuity in the physical parameters of the gas, which is known as the shock front (Sasaki, 2022). However, as already mentioned in Sect. 2.3.1, in the differential form of the Euler equations, the density and flux functions of the conserved quantities are assumed to be smooth, which is not the case at the shock front. Therefore, it is necessary to know how the physical quantities behave across the discontinuity.

The abrupt change of physical quantities over the transition layer, commonly referred to as jump, are in general dictated by mass, momentum and energy conservation. The so-called **Rankine-Hugoniot jump conditions** describe the physical conditions in the pre-shock (upstream) and post-shock (downstream) region and are derived from the above mentioned conservation laws. Usually, shocks can be approximated as plane parallel and fixed in time in a reference frame moving with the shock itself. In that case, the Rankine-Hugoniont jump conditions take the following form (Vink, 2020):

$$\rho_1 v_1 = \rho_2 v_2 \tag{25}$$

$$p_1 + \rho_1 v_1^2 = p_2 + \rho_2 v_2 \tag{26}$$

$$p_1 + e_1 + \frac{1}{2}\rho_1 v_1^2 = p_2 + e_2 + \frac{1}{2}\rho_2 v_2^2 \tag{27}$$

As before, ρ stands for the density, p for the pressure and e for the internal energy of the gas. The quantities indexed with 1 describe the upstream region, and the ones with index 2 the downstream region. The solution to this set of equations can be expressed in terms of the so-called sonic Mach number M_s, a dimensionless quantity that is defined as the ratio of the gas velocity in the upstream region v_1 and the local sound speed c_s (Vink, 2020):

$$M_\mathrm{s} \equiv \frac{\rho_1 v_1}{\Gamma p_1} = \frac{v_1}{c_\mathrm{s}}. \tag{28}$$

For a supersonic flow, $M_\mathrm{s} > 1$ and a flow with $M_\mathrm{s} \approx 5$ or larger is usually denoted as a strong shock, in which case the approximation $M_\mathrm{s} \to \infty$ is applicable. Typical Mach numbers in SNRs are very large and reach above $M_\mathrm{s} \approx 100$. For an ideal gas, the solution takes the form

$$\chi = \frac{(\Gamma + 1)M_\mathrm{s}^2}{(\Gamma - 1)M^2 + 2}, \tag{29}$$

where the compression ratio is defined as $\chi \equiv \frac{\rho_2}{\rho_1} = \frac{v_1}{v_2}$ and and Γ is the adiabatic index (Vink, 2020).

From a mathematical point of view, a shock can be treated as a so-called **Riemann Problem**. Very generally, the Riemann problem describes the conservation law $\frac{\partial}{\partial t}q + \frac{\partial}{\partial x}f(q)$ (see Eq. 2) in conjunction with two constant initial states q_l and q_r divided by a discontinuity (LeVeque et al., 1998a):

$$q(x, 0) = \begin{cases} q_\mathrm{l} \text{ if } x < 0 \\ q_\mathrm{r} \text{ if } x > 0. \end{cases} \tag{30}$$

The solution is dependent on how the left and right states q_r and q_l are related, which in this case is dictated by the Rankine-Hugoniot jump conditions (LeVeque et al., 1998a). In numerical codes, like the one used later on in this work (see Sect. 4.1), the solution to the Riemann problem is calculated in each numerical cell by means of a so-called Riemann solver (PLUTO Team, 2024).

As already briefly mentioned above, the shocks encountered in SNRs are collisionless, meaning the mean free path between particle-particle collisions resulting from Coulomb interactions is on the scale of the the remnant itself. As an example, the mean free path of proton collisions at an assumed shock velocity of $1000\,\mathrm{km\,s^{-1}}$ is around $32\,\mathrm{pc}$ (Vink, 2020). This implies that across the shock front thermalisation of the kinetic energy must be conveyed by other processes, which are in general referred to as collective effects. The incoming particles interact with plasma waves and electric fields in the shock transition layer and are thereby thermalised. However, the physical processes occurring across the shock transition layer are complex and not very well understood yet (Vink, 2020).
Since the plasma conditions up- and downstream are given by the Rankine-Hugoniont jump conditions anyway, at first it does not seem like the type of shock (collisional or collisionless) makes a difference. However, this is not completely true. The Rankine-Hugoniot jump conditions do not differentiate between particle species and only describe the overall plasma conditions. Because of the large mean free path of the Coulomb collisions, it cannot be assumed that all particle species thermalise equally across the shock transition layer. If the post-shock temperature is calculated from the Rankine-Huginot conditions separately for electrons (T_e) and protons (T_p), the result are two very different temperatures with a ratio of $\frac{T_\mathrm{e}}{T_\mathrm{p}} = \frac{m_\mathrm{e}}{m_\mathrm{p}} = 5.5 \times 10^{-4}$ (Vink, 2020). Despite the fact that it is not yet completely clarified, whether the heating processes across the shock front in general produce approximately the same ion- and electron temperatures, there is evidence from observations of young SNRs implying a lower electron temperature compared to the proton temperature. In SNRs it is possible to measure temperatures downstream in the vicinity of the shock from optical and UV spectroscopy. Further downstream, the electron temperature is usually derived from continuum and line-ratio measurements in X-rays. Ion temperatures can be estimated from X-ray Doppler line broadening (Vink, 2020).
Over time, the post-shock temperatures usually equilibrate between the different species via Coulomb collisions. However, the equilibration processes of electrons and protons take a few thousand years, in many cases even longer than the age of the SNR itself. The equilibration time is approximately proportional to the inverse of the electron density n_e (Vink, 2020). An important parameter in this context is the **ionisation age** τ of the remnant, which can be expressed as $\tau = n_\mathrm{e} t$, with the time t since the plasma has been shocked. The ionisation age is also a measure of the ionisation state of the plasma. Due to the low collision rates, the plasma in SNRs is usually not in ionisation equilibrium but in a state referred to as non-ionisation equilibrium (NEI). The ionisation rates are proportional to the electron density n_e (Vink, 2020). The ionisation time scale can be determined via X-ray spectroscopy and provides an estimate for whether temperature equilibrium of the different species is expected, for the ionisation state of the plasma, and subsequently provides a possibility to also determine electron densities and the age of the remnant. Figure 6 shows the temperatures of different species as a function of the ionisation age. Evidently, the electron temperature equilibrium of all species is reached at an ionisation age of $n_\mathrm{e} t \approx 10^{12} \mathrm{cm}^{-3}\,\mathrm{s}$. Similarly, for young SNRs collisional ionisation equilibrium is expected to be reached around the same ionisation age (Vink, 2020).

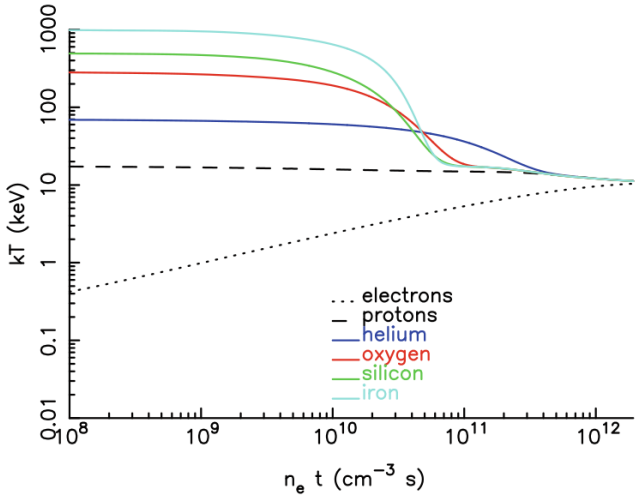

Figure 6: Temperature equilibration of different ions and electrons through Coulomb collisions as a function of the ionisation time. The dotted line shows the electron temperature, the dashed line the proton temperature and the solid lines the temperature of different ions. The initial post-shock temperature for each species was calculated from the Rankine-Hugoniot jump conditions with an assumed shock velocity of $3000\,\mathrm{km\,s^{-1}}$. Evidently, the initial post-shock temperature of the ions depends on the mass and is higher for heavier ions (Vink, 2020).

However, the Rankine-Hugonoit conditions do not hold for all types of shocks. If the shock becomes radiative, energy loss via radiation needs to be taken into account, which for SNR plasmas it governed by line radiation and thermal continuum processes. If the shock velocity is high, meaning above $\sim 200\,\mathrm{km\,s^{-1}}$, and subsequently the temperature T of the shocked plasma passes $10^6\,\mathrm{K}$, cooling processes are not very efficient. Figure 7 shows an example of a cooling function $\Lambda(T)$, which together with the electron density n_e and the proton density n_p can be used to calculated the emissivity ϵ of the gas (Vink, 2020):

$$\epsilon = n_\mathrm{e} n_\mathrm{p} \Lambda. \tag{31}$$

The cooling function also depends on the chemical abundances of the gas (Sasaki, 2022).

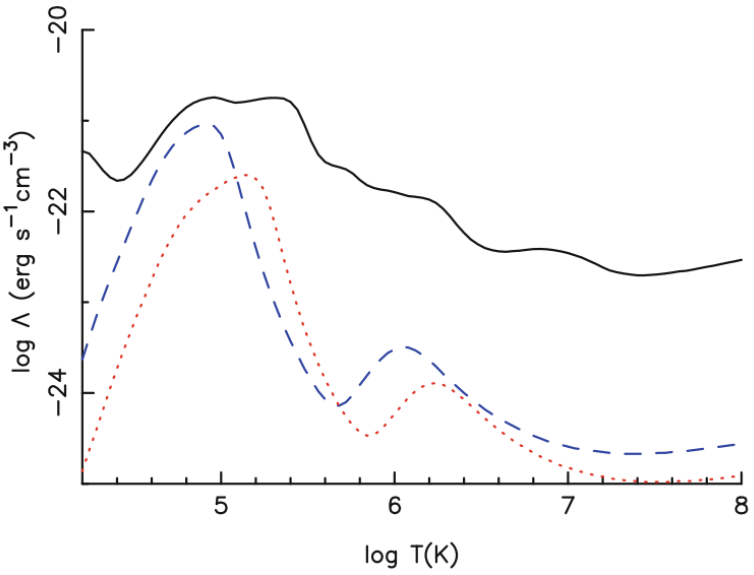

Figure 7: Cooling function of an optically thin plasma. The dashed blue line showcases the carbon contribution, and the dotted red line the oxygen contribution to the cooling (Vink, 2020).

3. The supernova remnant Puppis A

Puppis A is a Galactic core-collapse supernova remnant (SNR) in the southern hemisphere of the sky, coincident with the well-known Vela SNR, but located at a much larger distance, with estimates in the literature ranging from $1.3 \pm 0.3\,\mathrm{kpc}$ (Reynoso et al., 2016) to $2.2 \pm 0.3\,\mathrm{kpc}$ (Reynoso et al., 2003). Both studies mentioned here are mainly based on H I radio observations. The angular diameter of the remnant's shell is around $56'$ (Mayer et al., 2022), which implies a diameter of approximately 21.2 pc at an assumed distance of 1.3 kpc. Puppis A is known to host the central compact object (COO) RX J0822-4300, a high-velocity neutron star visible only in X-rays with an estimated proper motion of $\mu = 80.4\,\mathrm{mas\,yr^{-1}}$ (Mayer et al., 2020). At an assumed distance of 1.3 kpc, the projected velocity corresponds to $v_{\mathrm{proj}} = 496\,\mathrm{km\,s^{-1}}$ (Mayer et al., 2020). From the proper motion of the COO, it is possible to also derive an estimate for the kinematic age of Puppis A, as was done, for example, by Mayer et al. (2020). In their work, an age of $4000^{+700}_{-600}\,\mathrm{yr}$ is proposed. A similar age estimate of $3700 \pm 300\,\mathrm{yr}$ is found by Winkler et al. (1988) from the proper motion of oxygen-rich clumps, which were assumed to consist largely of pure ejecta from the SN. Puppis A is observable across a number of different wavelengths, ranging from radio to gamma rays. In the following, the focus will lie on the existing X-ray, radio, infrared observations of the remnant to gather as much constraints for the parameters of the model setup presented later on in this work as possible.

3.1. X-ray observations

Puppis A is one of the brightest sources in the X-ray sky with an unabsorbed X-ray flux of $F = 2.64 \times 10^{-8}\,\mathrm{erg\,s^{-1}\,cm^{-2}}$ in the 0.2-5 keV band (Mayer et al., 2022). At an assumed distance of 1.3 kpc, this equates to a X-ray luminosity of $L = 5.3 \times 10^{36}\,\mathrm{ergs\,s^{-1}}$ (Mayer et al., 2022).

The first full X-ray image of Puppis A was compiled by Dubner, G. et al. (2013) by combining two new pointed XMM-Newton observations with 23 archival data sets taken with both XMM-Newton and the Chandra X-ray Observatory. The resulting image is shown in Fig. 8 and covers also the southern and southwestern part of Puppis A, which previously had not been examined in X-ray observations. It is stated that Puppis A has a very unique appearance in X-rays with the visible filaments resembling a 'honeycomb', which is an implication of the remnant expanding in a complexly structured ISM. The filamentary pattern is found to be similar to younger Galactic SNRs such as Casssopeia A, the Crab Nebula, or Kepler's SNR, which leads them to believe that the emission shows the 'imprint' of the SN explosion on the surrounding ISM. Moreover, the X-ray emission seems to be solely thermal and not governed by a Pulsar Wind Nebula (PWN) in the centre, in which case non-thermal synchrotron emission would be expected. In general, the X-ray emission decreases from east to west and is rather weak in the newly covered southern part of the remnant.

The most prominent and brightest feature of Puppis A in X-rays is the bright eastern knot (BEK), clearly visible in Fig. 8 at the southeastern edge of the remnant. The BEK is suspected to be the most pronounced interaction site of the shock front with

an interstellar cloud of higher density (Hwang et al., 2005). Striking is also the band of harder X-ray emission that extends from the northeastern part across the SNR, shown in blue in Fig. 8 (Dubner, G. et al., 2013). This characteristic was previously identified in other publications as well, such as Katsuda et al. (2010) or Hwang et al. (2005). Dubner, G. et al. (2013) attributes this feature to a higher column density, which was derived from H I radio observations, coinciding with the band of hard emission and absorbing the softer part of the X-ray spectrum.

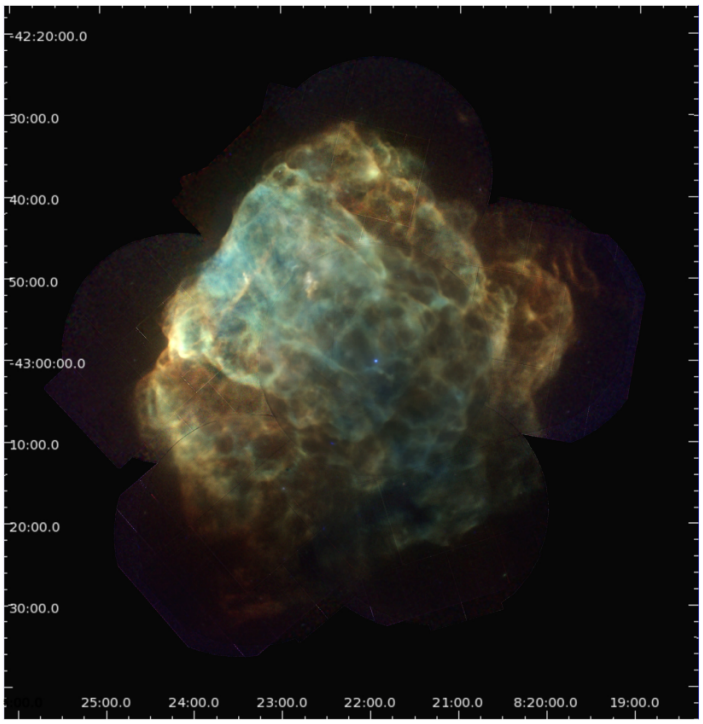

Figure 8: Full three-colour image of Puppis A in X-rays compiled by Dubner, G. et al. (2013) from a total of 25 XMM-Newton and Chandra observations. Red corresponds to the 0.3-0.7 keV band, green represents the 0.7-1.0 keV band and blue the 1.0-8.0 keV band. The data are shown in square root intensity scale and smoothed with a Gaussian. The blue point near the centre of the SNR is the COO RX J0822-4300.

The first study of the shocked plasma in X-rays over the entire remnant with high-spacial-resolution data from one single instrument was presented by Mayer et al. (2022), using data from the eROSITA X-ray telescope. They confirmed the results by Dubner, G. et al. (2013) that strong foreground absorption is present in Puppis A, especially in the southwestern part of the remnant. The absorbing column density over the whole remnant is found to vary by at least a factor of five (Mayer et al., 2022). Additionally, a temperature variation from east to west across the remnant by around a factor of two is determined, which, combined with the stronger absorption in the south-west, is stated to

be the reason for the belt of hard emission observed in Puppis A. Maps of the density and temperature distributions across the SNR compiled by Mayer et al. (2022) are shown in Fig. 9. Moreover, studies of the plasma ionization age and the emission measure

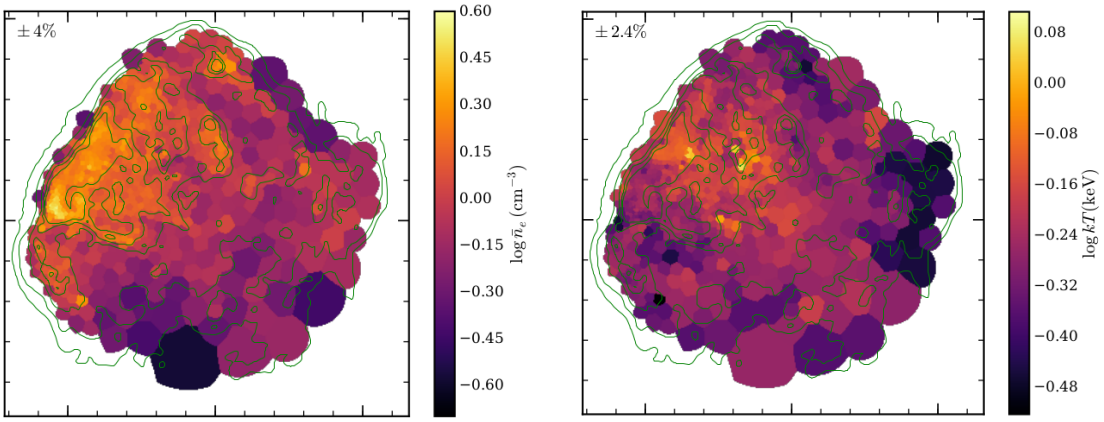

Figure 9: Density (left) and temperature (right) maps of Puppis A as presented by Mayer et al. (2022).

distribution are carried out, and it is concluded that the prominent features in Puppis A, such as the ejecta knot and the BEK have recently interacted with either the forward or the reverse shock. Regarding the element abundances, it is revealed that solar or subsolar abundances can be assumed for Puppis A. Elements, which are most commonly found in core-collapse supernovae, are concentrated in a few specific locations, such as the ejecta knot first discovered by Katsuda et al. (2008) in XMM-Newton observations. Mayer et al. (2022) were also able to provide an estimate for the total mass of ISM swept up by the forward shock, which contributes to the thermal X-ray emission:

$$M_{\mathrm{ISM}} = (78 - 87) \left(\frac{d}{1.3\,\mathrm{kpc}} \right)^{\frac{5}{2}} M_{\odot}. \tag{32}$$

In their calculation, a spherically symmetric shell at a distance d of 1.3 kpc is assumed, which implies a shockwave radius of $r = 10.6\,\mathrm{pc}$, as well as a radial density profile typical for the Sedov-Taylor phase of SNRs. Additionally, it is stated that the X-ray emitting plasma consists predominantly of swept-up ISM, with only a negligible contribution from the ejecta and an estimated average pre-explosion ISM density of $1.1 \times 10^{-24}\,\frac{\mathrm{g}}{\mathrm{cm}^{-3}}$ is given. From the Sedov-Taylor blast wave solution (Sedov, 1959), they also estimated the explosion energy E at an assumed age of Puppis A of $t = 4000\,\mathrm{yr}$:

$$E = (1.22 - 1.36) \left(\frac{r}{10.6\,\mathrm{pc}} \right)^{\frac{9}{2}} \left(\frac{t}{4000\,\mathrm{yr}} \right)^{-2} \times 10^{51}\,\mathrm{erg}. \tag{33}$$

At a distance of 1.3 kpc, this would imply an explosion energy on the order of magnitude of the canonical value of $E = 10^{51}\,\mathrm{erg}$.

Mayer et al. (2022) also extracted the X-ray spectrum of the entire remnant between 0.2 and 5 keV and identified prominent emission lines. The spectrum is shown in Fig. 10.

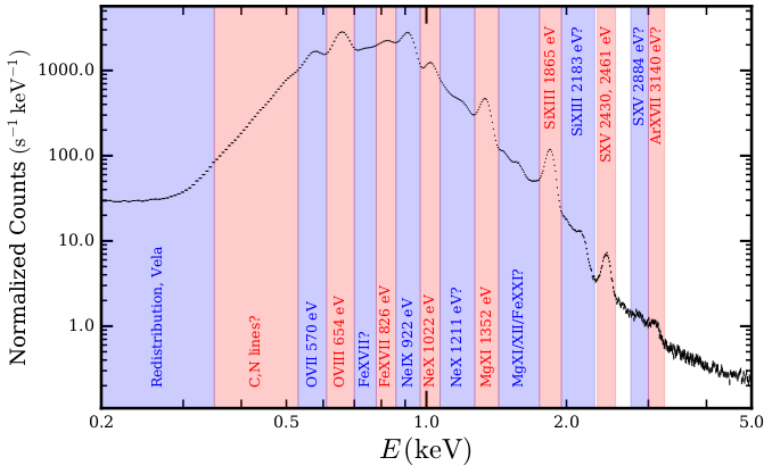

Figure 10: X-ray spectrum of the entire Puppis A SNR taken with the eROSITA X-ray telescope between 0.2 and 5 keV. The emission lines with a question mark do not dominate over the continuum. Figure taken from Mayer et al. (2022).

3.2. Radio observations

At radio wavelengths, Puppis A is observable as a shell with a diameter of around 50' (Reynoso et al. (2016), Aruga et al. (2022)). The 1.4 GHz radio continuum image compiled by Aruga et al. (2022) is displayed in Fig. 11, for which they used the same data as Reynoso et al. (2016) obtained with ATCA and the Parkes 64 m radio telescope. It is noted that the emission in the northeastern side of the shell is comparably strong and forms a flat edge, which is consistent with the distribution of X-ray emission (see Sect. 3.1) . Additionally, there are some brighter areas in the western part of the remnant. The thermal X-ray emission from Puppis A is found to be mostly confined to the region within the radio shell. Aruga et al. (2022) also analysed NANTEN CO and ATCA H I data to investigate molecular and atomic clouds linked to Puppis A. Figure 12 shows the integrated intensity maps of CO and H I in the velocity range from $8 - 20\,\mathrm{km\,s^{-1}}$. It is evident that H I and CO clouds are distributed all along the northeastern edge of the remnant, where both in X-rays and in the radio continuum emission map Puppis A shows a flat border. By comparing the radio continuum and X-ray emission to the distribution of the $8 - 20\,\mathrm{km\,s^{-1}}$ CO cloud, they find that the hot ionised gas and the CO cloud tend to be anti-correlated, which is interpreted as a sign of interaction between the SNR and the $8 - 20\,\mathrm{km\,s^{-1}}$ cloud. Furthermore, the line intensity ratio $R_{\mathrm{CO}} = {}^{12}\mathrm{CO(J = 2 - 1)}/{}^{12}\mathrm{CO(J = 1 - 0)}$ is enhanced in the north east of Puppis A ($R_{\mathrm{CO}} \sim 0.8 - 1.1$), which, for lack of any other source of heating, indicates that the gas was shock-heated by the SNR (Aruga et al., 2022). They observe the same

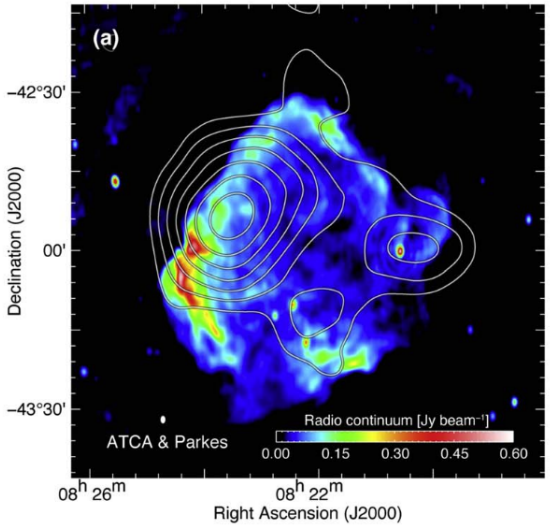

Figure 11: Map of the 1.4 GHz radio continuum emission from Puppis A (Aruga et al., 2022). The data was taken with ATCA and Parkes (Reynoso et al., 2016). The contours show the gamma ray emission at different levels.

anti-correlation in Hα emission, which supports the hypothesis.
They pinpoint the peak velocity of the $8 - 20\,\mathrm{km\,s^{-1}}$ cloud to $\sim 10 - 11\,\mathrm{km\,s^{-1}}$, which agrees with the results obtained by Reynoso et al. (2016) from H I absorption studies. A kinematic distance of $d \sim 1.4 \pm 0.1\,\mathrm{kpc}$ to the cloud is derived. Additionally, the averaged particle number densities of atomic and molecular hydrogen are estimated within the radio shell. For atomic hydrogen, $n(\mathrm{H\,I}) \sim 220\,\mathrm{cm^{-3}}$ and for molecular hydrogen, $n(\mathrm{H_2}) \sim 10\,\mathrm{cm^{-3}}$. These results lead to a total interstellar proton density of $n(\mathrm{p}) = 230\,\mathrm{cm^{-3}}$ (Aruga et al., 2022).

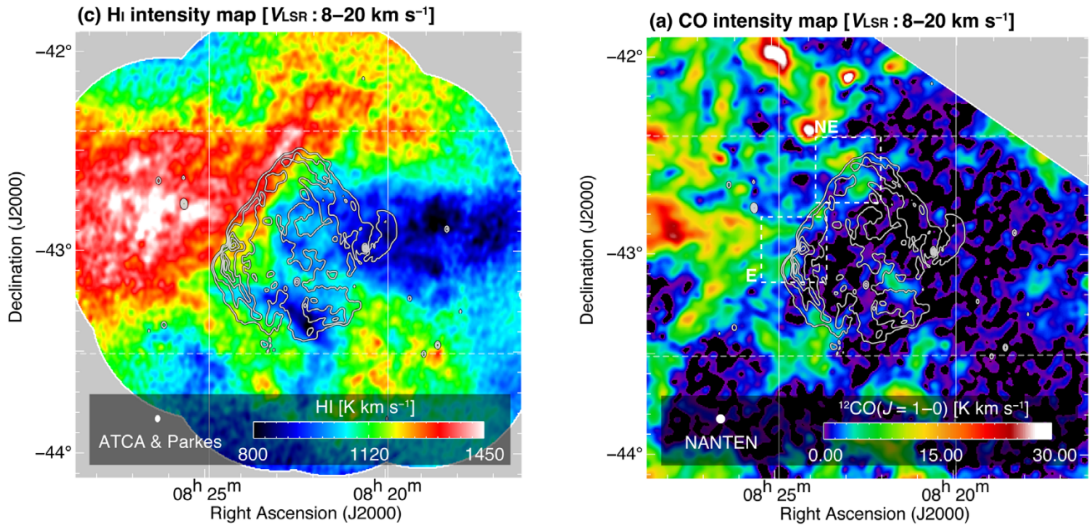

Figure 12: Distribution of H I (left) and CO (right) around Puppis A presented by Aruga et al. (2022). The images show the integrated intensity maps in the velocity range from $8 - 20\,\mathrm{km\,s^{-1}}$. The contours display the radio continuum emission.

3.3. Infrared observations

Puppis A was first discovered in infrared (IR) during the Infrared Space Observatory (IRAS) all-sky survey, which was launched in 1983 (Neugebauer et al., 1984). Later, observations with the Spitzer Space Telescope were carried out to obtain higher-resolution data and gain insights about the ISM that Puppis A is interacting with (Arendt et al., 2010). Figure 13 shows the IR emission as observed with Spitzer (green), as well as the X-ray emission in the 0.7-1.0 keV band to be able to compare the two wavelength ranges with each other, which is done in Dubner, G. et al. (2013) and Arendt et al. (2010), respectively. Arendt et al. (2010) find that the remnant is bright and has a complex structure with many filaments at $24\,\mu$m and $70\,\mu$m and measures an angular diameter of approximately $50'$. The BEK is the brightest feature also in IR. The overall brightness is found to decrease from north-east to south-west and the integrated IR flux results in $9 \times 10^{-8}\,\mathrm{erg\,s^{-1}\,cm^{-2}}$, which corresponds to a luminosity of $1.4 \times 10^4\,L_\odot$ at an assumed distance of 2.2 kpc. The emission at both above-mentioned wavelengths correlates very well with the observed X-ray emission across all spatial scales, although the correlation is somewhat less pronounced in the southern part of Puppis A (Dubner, G. et al., 2013). However, Arendt et al. (2010) note that the IR data do not correlate very well with the radio emission, particularly when looking at small spatial scales. Arendt et al. (2010) and Dubner, G. et al. (2013) also compared the X-ray emission from Puppis A to Spitzer IR data at $160\,\mu$m. Figure 14 again shows the X-ray emission in the 0.7-1.0 keV band in red and the IR emission at $160\,\mu$m in blue. From the remnant itself, no emission at $160\,\mu$m is detected. Instead, most of the emission originates from the region adjacent to the northeastern edge of the SNR. Dubner, G. et al. (2013) believe that this emission

is caused by a nearby molecular cloud, where the larger dust grains that this emission corresponds to are still intact and have not been destroyed by the passing of the shock from the SN.

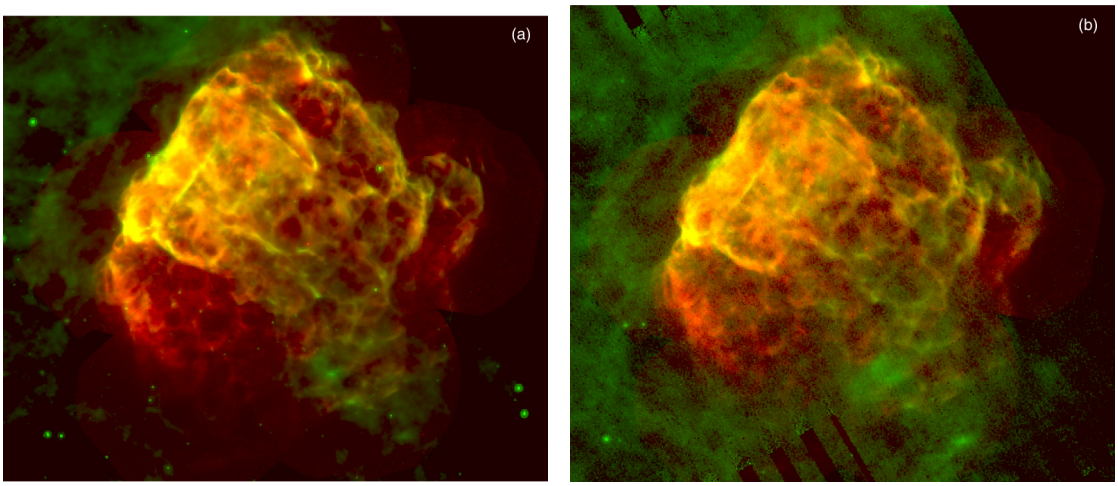

Figure 13: Two-colour images of Puppis A published by Dubner, G. et al. (2013) showing the X-ray emission in the 0.7-1.0 keV band (red) and the IR emission (green) at 24 μm (left) and at 70 μm (right). The IR Spitzer data was taken from Arendt et al. (2010).

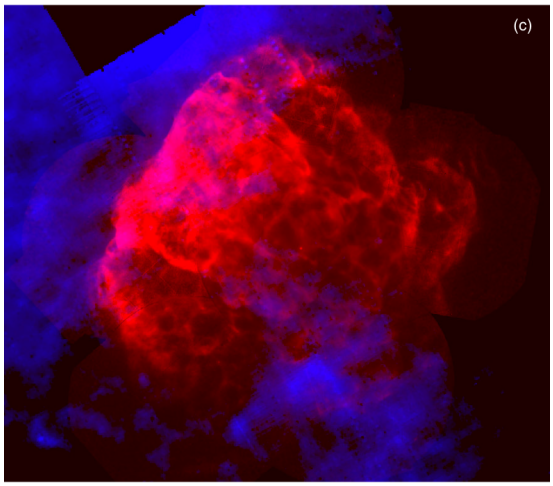

Figure 14: Two-colour image of Puppis A published by Dubner, G. et al. (2013) showing the X-ray emission in the 0.7-1.0 keV band (red) and the IR emission (green) at 160 μm. The IR Spitzer data was taken from Arendt et al. (2010).

4. Hydrodynamic simulations with PLUTO

The PLUTO code [1] used throughout this work is a numerical code developed by Mignone et al. (2007) specifically for computational astrophysics and fluid dynamics simulations with high Mach number flows. In this work, PLUTO versions 4.4-patch1 and 4.4-patch2 are used. In the following, the code structure will be outlined focussing on the physical modules applied in this work. In the second part of this chapter, the problem setup and configuration of PLUTO will be described based on the modification of one of the two-dimensional hydrodynamics (HD) test problems provided with the PLUTO distribution. A detailed description on how to use the code can be found in the PLUTO User's Guide (PLUTO Team, 2021).

4.1. The PLUTO code

As is stated in the user's guide (PLUTO Team, 2021), PLUTO integrates a system of conservation laws, which generally can be expressed as

$$\frac{\partial U}{\partial t} + \nabla \cdot T_h = \nabla \cdot T_p + S(U). \tag{34}$$

In Eq. 34, U is a set of conservative quantities, $T_h(U)$ stands for the hyperbolic flux tensor, T_p for the parabolic diffusion flux tensor and $S(U)$ for the source terms. A detailed description of what these terms stand for was presented in Sect. 2.3.1. For convenience, the state vector U is converted to a set of primitive variables V, which are then used to set the initial and boundary conditions. The conservation law in Eq. 34 is integrated numerically by means of the finite volume (FV) formalism which describes the evolution of the respective quantities averaged over the volume of a computational cell in time. The general approach implemented in the code, that is the code's infrastructure, can be broken down into a number of consecutive steps as is shown in Fig. 15 (Mignone et al., 2007).
As already mentioned above, in a first step the volume averages U are converted to a set of primitive quantities V. Secondly, the variables are interpolated, extrapolated or both to calculate left and right states $V_{+,\mathrm{L}}$ and $V_{+,\mathrm{R}}$ in each computational cell, followed by the solution of a Riemann problem between $V_{+,\mathrm{L}}$ and $V_{+,\mathrm{R}}$, which results in the numerical flux function F_+ at the interfaces of the cell. Lastly, the solution is evolved in time (Mignone et al., 2007).
The calculation of left and right states in each cell is implemented via a so-called reconstruction algorithm (Mignone et al., 2007), while a time stepping routine determines the evolution of the solution between to consecutive time steps. The specific algorithms that are used can be chosen when configuring the code (PLUTO Team, 2021).
PLUTO is designed in a modular structure, allowing for a number of different physics modules to be included in the simulation run depending on the nature of the problem at hand. Consequently, the form of all the variables in Eq. 34 is defined by the

[1] http://plutocode.ph.unito.it

physics modules that are chosen. The modules provided are classical hydrodynamics (HD), magnetohydrodynamics (MHD), special relativistic hydrodynamics (RHD), special relativistic MHD (RMHD), resistive relativistic MHD (ResMHD), and relativistic/non-relativistic radiation MHD. Moreover, it is possible to take a number of additional physical processes into account, that is for example viscosity, thermal conduction and resistivity, radiative losses/cooling, ionization/recombination processes, different equations of state, gravity and shearing box equations (PLUTO Team, 2024). Irrespective of which physics modules are selected, the steps described in Fig. 15 are always followed. However, the physical module gathers the set of algorithms necessary to calculate the explicit terms to solve the equations. This includes, for example, the Riemann solver or the routines to convert U to V (Mignone et al., 2007).

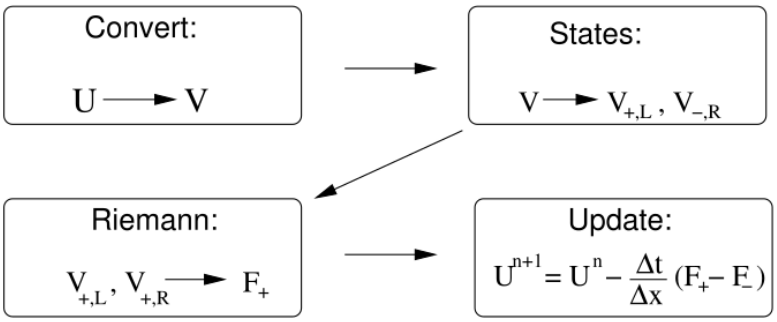

Figure 15: Flow diagram illustrating PLUTO's general infrastructure (Mignone et al., 2007).

PLUTO operates on a numerical grid, the geometry and dimensions of which can be chosen according to the requirements of the model setup. The available options are Cartesian coordinates ($\{x_1, x_2, x_3\} = \{x, y, z\}$), cylindrical axisymmetric coordinates ($\{x_1, x_2\} = \{r, z\}$), polar cylindrical coordinates ($\{x_1, x_2, x_3\} = \{r, \phi, z\}$), or spherical coordinates ($\{x_1, x_2, x_3\} = \{r, \theta, \phi\}$). Except for the cylindrical axisymmetric coordinates, which can only be used in one and two dimensions, all geometries are applicable in up to three dimensions. The grid spacing is uniform by default, but can also be stretched, meaning geometrical or logarithmic. It should be mentioned that a static grid version of the code and a version with adaptive mesh refinement (AMR, see Mignone et al. (2012)) are available. Unlike in the static grid version, the computational grid in the AMR version is not fixed, but is adapted dynamically in space and time, which can be beneficial for problems with largely varying scales. However, this work exclusively uses the static grid version, which is fully written in the programming language C. The code can be run on a single processor or on multiple processors in parallel, in which case the computational domain is divided into a number of subdomains of equal size, and each is allocated to one processor. Parallelisation is implemented via the Message Passing Interface (MPI) Library (PLUTO Team, 2021).

4.1.1. The HD module

With the HD module, which is used for all simulations throughout this work, the Euler or Navier-Stokes equations of classical fluid dynamics are implemented in the PLUTO code. The physical derivation of the Euler equations and how they are extended to the Navier-Stokes equations is presented in Sect. 2.3.1, based on which Eq. 34 takes the form

$$\frac{\partial}{\partial t}\begin{pmatrix}\rho\\ \boldsymbol{m}\\ E_\mathrm{t}+\rho\Phi\end{pmatrix}+\nabla\cdot\begin{pmatrix}\rho\boldsymbol{v}\\ \boldsymbol{m}\otimes\boldsymbol{v}+p\mathbf{I}\\ (E_\mathrm{t}+p+\rho\Phi)\boldsymbol{v}\end{pmatrix}^T=\begin{pmatrix}0\\ -\rho\nabla\Phi+\rho\boldsymbol{g}\\ \boldsymbol{m}\cdot\boldsymbol{g}\end{pmatrix} \tag{35}$$

with the mass density ρ, the momentum density $\boldsymbol{m}=\rho\boldsymbol{v}$, the velocity v and the thermal pressure p (PLUTO Team, 2021). The 3×3 identity matrix is represented by $\mathbf{I}$. The energy density E_t is given by

$$E_\mathrm{t}=\rho e+\frac{\boldsymbol{m}^2}{2\rho}, \tag{36}$$

where e is the internal energy (PLUTO Team, 2021). Equation 35 also takes into account body forces. These add source terms to the momentum and energy equations (see Sect. 2.3.1), which are expressed in terms of the gravitational potential Φ and the acceleration vector $\boldsymbol{g}$ (PLUTO Team, 2021). It has to be noted that contributions from body force are only computed if specifically enabled in the configuration of the code, which is not the case in the simulations in this work.
To provide closure to the respective system of differential equations, pressure p and mass density ρ are related via an equation of state $p=p(\rho,\rho e)$. Throughout this work, the ideal equation of state is applied, which is valid under the assumption of a calorically ideal gas and can be expressed as

$$p=\rho e(\Gamma-1) \tag{37}$$

with the adiabatic index Γ (see also Sect. 2.3.1) (PLUTO Team, 2021). For a non-relativistic monoatomic gas, as mostly present in supernova remnant physics, $\Gamma=\frac{5}{3}$ (Vink, 2020). The set of primitive variables in the HD module is given by $\boldsymbol{V}\equiv(\rho,\ \boldsymbol{v},\ p)^T$.
The Euler equations can be extended to the Navier-Stokes equations by taking into account viscous effects (see Sect. 2.3.1), which would add two parabolic diffusion terms to Eq. 35. Similar to the body forces, viscosity can be enabled or disabled when configuring PLUTO (PLUTO Team, 2021).

4.1.2. Radiative cooling

PLUTO also allows for time-dependent radiative cooling effects to be included when configuring the code. Radiative losses for optically thin plasma can be administered in several different ways. Throughout this work, the tabulated cooling module was used. In general, radiative losses result in a source term in the energy equation (see Sect. 2.3.1),

which depends on the cooling function Λ (PLUTO Team, 2021):

$$\frac{\partial(\rho e)}{\partial t} = -\Lambda(n, T). \tag{38}$$

As previously, ρ represents the mass density and e the internal energy. In case of tabulated cooling, the cooling function is not calculated analytically but provided in the form of a table containing discrete values for the temperature T and $\widetilde{\Lambda}(T)$ so that

$$\Lambda = n^2 \widetilde{\Lambda}(T). \tag{39}$$

Here, n stand for the particle number density and can be calculated from the mass density, the mean molecular weight μ, and the proton mass m_p as $n = \frac{\rho}{\mu m_\mathrm{p}}$ (PLUTO Team, 2021). As an alternative, a user-defined cooling function $\Lambda = \Lambda(\boldsymbol{V})$ depending on a vector of primitive variable $\boldsymbol{V}$ can be provided (PLUTO Team, 2021).

4.2. Problem setup in PLUTO

The PLUTO distribution comes with a number of test problems, which can be used to learn how to configure the code and run some first simulations. Here, the HD two-dimensional blast problem is used as a starting point to become familiar with setting up the code and is slightly modified to represent a supernova remnant expanding into an inhomogeneous ISM. The model is a simplified version of the SNR IC443 as presented by Ustamujic et al. (2021).

4.2.1. Configuring PLUTO

To configure PLUTO for a specific physical problem, four basic files need to be present in the local working directory, namely the `definitions.h`, `pluto.ini`, and `init.c` files, as well as a `makefile`.

`definitions.h` The `definitions.h` is the problem header file, which contains all the directives needed at compilation time for the problem at hand. This includes for example the physics module that should be used (HD, MHD,...), the geometry (Cartesian, cylindrical,...) and dimensions of the problem. Additional physics modules such as viscosity, body force, or radiative cooling are also enabled or disabled via the header file. Moreover, the reconstruction and time stepping algorithms are selected in this file. Suitable combinations of available time-stepping and reconstruction algorithms recommended in the PLUTO user's guide are listed in Table 2. In this work, the Runge-Kutta 3 (RK3) time-stepping together with parabolic reconstruction was used. Furthermore, the number of passive tracers is chosen in `definitions.h`, which can be used to track different plasma components throughout the simulation (PLUTO Team, 2024). The `definitions.h` file is edited via a python routine called `setup.py`. The only exception are user-defined constants, which can be added here but need to be changed manually. This usually includes

the constants providing physical units for the model setup. PLUTO computes all quantities in code units, which are then converted to c.g.s units with the respective constants specified in `definitions.h`. Three units must be provided, namely `UNIT_DENSITY` (ρ_0 in $\mathrm{g\,cm^{-3}}$), `UNIT_LENGTH` (L_0 in cm), and `UNIT_VELOCITY` (v_0 in $\mathrm{cm\,s^{-1}}$). All other quantities can be expressed as a combination of ρ_0, L_0, and v_0 and then converted to c.g.s units accordingly. An example are unit time $t_0 = \frac{L_0}{v_0}$ and unit pressure $p_0 = \rho_0 v_0^2$. It has to be noted that the scaling units should be chosen so that the numbers in code units are reasonable, meaning not extremely small or large, to avoid misinterpretation by the numerical algorithms (PLUTO Team, 2021).

Reconstruction	**Time stepping**	**Notes**
`LINEAR`	`RK2`	This is the default setup, which provides compatibility with most algorithms, coordinates, and physics modules.
`PARABOLIC`	`RK3`	Comparable to the first setup, runs slightly more stable and the computational cost is higher.
`PARABOLIC`	`ChTr`	Recommended for HD, MHD, and RHD simulations in Cartesian or cylindrical geometry.
`LINEAR`	`ChTr, HANCOCK`	Amongst the most sophisticated algorithms provided. Fitting for Cartesian and cylindrical geometry in the HD, RHD, and MHD modules.

Table 2: Recommended reconstruction and time stepping algorithm configurations. Characteristic Tracing is abbreviated with ChrTr and Runge-Kutta 2/3 with RK 2/3. The table was adapted from PLUTO Team (2021).

`pluto.ini` The `pluto.ini` file contains all the runtime parameters that are required for the computation during the simulation run, which are organized in nine separate blocks. This includes among others a block for the grid parameters, such as the number of grid points, the spacing of the grid and the size of the computational domain. Furthermore, the boundary conditions are chosen in this file, which determine how the solution behaves at the borders of the computational domain. There is one block dedicated to controlling the time-stepping and thereby essentially the simulation time, as well as a block for the Riemann solver. In the HD module, a total of six different Riemann solvers is available (PLUTO Team, 2024). The one applied in this work is the `roe` solver. The output is also controlled via the `pluto.ini`, meaning for example the data format of the output files and the frequency with which they are produced. Additionally, user-defined parameters set up in the `definitions.h` file are provided with initial values here (PLUTO Team, 2021).

`init.c` The `init.c` file belongs to the source files of PLUTO and implements the functions to configure the fluid according to the specific problem. Firstly, the `Init()` function provides a possibility for setting up the initial conditions locally for each computational cell dependent on the spatial coordinates x_1, x_2, and x_3. As arguments, it takes x_1, x_2, and x_3, as well as v, which is a pointer to the set of primitive variables (in the HD case to the density ρ = `v[RHO]`, the pressure p = `v[PRS]`, and the three components of velocity v_1 = `v[VX1]`, v_2 = `v[VX2]`, v_3 = `v[VX3]`). Throughout this work, the initial conditions are always implemented via the `Init()` function. Alternatively, the function `InitDomain()` can be used, which works as a multidimensional loop over the whole domain and is especially useful when the value in a computational cell depends on the neighbouring cells or if multiple cell values need to be integrated. `InitDomain()` also enables reading the initial conditions from an external file. For completeness it should be mentioned that the `init.c` file also contains several other functions, for example to implement user-defined boundary conditions or to reduce data during runtime. However, in this work only `Init()` was made use of (PLUTO Team, 2021).

`makefile` The `makefile` is necessary to compile and link the C source code and create the executable `pluto`. It is generated by the `setup.py` routine and can be adapted appropriately to the problem, meaning for example the C compiler that is used or whether the code is to be run with MPI in parallel or on a single processor (PLUTO Team, 2021).

If all files are set up correctly, the code is ready to be compiled using the `make` command. This creates the executable `pluto`, which is then used to start the simulation. Any PLUTO source files that are copied to the current working directory are prioritised when compiling the code, which is useful in case any modifications need to be made. Additionally, if the tabulated cooling module is enabled, a cooling table must be provided within the directory from which the code is executed.
The visualisation of the output is done with the pyPLUTO python package, which is also provided with the PLUTO distribution and allows to load and process the binary output data files as numpy arrays.

4.2.2. A simple blastwave problem

In this chapter, the configuration of PLUTO will be discussed in further detail based on a concrete example. The model setup described here draws on the work presented by Ustamujic et al. (2021). They did 3D HD simulations of the mixed-morphology SNR IC443 and developed a model of the inhomogeneous ISM that the remnant is expanding into, which is shown schematically in Fig. 16. It is assumed, that the inhomogeneities in the ISM are made up of a toroidal molecular cloud (shown in red in Fig. 16) and a atomic cloud shaped like a cap above the explosion site (shown in blue in Fig. 16). The ejecta region is implemented as spherically symmetric and slightly off-centre of the torus, starting at an age of 122 yr.

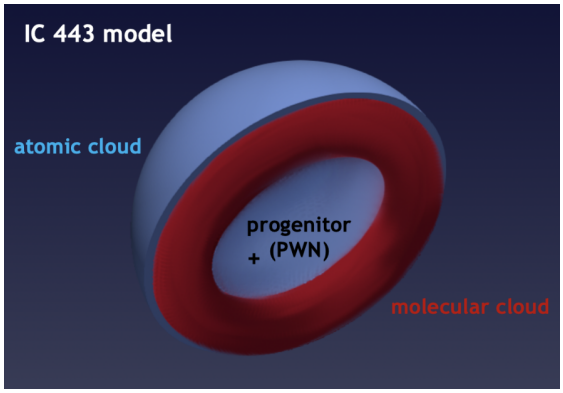

Figure 16: Schematic illustration of the initial conditions for the model of the IC443 presented by Ustamujic et al. (2021). The atomic cloud forms a kind of cap around the explosion site and is depicted in blue, while the molecular cloud is assumed as a toroidal structure shown in red. The location of the progenitor is marked with a black cross.

Here, the goal is to develop a simplified 2D model setup based on the 3D model by Ustamujic et al. (2021) to demonstrate how to set up and configure the code. It has to be noted, that the aim is not to accurately reproduce actual parameters of IC443 derived from observations, but simply to use the model presented by Ustamujic et al. (2021) as a guideline to grow familiar with PLUTO.
As a starting point, the HD blast wave test problem provided with the PLUTO distribution is used. In this case, the blast wave is generated by implementing a high pressure in the ejecta region (see Fig. 17). All the other primitive variables (density and velocities) are constant over the entire computational domain.
The geometry used in this problem is 2D Cartesian and all the boundary conditions are therefore set to 'outflow', which means the gradient of all scalar and vector variables across the boundaries of the computational domain vanish (PLUTO Team, 2021). Since it is a 2D simulation, the third spatial coordinate x_3 is automatically set to zero. However, the respective vector component (for example vx_3) is integrated regardless, which means the 3D structure of the 2D model needs to be considered in any case (PLUTO Team, 2021). This means the circular region with higher pressure in Fig. 17 in fact represents a tube in Cartesian coordinates and not a sphere as one might assume initially.
To simplify the 3D model of IC443 by Ustamujic et al. (2021), the ejecta region is placed right in the centre of the toroidal molecular cloud, which makes the setup symmetric with respect to the x_2 axis. Therefore, it is now possible to move from Cartesian to cylindrical geometry, which allows to simulate only half of the domain and save computational cost. In this case, the boundary condition at the beginning of the x_1 axis, which is the symmetry axis, has to be changed from 'outflow' to 'axisymmetric' the ensure the variables behave correctly at the borders of the domain.
The coordinates that need to be considered now are $\{x_1, x_2\} = \{r, z\}$. The third spatial coordinate, which is automatically set to zero in two dimensions but needs to be taken into

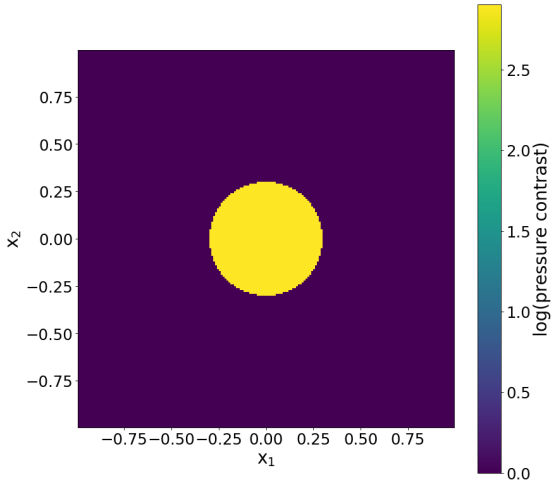

Figure 17: Initial pressure distribution of the HD blast test problem provided with the PLUTO distribution. All quantities are given in code units.

account regardless, is the angle φ describing the rotation around the z-axis. This means in order to represent a spherical ejecta region in the centre of the torus, a semi-circle with radius $r = \sqrt{x_1^2 + x_2^2}$ cut in half by the x_2 axis needs to be implemented. Similarly, a torus is described by a full circle with an offset with respect to the x_2 axis and the cap representing the atomic cloud is considered as a quarter annulus, again cut in half by the x_2 axis. The initial pressure and density distributions are displayed in the left and middle panels of Fig. 18. For the molecular cloud, a density contrast of 10^3 and for the atomic cloud a density contrast of 10 with respect to the rest of the domain is chosen. The constants `UNIT_DENSITY`, `UNIT_VELOCITY`, and `UNIT_LENGTH` are specified in the `definitions.h` as listed in Table 3 in line with the length, density, and velocity scales expected for SNRs. The extent of the computational domain is changed in the `pluto.ini` file to 1 pc in the x_1-direction and 2 pc in the x_2-direction. The grid resolution is set to 256 grid points along x_1 and 512 grid points along x_2 with uniform spacing.

`UNIT_DENSITY`	$1.67 \times 10^{-24}\,\mathrm{g\,cm^{-3}} = m_\mathrm{p}$
`UNIT_VELOCITY`	$1 \times 10^{8}\,\mathrm{cm\,s^{-1}}$
`UNIT_LENGTH`	$3.086 \times 10^{18}\,\mathrm{cm} = 1\,\mathrm{pc}$

Table 3: Units defined in the `definitions.h` file to convert the quantities in PLUTO from code units to c.g.s. units. Here, m_p denotes the proton mass, which in this case means that the density in code units is equal to the proton number density.

The initial ejecta radius is chosen to be $R_\mathrm{ejecta} = 0.3\,\mathrm{pc}$. The torus is placed at a distance of 0.6 pc from the centre and the cap has an inner radius of $R_\mathrm{inner} = 0.5\,\mathrm{pc}$ and an outer radius of $R_\mathrm{outer} = 0.7\,\mathrm{pc}$.

The right panel of Fig. 18 shows the initial temperature distribution, which is calculated from the pressure p and particle number density n as follows (PLUTO Team, 2021):

$$T = \frac{p}{2k_{\mathrm{B}}n}. \tag{40}$$

Here, k_{B} denotes the Boltzmann constant and n is equal to the density in code units since the unit density is set to m_{p} and the mean molecular weight $\mu = 1$. Evidently, the temperature in the molecular and atomic clouds is much lower than in the surrounding medium. The pressure in the ejecta region was fixed so that the initial ejecta temperature is $\sim 10^8\,\mathrm{K}$.
An ejecta mass of $4\,\mathrm{M}_\odot$ was chosen and the kinetic explosion energy is defined as $1 \times 10^{51}\,\mathrm{erg}$, the canonical value for SN explosions (see Sect. 2.2). Since for now the ejecta density is uniform over the entire ejecta region, the density is chosen so that $V \cdot \rho = 4\,\mathrm{M}_\odot$. Again, despite this being a 2D setup, the third dimension needs to be considered regardless. This means V in this case is the volume of the sphere that results from replicating the semi-circle describing the ejecta region along the φ axis. The same is true for the kinetic explosion energy $E_{\mathrm{kin}} = \frac{mv^2}{2}$. However, in case of the velocity, a linear profile in the radial direction was implemented, as shown in the left panel of Fig. 22. The maximum velocity v_{max} was chosen so that $\int_V \rho v(r)^2\,\mathrm{d}V = 10^{51}\,\mathrm{erg}$ with $v(r) = v_{\mathrm{max}} \cdot \frac{r}{R_{\mathrm{ejecta}}}$. From this, the initial age at the start of the simulation can be estimated as $t_0 = \frac{R_{\mathrm{ejecta}}}{v_{\mathrm{max}}} \approx 45\,\mathrm{yr}$.
Figure 21 shows the three passive tracers that are implemented to track the different plasma component throughout the simulation. Evidently, the respective tracer is set to one in the initial conditions in the region that the different plasma components are initialised. In this case, the left panel shows the tracer for the ejecta, the middle panel the tracer for the atomic cloud, and the right panel the tracer for the molecular cloud.

The simulation is now run for $\sim 78\,\mathrm{yr}$ until the blast wave reaches the edges of the computational domain. The density, pressure, and temperature distributions at $t \approx 123\,\mathrm{yr}$ are shown in Fig. 20 and Fig. 21 shows the three tracers after 78 yr of simulation time. From the density, pressure, and temperature distributions it is evident that a forward shock has developed, that runs into the ambient ISM including the atomic and molecular clouds. Additionally, a reverse shock, slowing down the ejecta, and subsequentially a contact discontinuity have formed. In the shocked medium the pressure, temperature and density are significantly higher than in the unshocked ejecta in the interior of the remnant, as well as in the unshocked ISM. The shocked region is also visible in the velocity and pressure profiles shown in the right panels of Figs. 22 and 23, respectively. The density map in Fig. 20 shows Rayleigh-Taylor instabilities occurring at the contact discontinuity, as is described in Sect. 2.2.2. These hydrodynamical instabilities are also apparent in the tracer distributions in Fig. 21.

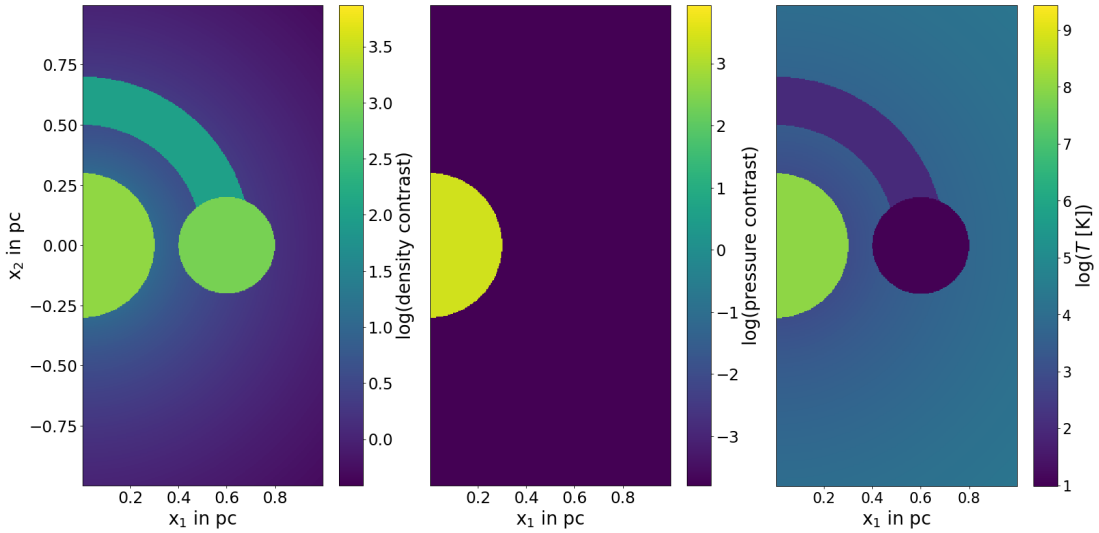

Figure 18: Initial 2D distributions of density (left), pressure (middle), and temperature (right) for the simplified model setup of IC443 in cylindrical geometry. A numerical grid resolution of 256×512 grid points was chosen. All three figures share the same x_2 axis.

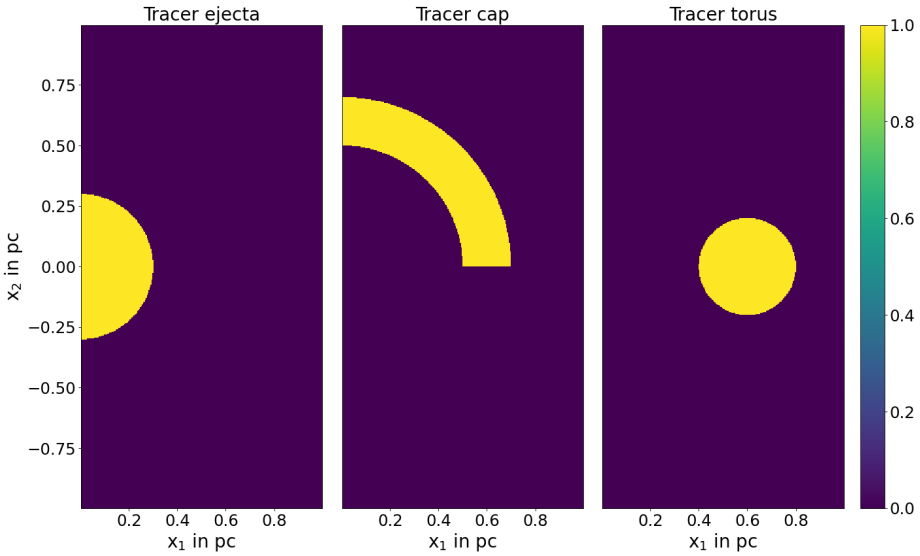

Figure 19: Initial 2D distributions of the passive tracers for the simplified model setup of IC443 in cylindrical geometry. The left panel shows the tracer for the ejecta, the middle panel the tracer for the atomic cloud shaped like a cap, and the right panel the tracer for toroidal molecular cloud.

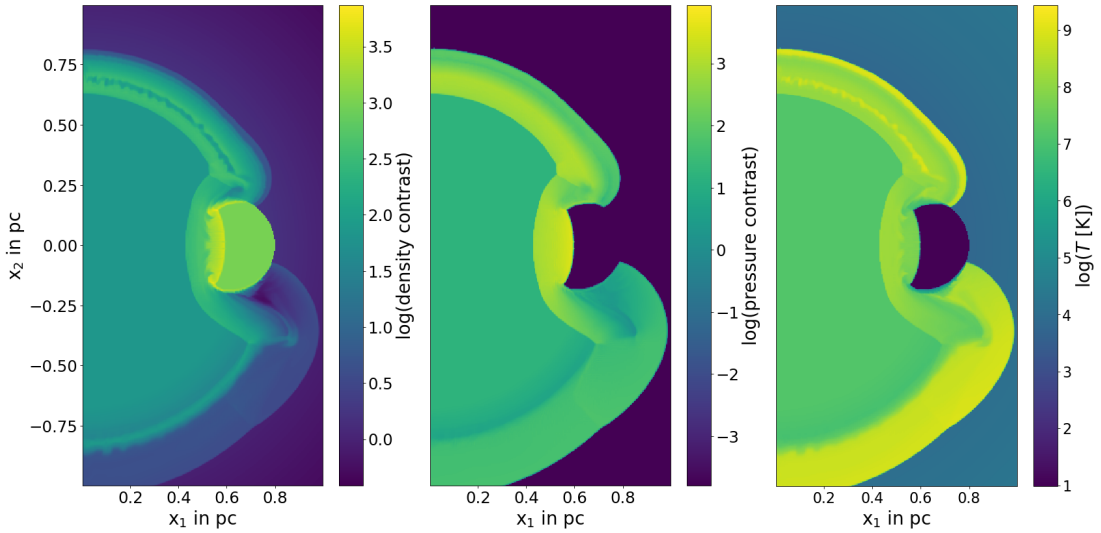

Figure 20: Distributions of density (left), pressure (middle), and temperature (right) for the simplified 2D model setup of IC443 in cylindrical geometry after 78 yrs. A numerical grid resolution of 256×512 grid points was chosen. All three figures share the same x_2 axis.

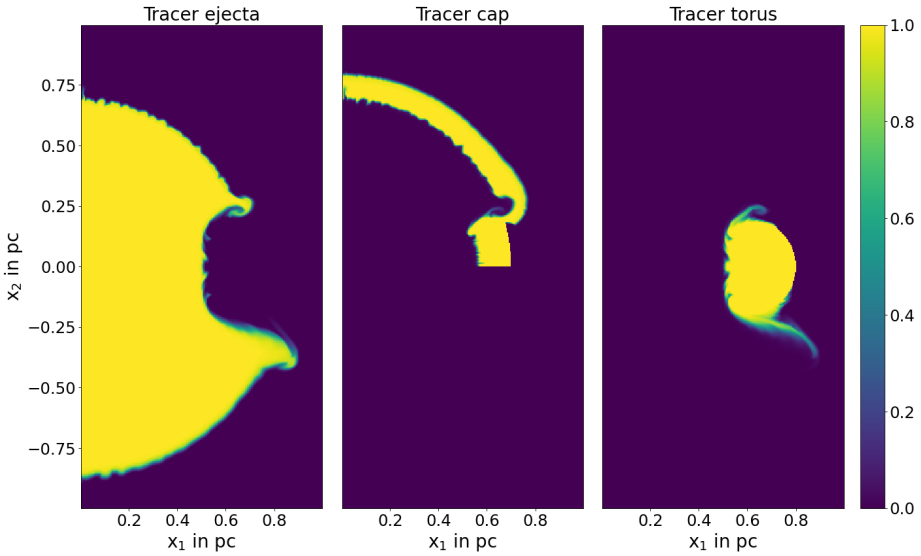

Figure 21: Distributions of the passive tracers for the simplified 2D model setup of IC443 in cylindrical geometry after ~ 78 yrs. The left panel shows the tracer for the ejecta, the middle panel the tracer for the atomic cloud shaped like a cap, and the right panel the tracer for toroidal molecular cloud.

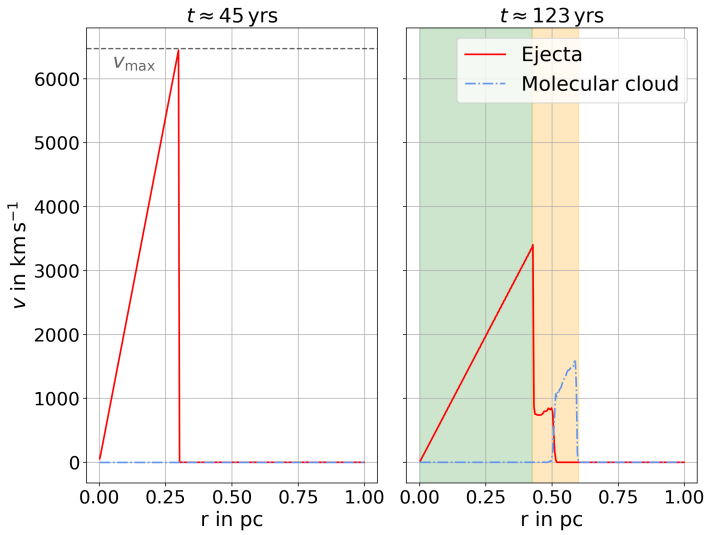

Figure 22: Velocity profiles along the x_1 axis at $x_2 = 0$ for the simplified 2D model setup of IC443. The left figure shows the initial velocity profile. On the right the same velocity profile after ~ 78 yrs of simulation time is shown for the ejecta (red solid line) and the molecular cloud (blue dashed-dotted line). The freely expanding ejecta are highlighted in green. The area shaded in orange shows, where the forward shock is accelerating the molecular cloud, while the ejecta are decelerated by the reverse shock. The unshaded area on the right marks the unshocked ISM.

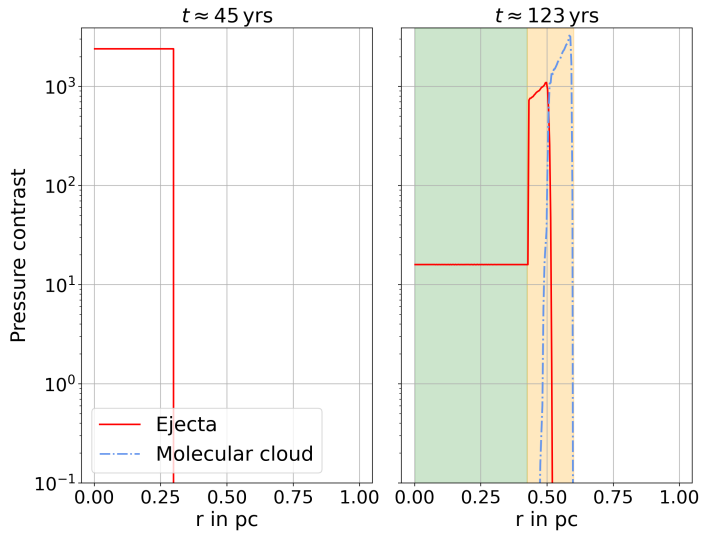

Figure 23: Pressure profiles along the x_1 axis at $x_2 = 0$ for the simplified 2D model setup of IC443. The left figure shows the initial pressure profile along the x_1 axis. On the right, the same pressure profile after ~ 78 yrs of simulation time is shown for the ejecta (red solid line) and the molecular cloud (blue dashed-dotted line). The freely expanding ejecta are highlighted in green. The shocked ejecta and ISM are shaded in orange and the unshaded area on the right marks the unshocked ISM.

5. Hydrodynamic simulations of Puppis A

In the following section, the development of a hydrodynamical model setup for Puppis A in PLUTO will be presented. The aim for the model is to reproduce the observational properties of Puppis A, specifically its X-ray morphology, as best as possible. This allows to draw conclusions about the parameters of the SN explosion and the ISM structures that the remnant is interacting with.
Section 5.1 provides a summary of the observational constraints for the HD model of Puppis A and gives a first outline of a possible model setup. In Sect. 5.2 the results of the preliminary two-dimensional (2D) simulations are summarised before moving on to the three-dimensional (3D) model setup and the synthesis of the X-ray emission generated from the models in Sect. 5.3. In Sect. 5.4 the synthetic X-ray spectra resulting from the most promising simulation runs are analysed.

5.1. Observational constraints constraints and first model outline

In order to develop a suitable hydrodynamical model setup for Puppis A, it is necessary to use constraints on parameters like the explosion energy, the distance and diameter, or the age of the remnant that can be derived from multi-wavelength observations (see Sect. 3 for details). Additionally, the observations provide crucial insights on the density and structures of the surrounding ISM. In the case of Puppis A, it is believed that the remnant is interacting with an interstellar cloud of atomic and molecular gas along its northeastern border (see Sect. 3.2). Table 4 shows a summary of the observational constraints that were primarily considered for the initial conditions of the HD model setup.

Model parameters	**Constraints from observations**
Age	$\sim 4000\,\mathrm{yr}$ (Mayer et al., 2020)
Diameter and distance	$21.2\,\mathrm{pc}$ (Mayer et al., 2022) at a distance of $1.3\,\mathrm{kpc}$ (Reynoso et al., 2016)
Explosion energy	$(1.22-1.36)\times10^{51}\mathrm{erg}$ at an assumed radius of $r = 10.6\,\mathrm{pc}$ and an age of $4000\,\mathrm{yr}$ (Mayer et al., 2022)
ISM density	Average pre-SN ISM density $\rho \approx 1.1\times10^{-24}\,\mathrm{g\,cm^{-3}}$, mass of emitting plasma $M_{\mathrm{ISM}} \approx 78-87\,\mathrm{M_\odot}$ at an assumed distance of $1.3\,\mathrm{kpc}$ (Mayer et al., 2022)
Interacting cloud	Proton density of $n_{\mathrm{p}} \approx 230\,\mathrm{cm^{-3}}$ (Aruga et al., 2022)

Table 4: Different initial model parameters that were derived from the observations of Puppis A. This table serves as a summary, for details see Sect. 3.

Since in X-ray images (e.g Dubner, G. et al. (2013), see Sect. 3.1), Puppis A seems to be somewhat rectangular in shape, with at sharp edge at the north-eastern border, the first

idea for the geometry of the model is to place the ejecta region inside a higher density torus, which represents the molecular/atomic cloud. In this scenario, the expanding ejecta is then expected to be confined within the cloud, which could roughly account for the rectangular shape observed in X-rays. The cross section of the torus was chosen as an ellipse with semi-minor axis a and semi-major axis c. A schematic illustration of the model geometry is shown in Fig. 24.
It should be stressed, that Fig. 24 is not an accurate representation of the initial density distribution, but only serves to outline the geometry of the model. The X-ray morphology of Puppis A is not symmetrical: the remnant shows a flat border in the north-east, yet seems to be expanding more or less freely in the south-west. This means that the density in the cloud is expected to be not uniform, but substantially higher on one side of the torus and blending into the lower-density ISM on the other side, which will be taken into account in the 3D simulations in Sect. 5.3.

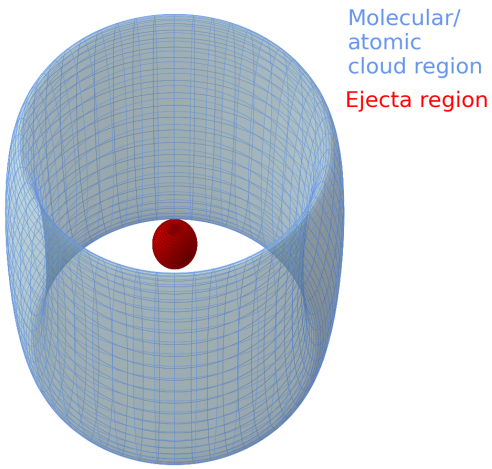

Figure 24: Schematic outline of the geometry of the first model setup for Puppis A. The cloud is implemented as an elliptical torus (blue) with the spherical ejecta region in the centre (red). It has to be noted that this figure only illustrates the geometry of the model and does not serve as an accurate representation of the initial density distribution.

5.2. Preliminary 2D simulations

As already mentioned, it is evident from the observations that Puppis A is not symmetrical and it will be necessary to move to 3D Cartesian geometry eventually. However, before extending the model to three dimensions, a few of the model parameters can already

be explored in 2D simulations. Similar to the simple model of IC443 presented in Sect. 4.2.2, this is done in 2D cylindrical geometry, which means in this case the density in the toroidal cloud is, in fact, uniform. To start with, this is a reasonable approximation. If applicable, it is generally advisable to begin with 2D simulations, since the computational cost, and subsequently the computation time, are substantially lower. The two parameters varied in this case are the semi-major axis c of the elliptical torus representing the cloud, as well as the ejecta mass.

5.2.1. Cloud extent

For the cloud extent, three different values for the semi-major axis c of the elliptical torus are tested, namely $c = 12.5\,\mathrm{pc}$, $c = 9\,\mathrm{pc}$, and $c = 5\,\mathrm{pc}$. The semi-minor axis a was kept at $a = 1.3\,\mathrm{pc}$ in all three simulation runs. Since the cloud that Puppis A is interacting with is likely not yet shocked completely, a is not a parameter that needs to be varied. A spherical ejecta region with an initial radius R of 0.3 pc and an ejecta mass of $10\,\mathrm{M}_\odot$ are assumed. The radial density profile follows the ejecta density profile for core-collapse SNe presented by Chevalier (2005), which exhibits a plateau in the innermost region, followed by two power law sections with index $m = 1$ and $b = 11.5$, respectively. For the surrounding ISM, a uniform density of $1.1\,\mathrm{g\,cm^{-3}}$ (see Table 4) is chosen. The initial density distributions for the three different simulations are shown in Fig. 25. Additionally, to make the simulations more realistic and help hydrodynamical instabilities to develop, cell-by-cell density "clumps" are implemented in the ejecta region. Figure 26 shows the density distribution in the ejecta region in detail. The density values across all computational cells follow a random power law distribution within the interval $10^{[-1,1]}$ superimposed on the radial density profile by Chevalier (2005), which is a simple way of introducing clumping in the ejecta, presented by Orlando et al. (2012). Since the density distribution is now randomised, the ejecta mass is fixed by means of a normalisation factor N_ej, so that

$$N_\mathrm{ej} \cdot \sum_i m_i = N_\mathrm{ej} \cdot \sum_i \rho_i V_i = 5\,\mathrm{M}_\odot, \tag{41}$$

where m_i is the mass of the ith cell, ρ_i is the mass density in the ith cell, and V the cell volume. Since the third dimension needs to be considered regardless of this being a two-dimensional simulation, the volume is expressed as $V = 2\pi r_i \Delta x_i$, with the radius r_i and the area Δx_i of the ith cell. Similarly, a kinetic explosion energy of $E_\mathrm{kin} = 1 \times 10^{51}$ erg is assigned by choosing the maximal initial ejecta velocity v_max accordingly. The radial velocity profile in the ejecta is linear with respect to the radius r and the slope is determined by v_max:

$$v(r) = \frac{v_\mathrm{max}}{R} \cdot r. \tag{42}$$

Since the kinetic energy in each cell is also dependent on the random cell mass m_i, setting the correct explosion energy is achieved by summing up the energy contributions of all cells in the ejecta region and calculating v_max, so that

$$\frac{1}{2} \sum_i m_i v_i(r_i)^2 = \frac{1}{2} \left(\frac{v_\mathrm{max}}{R} \right)^2 \cdot \sum_i m_i r_i^2 \stackrel{!}{=} E_\mathrm{kin}. \tag{43}$$

Here, v_i is the absolute value of velocity in the ith cell.
The pressure in the ejecta region is initially increased with respect to the surrounding pressure to $2 \times 10^{-6}\,\mathrm{dyn\,cm^{-2}}$, resulting in a temperature variation in the ejecta between $10^5\,\mathrm{K}$ and $10^8\,\mathrm{K}$. The kinetic explosion energy is fixed to the canonical value of $\sim 10^{51}\,\mathrm{erg}$ and for now an ejecta mass M_{ej} of $10\,\mathrm{M}_\odot$ is assumed. In the first simulation ($c = 12.5$), a grid resolution of 256×512 grid cells is chosen. Since this is found too low to actually see the power law density profile, the resolution is increased to 512×1024 grid cells for the next two simulations ($c = 9\,\mathrm{pc}$ and $c = 5\,\mathrm{pc}$). The units are kept as presented in Table 3. All simulations are then run for $\sim 4000\,\mathrm{yrs}$, which is the common age estimate for Puppis A in literature (see Table 1). The resulting density distributions are displayed in Fig. 27. Judging from the shape of the blast wave, it seems that in the model with $c = 5\,\mathrm{pc}$, the cloud is not extended enough to cause the rectangular shape that is observed. Out of the other two models, $c = 9\,\mathrm{pc}$ looks the most promising in being able to recreate the shape of Puppis A, which is why for the following simulations, $c = 9\,\mathrm{pc}$ is adapted as the semi-major axis of the elliptical torus representing the cloud.

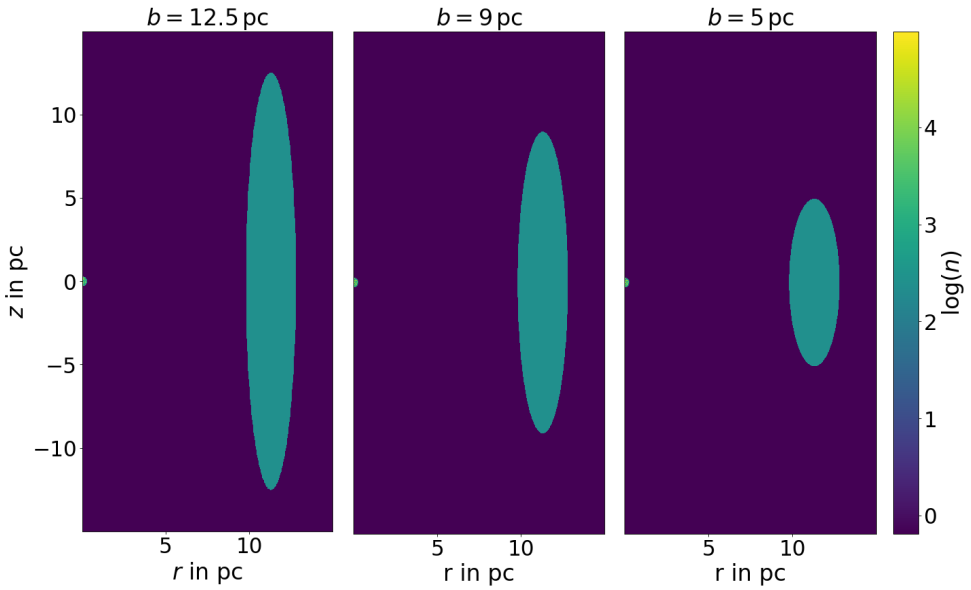

Figure 25: Initial density distributions for the 2D model setup of Puppis A in cylindrical geometry. The cloud that the remnant is interacting with is placed at a distance of 11.3 pc. The shape was chosen to be an elliptical torus with a semi-minor axis of 1.3 pc. Different semi-major axes of 12.5 pc (left), 9 pc (middle), and 5 pc (right) were tested.

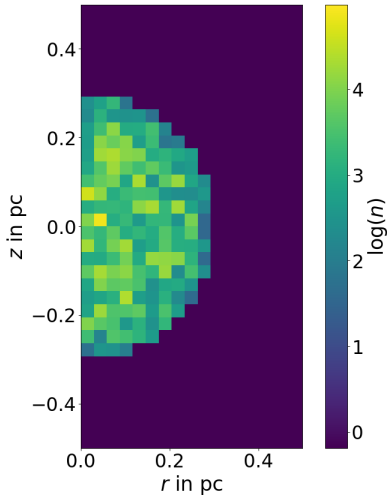

Figure 26: Initial ejecta density distribution for the 2D model setup of Puppis A in cylindrical geometry. A cell-by-cell randomisation was introduced, as well as the power law density profile for core collapse SNe presented by Chevalier (2005) to make the model more realistic. For now, the initial ejecta radius is set to 0.3 pc.

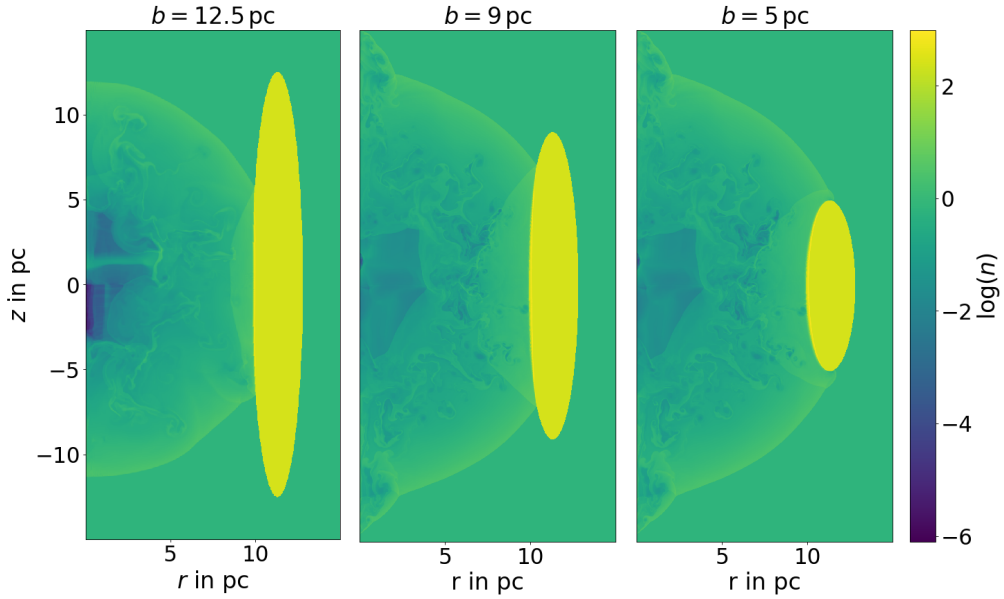

Figure 27: Density distributions for the 2D model setup of PuppisA in cylindrical geometry after $\sim$ 4000 yrs. The cloud that the remnant is interacting with is placed at a distance of 11.3 pc. The shape was chosen to be an elliptical torus with a semi-minor axis of 1.3 pc. Different semi-major axes of 12.5 pc (left), 9 pc (middle), and 5 pc (right) were tested.

5.2.2. Ejecta mass

The ejecta mass is the second parameter that is explored in two dimensions. In principle, the model setup stays the same as in the previous section, with $c = 9\,\mathrm{pc}$ and a kinetic explosion energy of $1 \times 10^{51}\,\mathrm{erg}$. However, it is decided to extend the initial radius of the ejecta to 2 pc, instead of the previous 0.3 pc to better resolve the ejecta density profile. This allows for the grid resolution to be decreased to 256×512 grid cells again, which is the resolution suitable for the 3D simulations later on. The initial pressure in the ejecta region is reduced to $\sim 40 \times 10^{-7}\,\mathrm{dyn\,cm^{-2}}$ to achieve a reasonable ejecta temperature. To take into account the proper motion of the CCO (see Sect. 3), which caused it to move away from the original explosion site, the cloud is shifted further inwards and is now centred at $r = 10\,\mathrm{pc}$. Moreover, instead of a uniform density of the surrounding ISM, a power law density profile $\rho(r) \sim r^{-2}$ dropping to $1.1\,\mathrm{g\,cm^{-3}}$ at $\sim 9\,\mathrm{pc}$, just behind the border of the cloud, is implemented. The density behind the cloud is uniform.
Three different ejecta masses are tested, namely $3\,\mathrm{M_\odot}$, $5\,\mathrm{M_\odot}$, and $10\,\mathrm{M_\odot}$. The initial density distributions are displayed in Fig. 28. The simulation is then run again for $\sim 4000\,\mathrm{yrs}$. The resulting density distributions are shown in Fig. 29. Additionally, the radial profiles for density (see Fig. 30), temperature (see Fig. 31), and velocity (see Fig. 32) are examined. Both the cloud and the ejecta were marked with a passive tracer in the initial conditions, this allows to depict the properties of each of the plasma components separately. In case of the density, the array is simply multiplied with the respective tracer array. For all other quantities that don't scale with the tracers, like temperature or velocity, a mask is created to filter for all computational cells, where the respective tracer is larger than 0.9. The data array is then multiplied by the corresponding mask.
Overall, the ejecta mass does not seem to influence the simulation results substantially. When looking at the density profiles, in all three cases the shocked ejecta is located in the innermost part of the remnant, surrounded by shocked ISM. This is promising, since most of the X-ray emission from Puppis A is believed to originate from shocked ISM (see Sect. 3.1). The forward shock has begun to propagate through the cloud with a similar velocity for all three ejecta masses. The temperatures of the shocked ejecta, ISM, and cloud are comparable in all three cases as well. Some differences can be spotted in the $10\,\mathrm{M_\odot}$ case. Due to the higher ejecta mass, the reverse shock has not yet reached the centre of the remnant, which is evident from a portion of the innermost ejecta still moving outwards, while in the remaining two simulations, the ejecta has been fully accelerating inwards.
All in all, in is concluded that the ejecta mass is not expected to introduce dramatic differences to the model, which is why as a middle ground, it is proceeded with an ejecta mass of $5\,\mathrm{M_\odot}$.

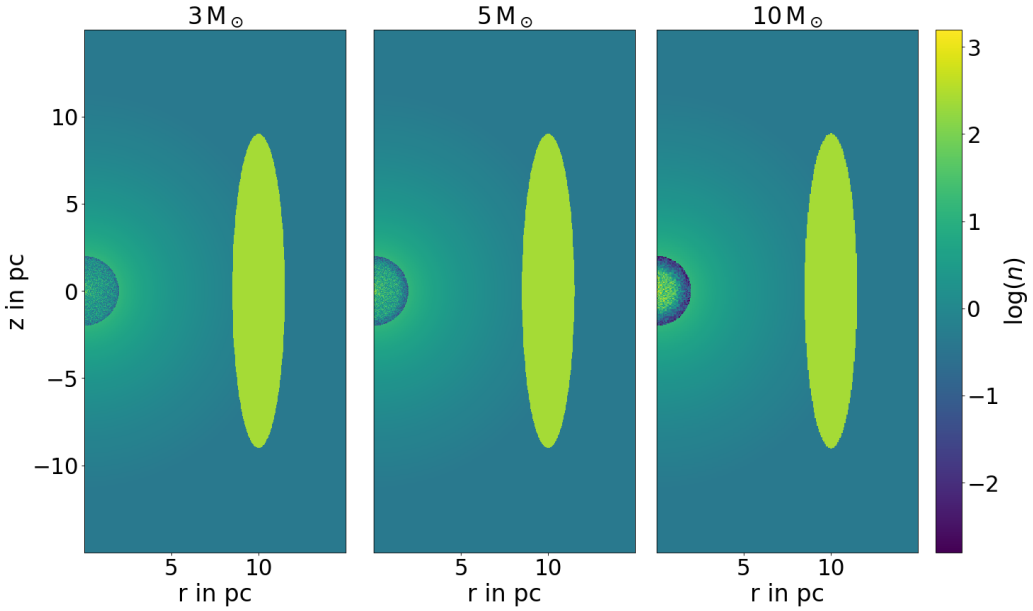

Figure 28: Initial density distributions for the 2D model setup of Puppis A in cylindrical geometry with initial ejecta masses of $3\,M_\odot$ (left), $5\,M_\odot$ (middle), and $10\,M_\odot$ (right).

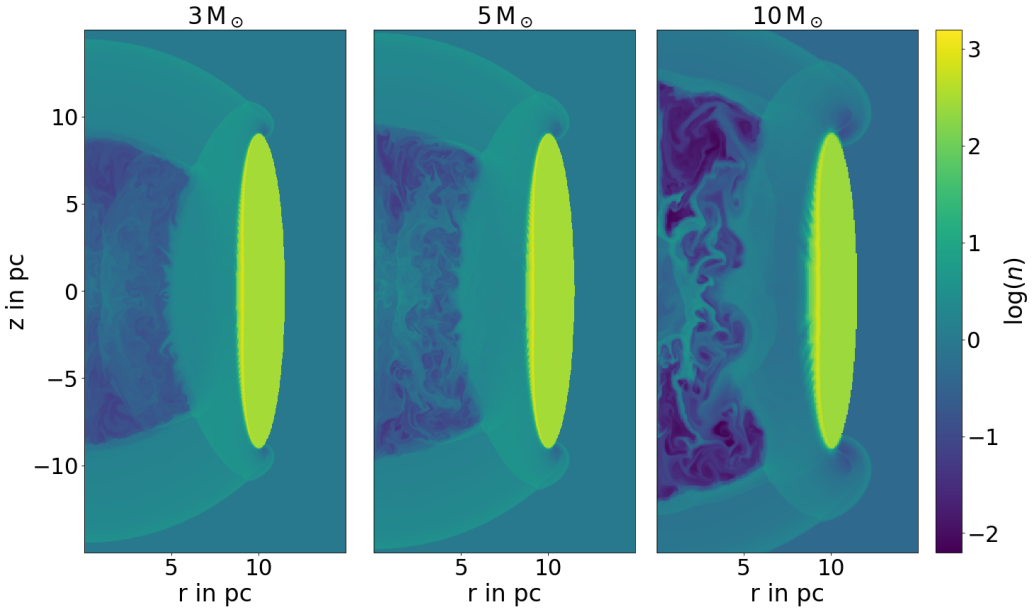

Figure 29: Density distributions for the 2D model setup of Puppis A in cylindrical geometry after $\sim$ 3900 yrs with initial ejecta masses of $3\,M_\odot$ (left), $5\,M_\odot$ (middle), and $10\,M_\odot$ (right).

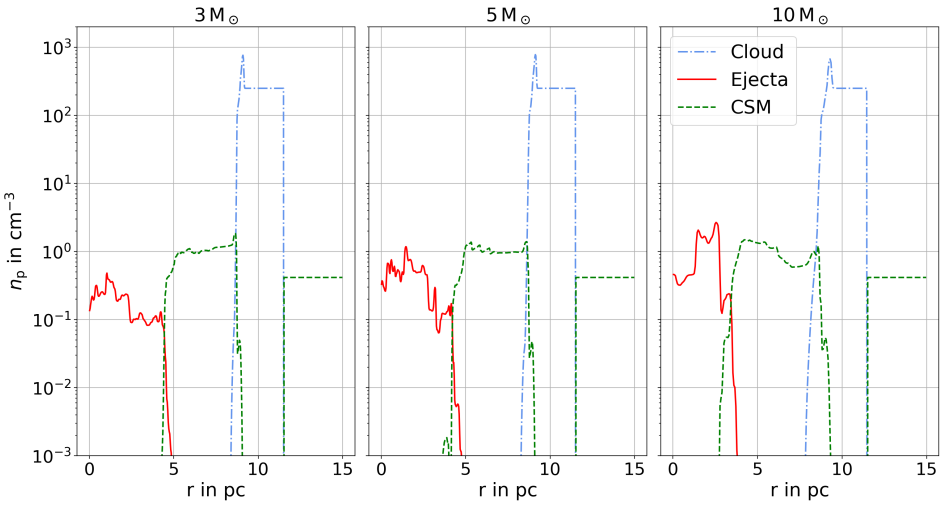

Figure 30: Radial density profiles (proton number densityn_p) for the 2D model setup of PuppisA in cylindrical geometry after $\sim 3900\,\mathrm{yrs}$. Three different initial ejecta masses of $3\,\mathrm{M}_\odot$ (left), $5\,\mathrm{M}_\odot$ (middle), and $10\,\mathrm{M}_\odot$ (right) were tested.

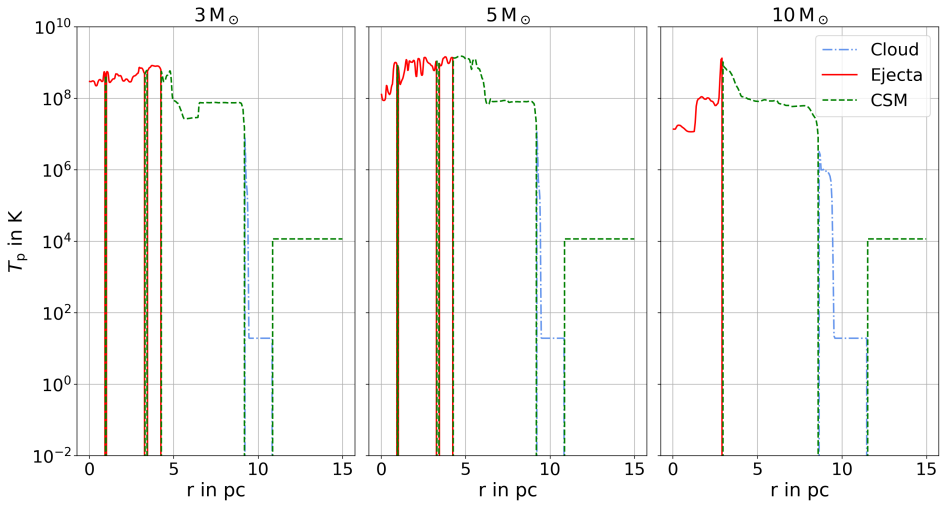

Figure 31: Radial temperature profiles (proton temperature T_p) for the 2D model setup of PuppisA in cylindrical geometry after $\sim 3900\,\mathrm{yrs}$. Three different initial ejecta masses of $3\,\mathrm{M}_\odot$ (left), $5\,\mathrm{M}_\odot$ (middle), and $10\,\mathrm{M}_\odot$ (right) were tested.

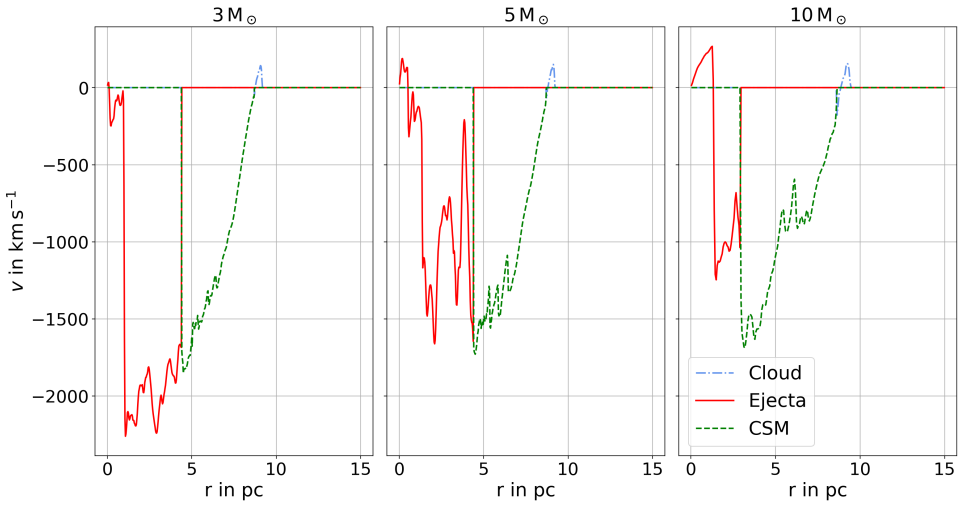

Figure 32: Radial velocity profiles for the 2D model setup of PuppisA in cylindrical geometry after $\sim 3900\,\mathrm{yrs}$. Three different initial ejecta masses of $3\,\mathrm{M}_\odot$ (left), $5\,\mathrm{M}_\odot$ (middle), and $10\,\mathrm{M}_\odot$ (right) were tested.

5.3. 3D simulations and synthetic X-ray maps

In order to take into account the asymmetry of Puppis A revealed in the observational data, the model is now extended to 3D Cartesian geometry. A grid resolution of 512×512 grid points is chosen for all three dimensional simulations and the units are kept as listed in Table 3. An ejecta mass of $5\,\mathrm{M}_\odot$ is fixed by means of Eq. 41 with the volume of a computational cell calculated as $V_i = \Delta x_i \cdot \Delta y_i \cdot \Delta z_i$ in 3D Cartesian geometry. The randomisation of the ejecta region and the power law profile by Chevalier (2005) as described in Sect. 5.2.2 are also maintained, as well as the power law density profile in the ISM to imitate a possible stellar wind of the progenitor. However, the cell-by cell randomisation of the density is introduced also to the ISM by multiplying the original power law profile with random numbers in the interval $2^{[-1,1]}$. Moreover, the gas composition is changed to solar abundances by means of setting the mean molecular weight per electron to $\mu = 1.2$. The main visible changes to the model were made with respect to the geometry of the cloud. In the course of this work, three different geometries were tested, which will hereafter be referred to as model 1 (Sect. 5.3.1), model 2 (Sect. 5.3.2), and model 3 (Sect. 5.3.3). For each model, parameters like the explosion energy or the ISM density are varied and the results are then compared to the observations. All of the changes introduced to the geometry of the model setup are based on the results obtained from the previous version and are supposed to improve the resemblance of the simulated data to the observations.

5.3.1. Model 1

In a first attempt to adjust the density distribution in the cloud, a Gaussian profile was implemented on the torus:

$$\rho(\theta) \sim \exp\left(-\frac{(\theta-\theta_0)^2}{2\sigma^2}\right). \tag{44}$$

Here, $\theta = \arctan\left(\frac{x_1}{x_3}\right)$ describes the angle around the torus, θ_0 determines the position and σ the width of the maximum density. For the first simulation run, $\theta_0 = 0$ and $\sigma = \frac{\pi}{8}$ are chosen. This means the density reaches its maximum on one side and gradually drops to around $1 \times 10^{-24}\,\mathrm{g\,cm^{-3}}$ on the opposite side, which is nicely shown in Fig. 34. The ISM density is kept as a power law profile $\rho(r) \sim r^{-2}$, which drops to $1.1 \times 10^{-24}\,\mathrm{cm^{-3}}$ at $\sim 9\,\mathrm{pc}$ just behind the border of the cloud and is constant behind the cloud. As already mentioned, the profile is superimposed with a cell-by-cell randomisation in the interval $2^{[-1,1]}$.

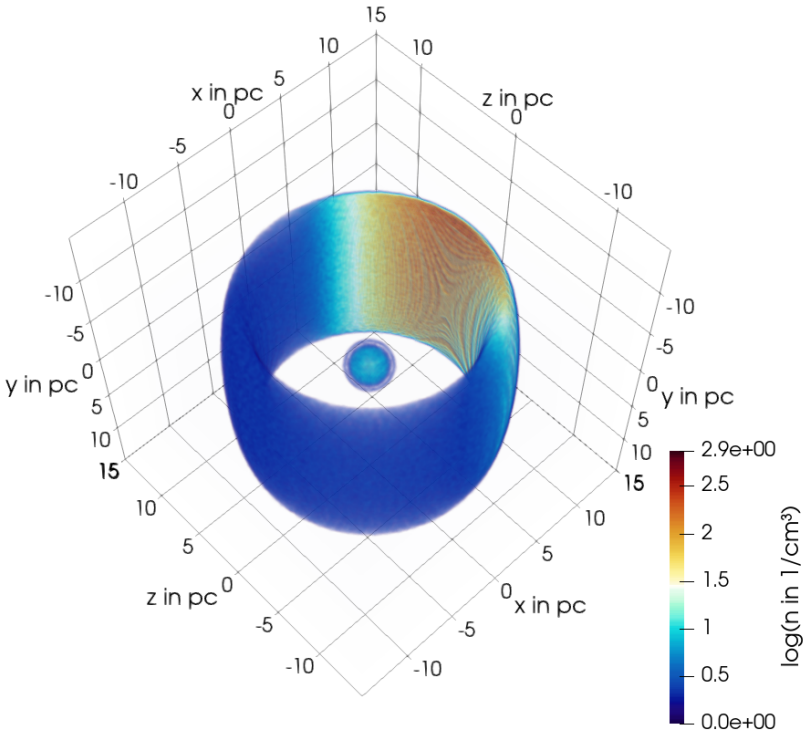

Figure 33: Three dimensional initial density distribution in the ejecta and cloud region for the first version of the model setup (model 1).

The density distribution after a simulation time of 4000 yr is shown in Fig. 35. Evidently, the forward shock from the SN explosion has propagated far enough to hit the cloud.

A reverse shock has also formed, accelerating the shocked plasma inwards. For further details, the initial and final radial profiles for density, pressure and velocity can be found in Appendix B.1.
To be able to compare the HD model directly to the X-ray observations, the X-ray emission is synthesised to generate X-ray maps from the simulation results following the method described in Sect. 2.3 of Orlando et al. (2015). First of all, the plasma temperature is calculated (see PLUTO Team (2021)) according to

$$T = \frac{p}{2k_{\mathrm{B}}n} = \frac{p\mu m_{\mathrm{p}}}{2k_{\mathrm{B}}\rho} \tag{45}$$

with the mean molecular weight per electron $\mu = 1.2$. The electron temperature T_{e} is then computed based on the assumption that the electrons thermalise via Coulomb collisions with ions (see Orlando et al. (2015) for a detailed description). Additionally, the ionisation age $\tau = n_{\mathrm{e}}t$ in each computational cell is determined, with the electron number density $n_{\mathrm{e}} = \frac{\rho}{\mu m_{\mathrm{p}}} = \frac{\rho}{1.2m_{\mathrm{p}}}$ and the time t since the cell has been shocked.
The resulting contribution to the unabsorbed X-ray flux in each cell is then determined in Xspec[2], a software package for X-ray spectral fitting, according to the plasma emission model `vnei`, which is a non-equilibrium ionisation (NEI) plasma model with variable element abundances taking both the plasma temperature and the ionisation time scale as model parameters (see Borkowski et al. (2001), Hamilton et al. (1983), Borkowski et al. (1994), and Liedahl et al. (1995) for reference). The element abundances are fixed to solar values. The data cube is then rotated around the x, y, and z axis by the respective angles $\alpha_{\mathrm{x}} = 20°$, $\alpha_{\mathrm{y}} = -40°$, and $\alpha_{\mathrm{z}} = 150°$ to approximately match the orientation of Puppis A. Throughout, this work, different rotation angles will be tested. Finally, the flux contributions are weighted with the emission measure and summed up along the line of sight (z axis) to create a two dimensional projected X-ray map as would be observed in the sky.
The resulting X-ray map for model 1 is shown in the left panel of Fig. 36. Here, it is evident that the X-ray emission is dominated largely by the shocked cloud and the emission from the shocked ejecta and ISM is barely visible. This is not what is expected from observations. To estimate what the morphology of the ISM and ejecta emission would look like, the right panel of Fig. 38 shows the X-ray map with the emission from the cloud largely neglected, which is possible by only summing up the flux contributions from those cells, where the cloud tracer is lower than 0.1. Here, it is evident that the emission takes the expected rectangular shape. Additionally, in the right panel of Fig. 36 a bright feature on the lower right of the remnant has developed self-consistently. A similar feature is seen in the X-ray observations of Puppis A, known as the bright eastern knot (BEK, see Sect. 3.1), which means the model is showing promising results.
In order to improve the model, the emission from the cloud is to be reduced. This is implemented by enabling tabulated radiative cooling to consider also radiative losses and cool down the shocked cloud below a temperature where X-rays are emitted. The temperature profiles with and without radiative losses between 6 pc and 10 pc are displayed in Fig. 58

[2] https://heasarc.gsfc.nasa.gov/xanadu/xspec/

and Fig. 62. The full temperature profiles can be found in Appendix B.1. Evidently, the temperature of the shocked cloud between a radial distance of $\sim 8.8\,\mathrm{pc}$ and $\sim 9.1\,\mathrm{pc}$ has gone down significantly. However, when again synthesising the X-ray map (see Fig. 38), the emission is still dominated by the shocked cloud material. Curiously, the emission is bright in two vertical strips, which are coincident with where the cloud density transitions from maximum density to the lower density at the foot of the Gaussian. Due to the Gaussian profile, the density transitions smoothly, which means in the two regions left and right of the maximum the density is not as high as to slow down the shock from the explosion in the same manner as the densest part of the cloud does, but still high enough to exceed the emission measure of the lower density cloud material on the opposite side of the maximum density. Additionally, judging from the X-ray image in Fig. 8, the remnant seems to be expanding more or less freely in the south-west. In the simulations, this is not the case as the blast wave is confined on all sides within the toroidal cloud.

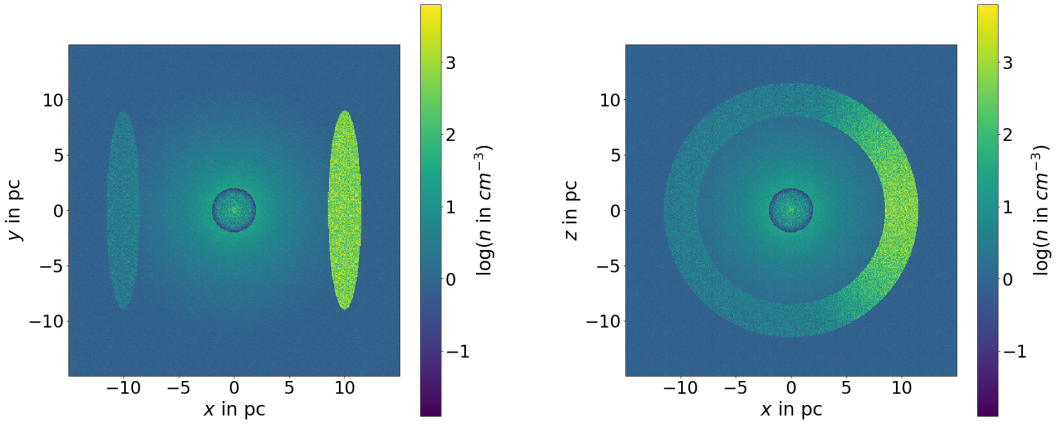

Figure 34: Initial 2D cuts of the density distributions for the 3D model setup of Puppis A in Cartesian geometry. The left panel shows the x-y-plane at z=0 and the right panel shows the x-z-plane at y=0. The cloud that the remnant is interacting with is placed at a distance of 10 pc. The shape was chosen to be an elliptical torus, superimposed with a Gaussian density profile.

Another way to quantitatively compare the plasma conditions in the simulations to the ones derived from observations is to create a 2D histogram showing the distribution of emission measure EM with respect to the ionisation timescale τ and the electron temperature T_e calculated from each computational cell in the simulated data, as was done for example by Greco et al. (2022). The values for EM are sorted into logarithmic bins in both T_e and τ and subsequently normalised by the bin size. The resulting distribution derived from model 1 with radiative losses considered is displayed in Fig. 39. A similar histogram created from the eROSITA X-ray observations of Puppis A presented by Mayer et al. (2022) is displayed in the top panel of Fig. 39. Evidently, the electron temperature generally is a lot higher in the simulations (maximum well above 1 keV)

compared to the observations (maximum between 0.5-0.6 keV) and the model results show a much broader range in τ. All in all, it is clear that some modifications to the model geometry are necessary, since the agreement between the current model results and the observations is not yet satisfactory.

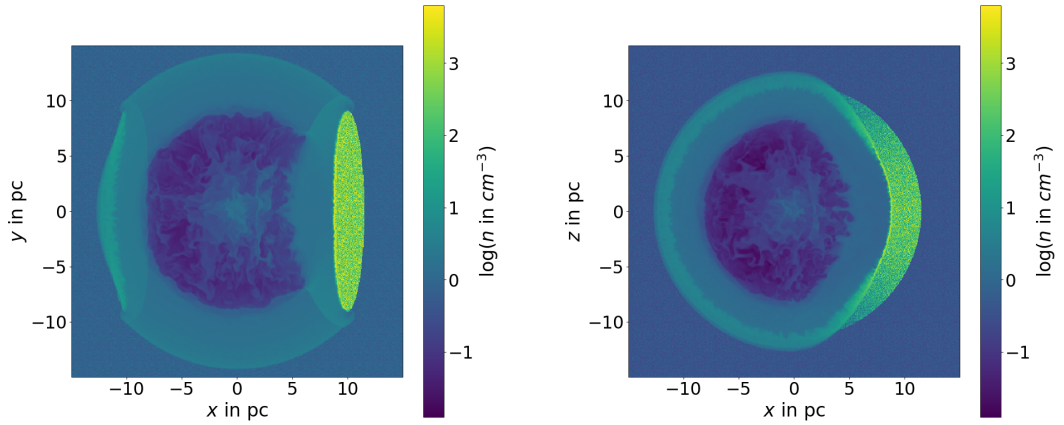

Figure 35: Two dimensional cuts of the density distributions for the 3D model setup of Puppis A in Cartesian geometry after a simulation time of $\sim$ 4000 yr. The left panel again shows the x-y-plane at z=0 and the right panel shows the x-z-plane at y=0.

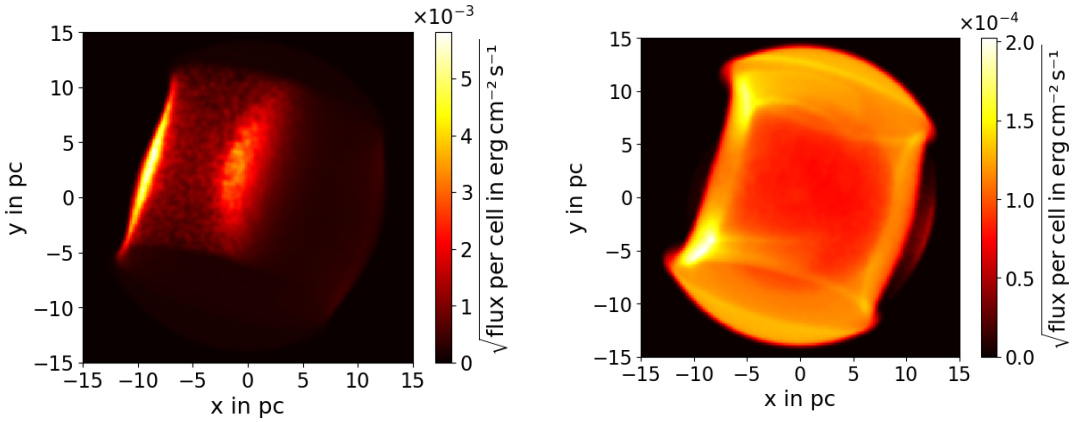

Figure 36: Synthetic X-ray map in the 0.3-10 keV band for model 1 showing the resulting emission from all plasma components (left panel) and the emission predominantly from the ejecta and shocked ISM with the cloud emission neglected. The intensity scale is square root to be comparable to Fig. 8.

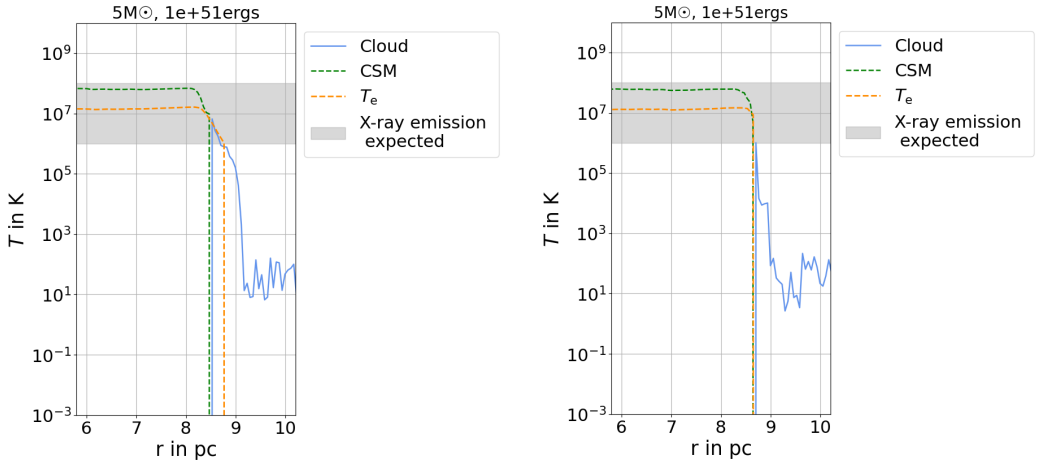

Figure 37: Radial temperature profiles in the interaction region of the forward shock with the densest part of the cloud after a simulation time of $\sim 4000\,\mathrm{yr}$. The left panel shows the simulation run without radiative losses and in the right panel radiative losses were included. The shaded areas mark the temperature range in which thermal X-ray emission is expected. Evidently, in the right panel the temperature of the shocked cloud is significantly lower and even drops below the range in which X-rays are emitted almost completely.

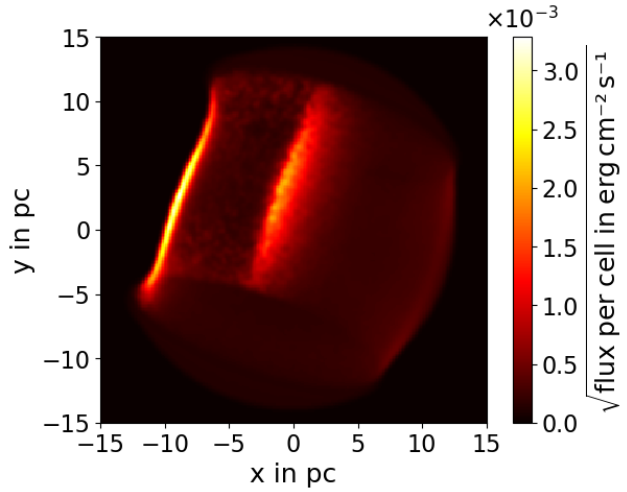

Figure 38: Synthetic X-ray map in the 0.3-10 keV band for model 1 with radiative losses considered in the simulation run. The intensity scale is square root to be comparable to Fig. 8.

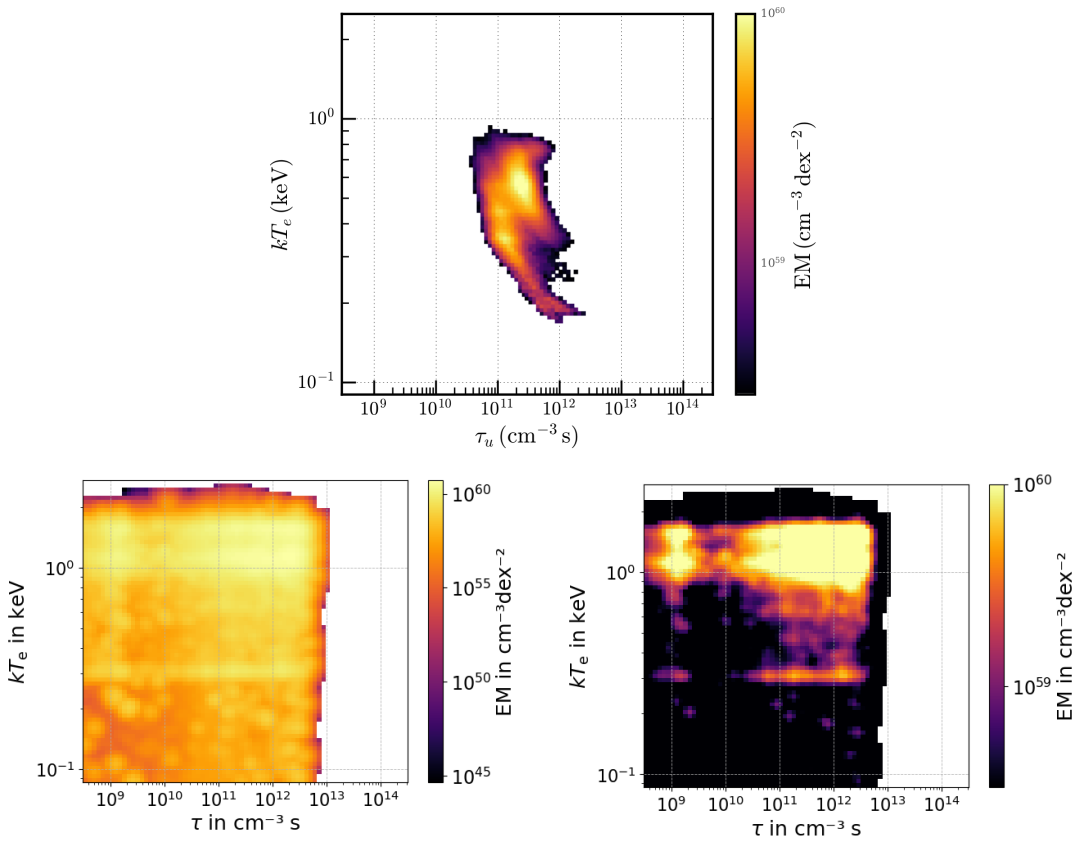

Figure 39: Histograms of the logarithmic distribution of emission measure (EM) with respect to the ionisation timescale and electron temperature. The top panel shows the EM distributions derived from spectral fitting of the eROSITA X-ray data presented by (Mayer et al., 2022). The bottom panel shows the same distribution for model 1 with radiative losses included. In left figure, the colour bar is scaled to the data range. On the right, the colour bar matches the top panel for comparability. Credits for top panel: Martin Mayer.

5.3.2. Model 2

In the second version of the model setup for Puppis A, the geometry of the cloud is changed from a full torus to a partial torus with a sharp density cut with respect to the ambient density instead of the previous smooth transition by means of the Gaussian profile. An angular extent of $\theta = \frac{\pi}{4}$ is chosen. As a consequence, the expansion of the blast wave is no longer confined in the south-western part of the remnant, but only in the north-east. Additionally, the two maxima observed in the X-ray emission should also vanish, since there is no transitional density any more. The rest of the model parameters for now stay the same as in model 1. The initial density distributions are shown in Figs. 40 and 41.

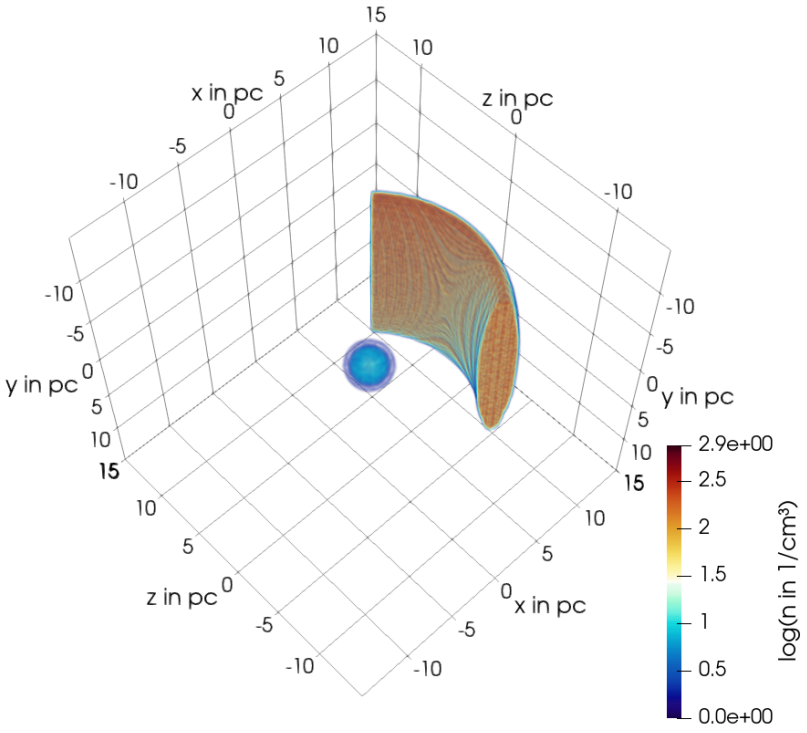

Figure 40: Three dimensional initial density distribution in the ejecta and cloud region for the second version of the model setup (Model 2).

The simulation is then again run for around 4000 yr. The resulting density distributions are displayed in Fig. 42 and in Appendix B.2, the initial and final profiles for density, temperature, velocity, and pressure are shown. As predicted, the blast wave is now confined by the cloud and freely expanding on the other side. Again, a reverse shock has formed located at around $r \approx 5\,\mathrm{pc}$, where the shock-cloud interaction took place, and is accelerating the material inwards.
To compare the X-ray emission, an X-ray map in the 0.1-10 keV band is generated in the same way as described in Sect. 5.3.1, this time with rotation angles $\alpha_\mathrm{x} = 20°$, $\alpha_\mathrm{y} = -20°$, and $\alpha_\mathrm{z} = 150°$ (see Fig. 43). Compared to model 1, the emission from the ISM with respect to the emission from the shocked cloud has risen, and as expected, the two bright, vertical strips of emission have disappeared. Additionally, the bright feature in the south-western part of the remnant is sill visible, which is very promising. However, even though the sharp edge in emission on the north-eastern side of the remnant caused by the cloud is still visible, there is now also emission present beyond the border, likely the projection of the shocked ISM and ejecta from the angular region behind the cloud. As this is not consistent with the observations, it will be necessary to adjust the angular extent of the cloud. Figure 44 shows the distribution of emission measure with respect to ionisation time scale τ and electron temperature T_e. The emission measure is reduced

compared to the previous version of the model, which is expected, since $EM \sim n_e^2$ and a large portion of the dense cloud material has been removed. Compared to the observations, the EM is now almost on the same order of magnitude. In contrast, the electron temperature of the plasma is still a lot higher and peaks at over 1 keV. As a reminder, the peak of the electron temperature derived from observations lies at around 0.6 keV. The spread in ionisation timescale is also still broader, compared to what is observed. Overall, just like for the previous version, further modifications of the model geometry and parameters are required.

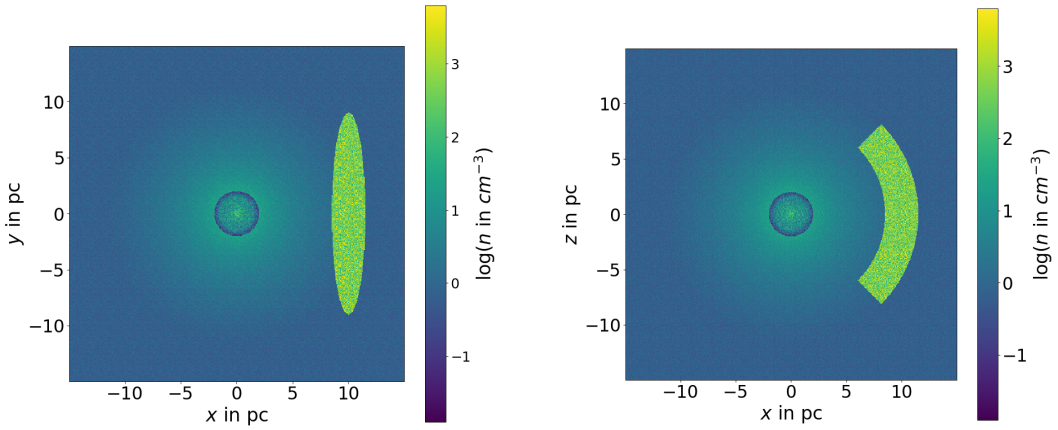

Figure 41: Two dimensional cuts of initial the density distributions for the 3D model setup of Puppis A in Cartesian geometry. The left panel shows the x-y-plane at z=0 and the right panel shows the x-z-plane at y=0. The cloud that the remnant is interacting with is placed at a distance of 10 pc. The shape was chosen to be a partial elliptical torus covering an angle of $\frac{\pi}{4}$.

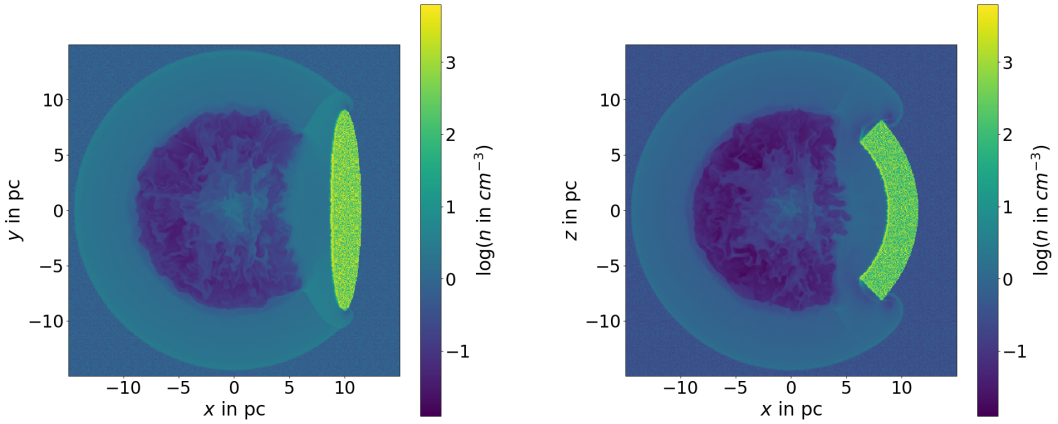

Figure 42: Two dimensional cuts of the density distributions for the 3D model setup of Puppis A in Cartesian geometry after a simulation time of $\sim 4000\,\mathrm{yr}$. The left panel again shows the x-y-plane at z=0 and the right panel shows the x-z-plane at y=0.

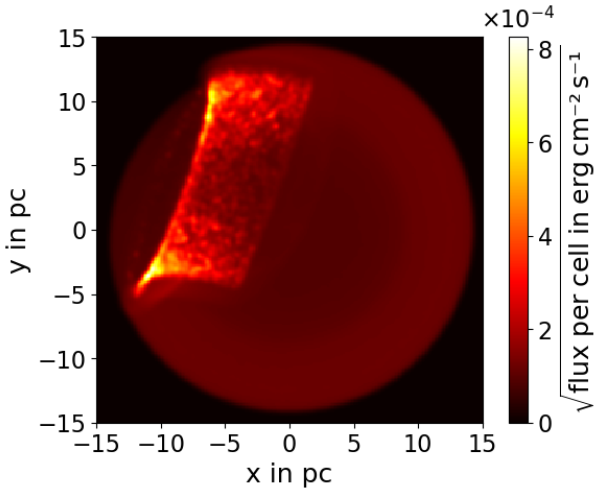

Figure 43: Synthetic X-ray map in the 0.3-10 keV band for model 2 with radiative losses considered in the simulation run. The intensity scale is square root to be comparable to Fig. 8.

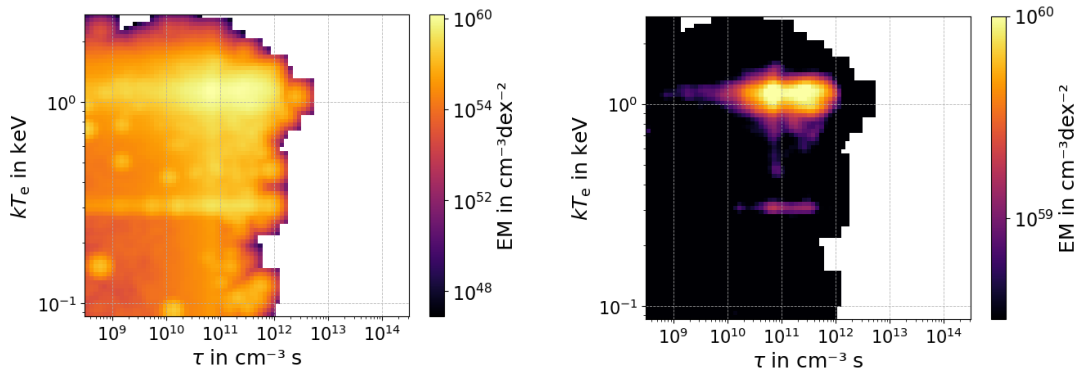

Figure 44: Histogram of the logarithmic distribution of emission measure with respect to the ionisation time and electron temperature for model 2. In the left panel, the colour bar is scaled to the data range and on the right the colour bar matches the top panel of Fig. 39 for comparability.

5.3.3. Model 3

In order to increase the resemblance of the synthesised X-ray emission to the observations, a more sophisticated version of clumping is introduced in the cloud, similar to for example Ustamujic et al. (2021). While the geometry remains the same as in the previous model setup, the size of the clumps was increased to replace the cell-by-cell density variations implemented before. In total, 20000 clumps are randomly placed within the cloud region. The clump radius is fixed to 5 cells, which corresponds to a clump diameter of $\sim 0.04\,\mathrm{pc}$. The density again is randomised within the interval of $\rho_0 \cdot 10^{[-j,j]}$. The value of ρ_0 is set to $\sim 200\,\mathrm{cm}^{-3}$ based on (Aruga et al., 2022). The angular extent of the cloud is increased to $\theta = \frac{2}{3}\pi$ based on the results discussed in the previous section. In the ISM, the power law density profile with index 2 is kept. The initial density distribution is nicely shown in Figs. 45 and 46. In the following five simulation runs (referred to as model 3.1 to model 3.4), the ISM density, the explosion energy, and the simulation time are varied in order to explore, which parameters deliver the best results. An overview of the tested model parameters is shown in Table 5. The ISM density in models 3.3, 3.4, and 3.5 are normalised to a specific mass M_{ISM} of plasma within a radius of 10.6 pc based on the total mass of emitting plasma derived by Mayer et al. (2022) (see Table 4). Figure 47, as an example, shows the final density distribution of model 3.1 to illustrate the shock-cloud interaction with the newly introduced clumping in the cloud.

Model version	Model parameters
Model 3.1	$M_{\mathrm{ejecta}} = 5\,\mathrm{M}_{\odot}$, $E_{\mathrm{kin}} = 1 \times 10^{51}\,\mathrm{erg}$, $\rho_{\mathrm{Cloud}} \in \rho_0 \cdot 10^{[-1,1]}$, $t_{\mathrm{sim}} \approx 2300\,\mathrm{yr}$, $M_{\mathrm{ISM}} = 50\,\mathrm{M}_{\odot}$
Model 3.2	$M_{\mathrm{ejecta}} = 5\,\mathrm{M}_{\odot}$, $E_{\mathrm{kin}} = 5 \times 10^{50}\,\mathrm{erg}$, $\rho_{\mathrm{Cloud}} \in \rho_0 \cdot 10^{[-1,1]}$, $t_{\mathrm{sim}} \approx 3100\,\mathrm{yr}$, $M_{\mathrm{ISM}} = 50\,\mathrm{M}_{\odot}$
Model 3.3	$M_{\mathrm{ejecta}} = 5\,\mathrm{M}_{\odot}$, $E_{\mathrm{kin}} = 5 \times 10^{50}\,\mathrm{erg}$, $\rho_{\mathrm{Cloud}} \in \rho_0 \cdot 10^{[-1,1]}$, $t_{\mathrm{sim}} \approx 4000\,\mathrm{yr}$, $M_{\mathrm{ISM}} = 180\,\mathrm{M}_{\odot}$
Model 3.4	$M_{\mathrm{ejecta}} = 5\,\mathrm{M}_{\odot}$, $E_{\mathrm{kin}} = 5 \times 10^{50}\,\mathrm{erg}$, $\rho_{\mathrm{Cloud}} \in \rho_0 \cdot 10^{[-2,2]}$, $t_{\mathrm{sim}} \approx 3100\,\mathrm{yr}$, $M_{\mathrm{ISM}} = 85\,\mathrm{M}_{\odot}$

Table 5: Overview of the tested model parameters for models 3.1 to 3.4

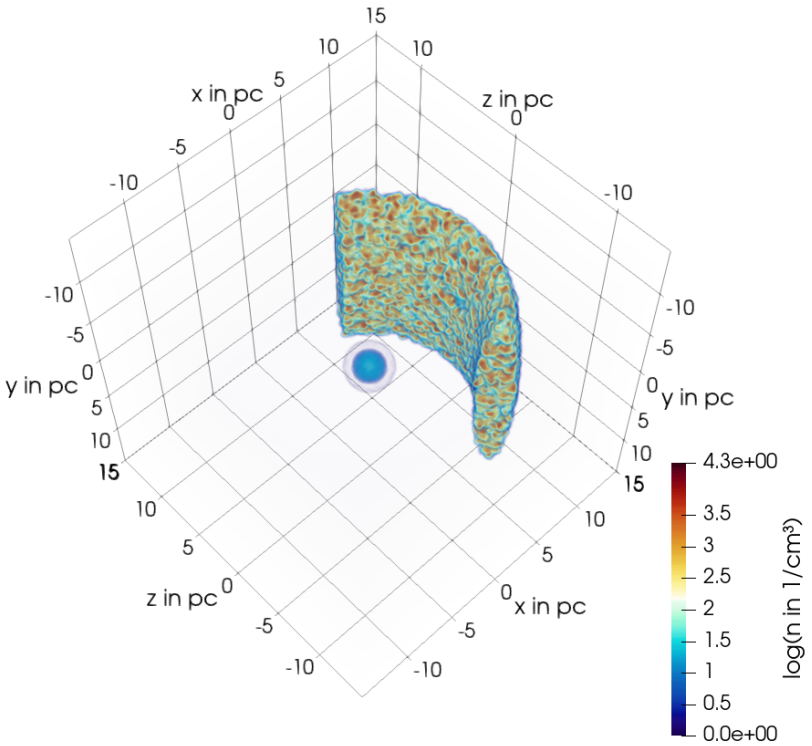

Figure 45: Three dimensional initial density distribution in the ejecta and cloud region for the third version of the model setup (Model 3).

The X-ray maps and histograms to showcase the resulting X-ray morphology and EM, T_{e} and τ distributions are then generated in the same manner as described in Sect. 5.3.1. The X-ray maps for models 3.1 - 3.4 are displayed in Fig. 48. Although the larger clumping better resembles the filamentary structures found in X-ray observations of

Puppis A, evidently, for all four simulation runs, the emission is heavily dominated by the shocked cloud. Especially in model 3.1, were the ISM density is the lowest compared to the other model setups, almost no emission from the ISM is visible in the X-ray map. The most emission from the ISM can be detected in model 3.3, where the initial ISM density is normalised to 180 $M_\odot$ within a radius of 10.6 pc. Reducing the kinetic explosion energy to 5×10^{50} erg also does not seem to have a noticeable effect on reducing the cloud emission. Figure 49 shows the distribution of emission measure with respect to τ and T_e. All three diagrams show a similar distribution in emission measure and a similar spread in electron temperature and ionisation timescale. The electron temperature peaks at around 1 keV for all the models, which compared to the observations is still to high. Increasing the density variations in to cloud to lie within $\rho_0 \cdot 10^{[-2,2]}$, as was done for model 3.4, has managed to bring the temperature down, but only by a very small amount. However, the EM is on the same order of magnitude or just slightly higher as derived from the observations for all four models. The spread in τ is still broader, compared to the observations. Thus far, even though some of the model results are quite promising, none of the models seems to be able to convincingly reproduce the plasma conditions in Puppis A.

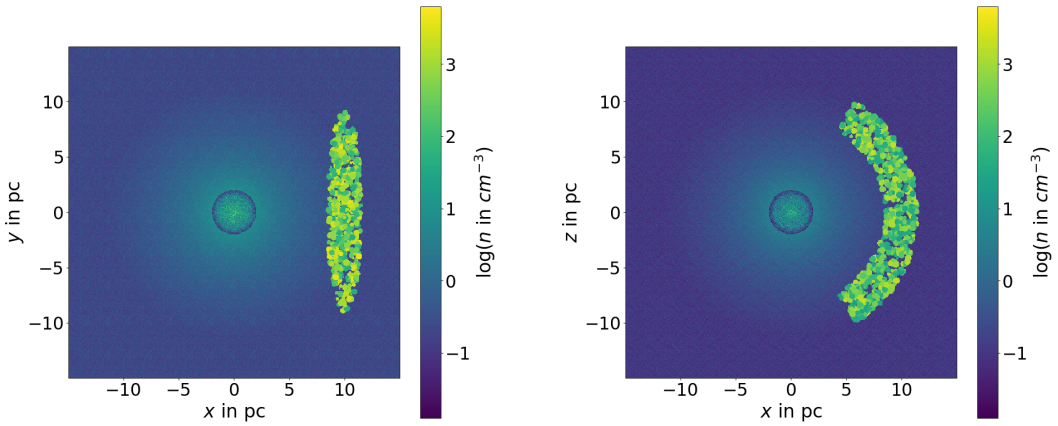

Figure 46: Two dimensional cuts of initial the density distributions for the 3D model setup of Puppis A in Cartesian geometry. The left panel shows the x-y-plane at z=0 and the right panel shows the x-z-plane at y=0. The cloud that the remnant is interacting with is placed at a distance of 10 pc. The shape was chosen to be a partial elliptical torus covering an angle of $\frac{\pi}{4}$. Additionally, clumps with a radius of 5 cells each were implemented.

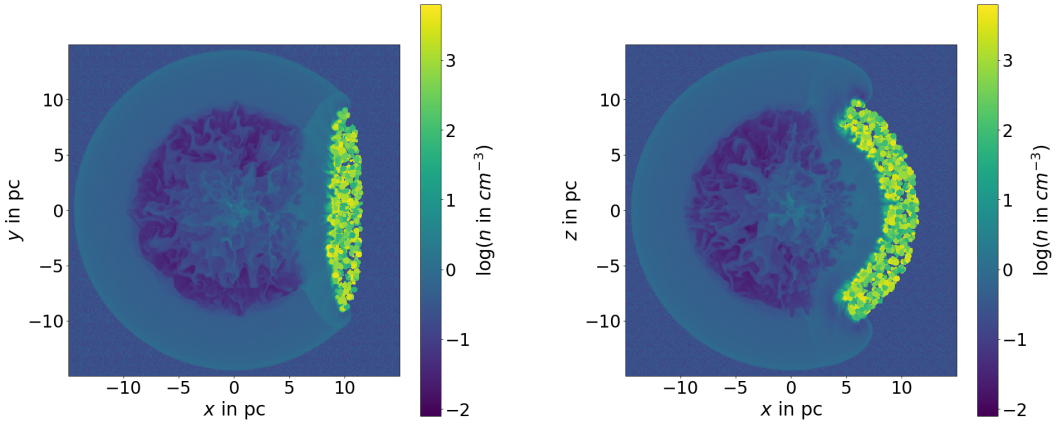

Figure 47: Two dimensional cuts of the density distributions for the 3D model setup of Puppis A in Cartesian geometry after a simulation time of $\sim 4000\,\mathrm{yr}$ (Model 3.1). The left panel again shows the x-y-plane at z=0 and the right panel shows the x-z-plane at y=0.

The main goal to improve the model is now to somehow reduce the temperature to match the observations, which is also expected to have an effect on the X-ray emission resulting from the model. Since neither reducing the kinetic energy nor increasing the density in the cloud had a significant effect on bringing the temperature down, this leaves the initial pressure in the ejecta region as one of the parameters that has not been explored yet. For all previous simulation runs, the initial pressure in the ejecta region was fixed to $\sim 40 \times 10^{-7}\,\mathrm{dyn\,cm^{-2}}$. To estimate, if this is expected to have a noticeable effect on the dynamics of the evolution of the remnant, the internal energy E_{th} in the ejecta region is estimated from the volume V and the pressure P. The internal energy density can be expressed as $\rho e = \frac{P}{\gamma - 1}$ (see Sect. 2.3 for details). With $\gamma = \frac{5}{3}$, this results in $\rho e = \frac{3}{2}P$. Integrated over the entire volume of the ejecta region, the internal energy can be estimated according to $E_{\mathrm{th}} = \frac{3}{2}PV$. For the pressure specified above, this results in $E_{\mathrm{th}} \approx 9 \times 10^{51}\,\mathrm{erg}$. Compared to the kinetic explosion energy, which for all previous models lies between $0.5 - 1 \times 10^{51}\,\mathrm{erg}$, this is clearly too high and probably had a significant effect on the evolution of the remnant. As a consequence, one final model version is tested (model 3.5), in which the initial pressure in the ejecta region is reduced by two orders of magnitude to around $\sim 0.8 \times 10^{-7}\,\mathrm{dyn\,cm^{-2}}$. This should correspond to an energy of $E_{\mathrm{th}} \approx 1 \times 10^{50}\,\mathrm{erg}$. In turn, the kinetic explosion energy is increased to $E_{\mathrm{kin}} = 1.5 \times 10^{51}\,\mathrm{erg}$. This means in this scenario, the thermal energy makes up only about 7% of the total energy and the evolution should be governed by the kinetic contribution only. All other initial conditions for model 3.5 are kept just like in the previous version (model 3.4). However, due to the reduced thermal energy, the blast wave is not able to reach the cloud within 4000 yr. The simulation is therefore run for 5000 yr. The initial and final radial profiles of density, velocity, pressure and temperature are displayed in Appendix B.3. The resulting X-ray map is shown in Fig. 50 and the distributions of EM, τ, and T_{e} are displayed in Fig. 51. From the X-ray map, it

is evident that now the model is able to reproduce the X-ray morphology of Puppis A much better, especially in the north-eastern part where the blast wave is interacting with the cloud. In the south-western part of the remnant, the ISM emission has risen significantly with respect to the cloud emission. However, since in this region, no further inhomogeneities have been placed into the ISM, the filaments from the real observations are not present and the emission is rather uniform. The distributions of EM, τ, and T_e are displayed in Fig. 51. Compared to the observations, the emission measure is lower by around two orders of magnitude. Even though the model is still not able to reproduce the exact plasma conditions as from the observations, the peak of the electron temperature has decreased significantly to around 0.7 keV, which is comparable with the temperature peak derived from the observations.

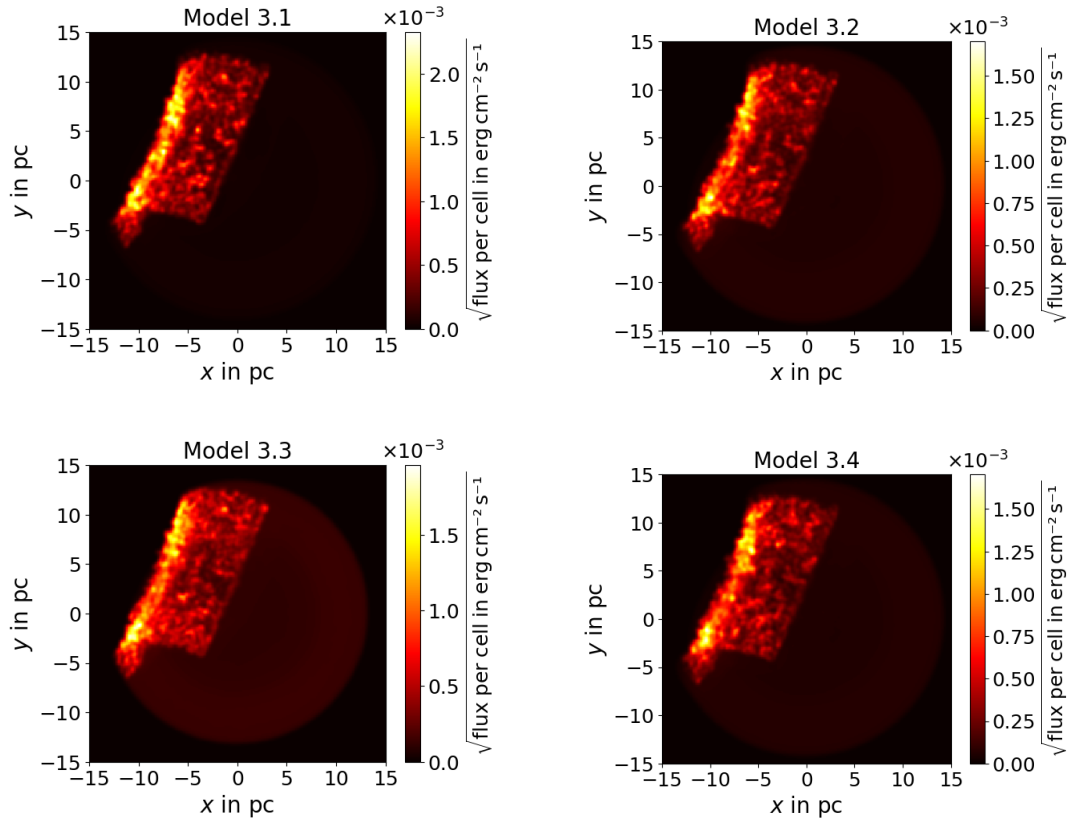

Figure 48: Synthetic X-ray maps in the 0.3-10 keV band for model versions 3.1 (top left), 3.2 (top right), 3.3 (bottom left), and 3.4 (bottom right). The respective model parameters are listed in Table 5. The intensity scale is square root to be comparable to Fig. 8.

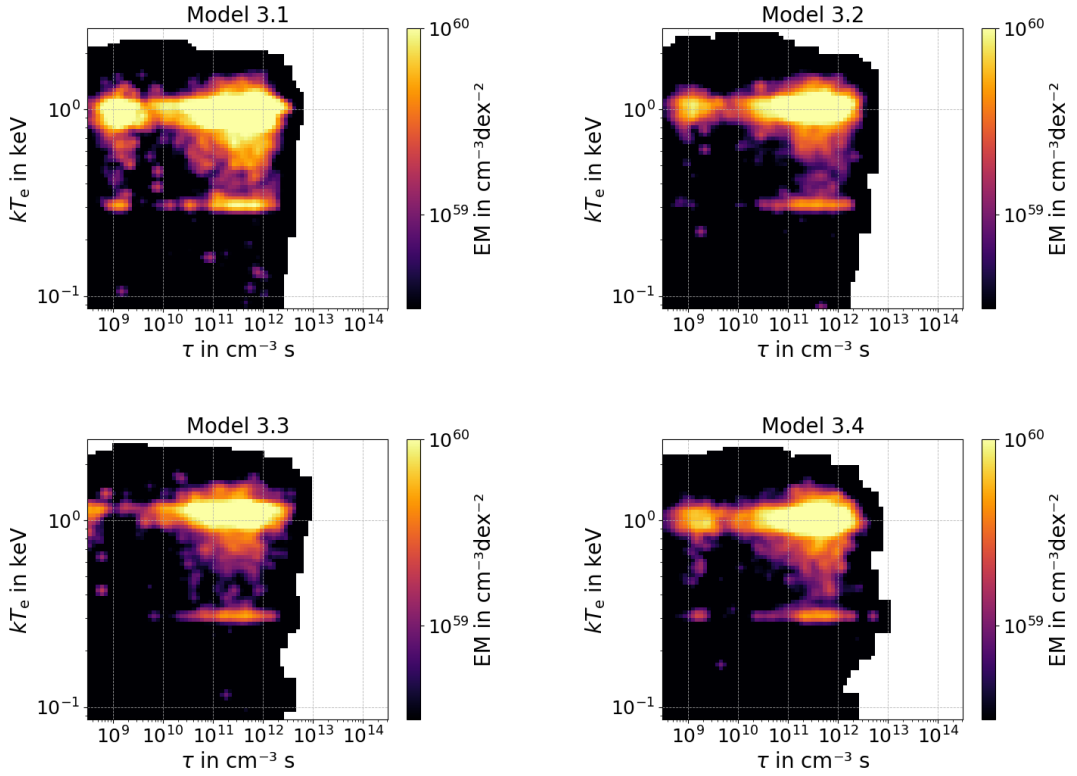

Figure 49: Histograms of the logarithmic distribution of emission measure EM with respect to the ionisation timescale τ and electron temperature kT_e for model model versions 3.1 (top left), 3.2 (top right), 3.3 (bottom left), and 3.4 (bottom right). The corresponding model parameters are listed in Table 5. The colour bar is scaled to match the top panel of Fig. 39 for comparability. The same histograms scaled to the data range can be found in Appendix **??**.

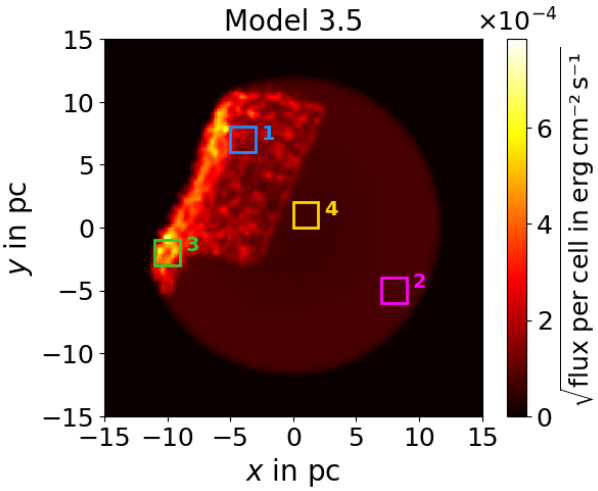

Figure 50: Synthetic X-ray map in the 0.3-10 keV band for model 3.5. The intensity scale is square root to be comparable to Fig. 8. The squared region 1-4 are used to extract the spectra discussed in Sect. 5.4.

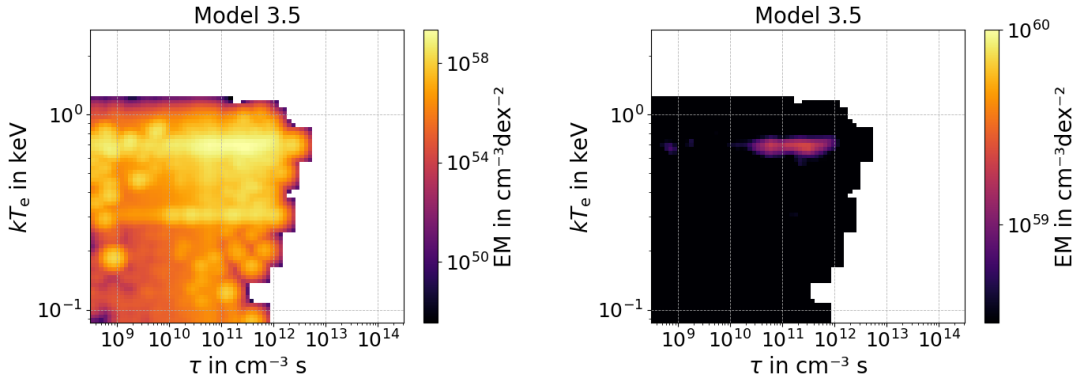

Figure 51: Histogram of the logarithmic distribution of emission measure with respect to the ionisation time and electron temperature for model version 3.5. In the left panel, the colour bar is scaled to the data range and on the right the colour bar matches the top panel of Fig. 39 for comparability.

5.4. Synthetic X-ray spectra

From the simulated data, it is possible to synthesise not only the X-ray maps, but also the X-ray spectra. This provides another effective way to compare the simulations to the observations and test the validity of the model setup. Again, the approach presented by Orlando et al. (2015) is followed. For each computational cell, the ionisation timescale $\tau = n_e t$, with the time t since the cell has been shocked, and the electron temperature T_e are determined. Similar to the X-ray fluxes, simulated spectra for a variety of values

for T_e and τ are generated with Xspec, again using a non-equilibrium ionisation (NEI) plasma emission model with variable element abundances (`vnei`). Foreground absorption is taken into account following the Tübingen-Boulder (`tbabs`) model by Wilms et al. (2000). The absorbing column density is fixed to $N_\mathrm{H} = 3 \times 10^{21}\,\mathrm{cm}^{-2}$ and the median of the element abundances reported by Mayer et al. (2022) is assumed (O, Ne, Mg, Si, S, and Fe). All the other abundances are set to solar values, except for the Nickel abundance, which is assumed to be equal to the iron abundance. The corresponding normalisation factor is $\frac{10^{-14}}{4\pi D^2} \cdot EM$, where D is the distance to the source and $EM = n_\mathrm{e}^2 V$ is the emission measure of the emitting volume V. Here, a distance of 1.3 kpc (Mayer et al., 2020) is adopted. To make the spectra comparable to the eROSITA spectra shown in Mayer et al. (2022), the corresponding auxiliary response file (ARF) of a representative spectral region defined by Mayer et al. (2022) and the corresponding response matrix file (RMF) file are used to create the spectra. The ARF represents the telescope's effective area and the RMF gives information about the spectral resolution and how the energy is redistributed on the detector (eROSITA Collaboration, 2024).
The result is one contributing spectrum from each cell based on the respective values of T_e and τ in the cell. To obtain the total spectrum from a specific region, all the spectra S_i attributed to the number of cells i within are first multiplied by the corresponding normalisation factor and then summed up:

$$S_\mathrm{total} = \frac{10^{-14}}{4\pi D^2} \cdot \sum_i EM_i \cdot S_i. \tag{46}$$

Figure 52 shows the synthesised total spectra of Puppis A from models 3.5 and 3.4, as well as the total spectrum extracted from eROSITA X-ray observations by Mayer et al. (2022). Figure 52 was compiled with pyXspec[3], the python implementation of Xspec, which as input takes the spectrum in units of counts per instrument channel. To produce the spectra in units of counts $\mathrm{s}^{-1}\,\mathrm{keV}^{-1}$, the input data are folded with the RMF and the ARF of the corresponding eROSITA observation. However, since the spectra resulting from the simulations were synthesised using the ARF of a smaller representative region of Puppis A with an exposure time of ~ 13.5 ks and the total observed spectrum from Mayer et al. (2022) uses the ARF of the total remnant with an exposure time of ~ 27.9 ks, the simulated spectra were scaled with the ratio of exposure times, so that the absolute flux is comparable to the observed total spectrum. Evidently, both of the synthetic spectra share similarities with the observed spectrum with respect to the spectral shape. The total flux of model 3.4 clearly exceeds the flux of the observed spectrum. In contrast, model 3.5 is a much better fit, especially at higher energies above 0.7 keV. Below 0.7 keV, an excess in counts in the synthetic spectrum is observed, which can most likely be attributed to variations in the absorbing column density and could be fixed by a higher N_H in the model. However, in Sect. 5.3.3, it was shown that the emission measure derived from model 3.5 is lower with respect to the EM derived from the observations by around two orders of magnitude. Curiously, this is not reflected in the fluxes of the spectra,

[3] https://heasarc.gsfc.nasa.gov/docs/xanadu/xspec/python/html/index.html

where model and observed data do not deviate by much. What causes this discrepancy is still unclear. One possible explanation would be that since the EM derived from the observations was corrected for the distance to Puppis A, this might introduce large errors on the measured EM.

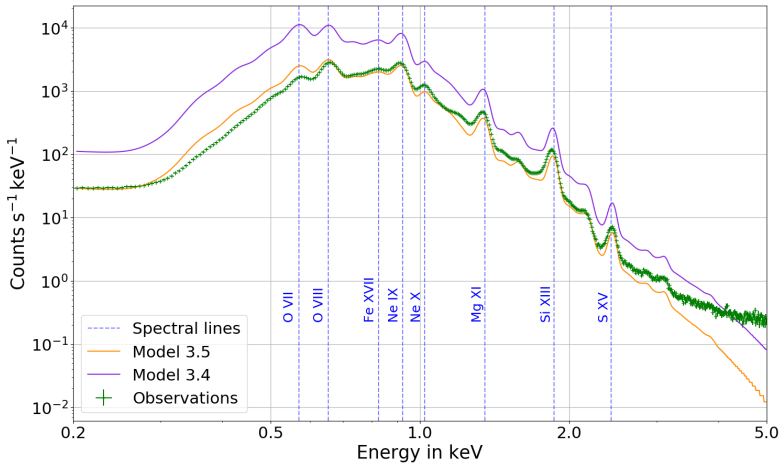

Figure 52: Total X-ray spectra of Puppis A synthesised from models 3.4 (purple) and 3.5 (orange). For comparison, the total spectrum observed with eROSITA together with the identified emission lines, both shown by Mayer et al. (2022) in their Fig. 3, are displayed in green and blue, respectively.

In order to estimate how well the plasma conditions in the simulation can be reconstructed from analysing the simulated spectra, for model 3.5, which is showing the most promising results, four additional spectra are extracted from the regions shown in Fig. 50. The regions were chosen so that two (Regions 1 and 3) represent the brighter features, where the shock is interacting with the cloud, and two are representative of the fainter south-western part of the remnant. All four spectra are then fitted in pyXspec with two different models: the first one is the same model that the synthetic spectra S_i were generated with, namely `tbabs*vnei`. The second model is the one that was used by Mayer et al. (2022) for their spectral analysis of Puppis A, where `vpshock` stands for constant temperature plane-parallel shock plasma model with variable element abundances, which is also a NEI plasma model (again see Borkowski et al. (2001), Hamilton et al. (1983), Borkowski et al. (1994), and Liedahl et al. (1995) for reference). Instead of assuming one single value for the ionisation timescale, the `vpshock` model assumes a distribution of ionisation timescales, implying that the plasma has not all been shocked at the same time. This likely provide a more realistic description of the shocked plasma in SNRs. In the case of both models, the absorbing column density, as well as the abundances for O, Ne, Mg, Si, S, and Fe are freed, similar to Mayer et al. (2022). All the other abundances are fixed to solar abundances using the abundance table by Wilms et al. (2000). The redshift is set to zero. The spectral fits with the `tbabs*vnei` model are shown in Fig. 53 and with the `tbabs*vpshock` model in Fig. 54. The resulting fit parameters for ionisation age and

electron temperature are listed in Table 6. Since regions 1-4 do not directly correspond to any of the regions in Puppis A discussed in Mayer et al. (2022), a quantitative comparison to the real data is hardly possible.
To estimate, how accurate the fitted values for τ and T_e are, they are compared to the corresponding values resulting directly from the simulated data. For that purpose, the mean values weighted with the emission measure from all computational cells located within the respective region are calculated. The results are listed in Table 7. Evidently, the fit parameters do not really agree with what is calculated directly from the simulations, especially in region 1 and 3, where emission from the cloud is present. The fits with both models (`vnei` and `vpshock`) predict a relatively high electron temperature around 1 keV and an ionisation timescale on the order of $\sim 10^{10}\,\mathrm{s\,cm^{-3}}$. The emission measure weighted means calculated directly from the simulated data show the opposite trend, namely a lower electron temperature around 0.2 keV and higher ionisation timescale on the order of $10^{11}\,\mathrm{s\,cm^{-3}}$. However, in general it is possible to fit a spectrum equally well with a high ionisation timescale and low temperature, or the other way around, due to the degeneracy in both of these parameters, which could explain the parameters obtained from the fits in this case. For regions 2 and 4 the parameters are in better agreement between both models and what is obtained directly from the simulations, although the ionisation time scales obtained from the `vpshock` model are higher by one order of magnitude. However, this makes sense, as the `vpshock` model returns the maximum ionisation timescale in the plasma.
Overall, it can be concluded that both the `vnei` and the `vpshock` model return better fit results in regions 2 and 4, where no shocked cloud material is present, which is reasonable as it is difficult to describe several plasma components with a single component model.

	tbabs*vnei		**tbabs*vpshock**	
	kT_e [keV]	τ [$10^{10}\,\mathrm{s\,cm^{-3}}$]	kT_e [keV]	τ_{high} [$10^{10}\,\mathrm{s\,cm^{-3}}$]
R1	1.201 ± 0.025	0.945 ± 0.013	1.000 ± 0.017	2.75 ± 0.05
R2	0.775 ± 0.016	2.75 ± 0.11	0.559 ± 0.011	15.5 ± 0.7
R3	0.714 ± 0.006	1.0238 ± 0.0012	0.663 ± 0.005	2.42 ± 0.04
R4	0.572 ± 0.011	6.2 ± 0.3	0.578 ± 0.011	16.9 ± 1.1

Table 6: Fit parameters for electron temperature and ionization time resulting from fitting the spectra synthesized in regions 1-4.

	kT_e [keV]	τ [10^{10} s cm^{-3}]
R1	0.2240 ± 0.0010	29.22 ± 0.14
R2	0.6528 ± 0.0005	4.604 ± 0.011
R3	0.18278 ± 0.0009	25.33 ± 0.24
R4	0.6713 ± 0.0005	5.200 ± 0.011

Table 7: EM-weighted mean of all computational cell within regions 1-4 for electron temperature and ionization timescale resulting directly from the simulated data.

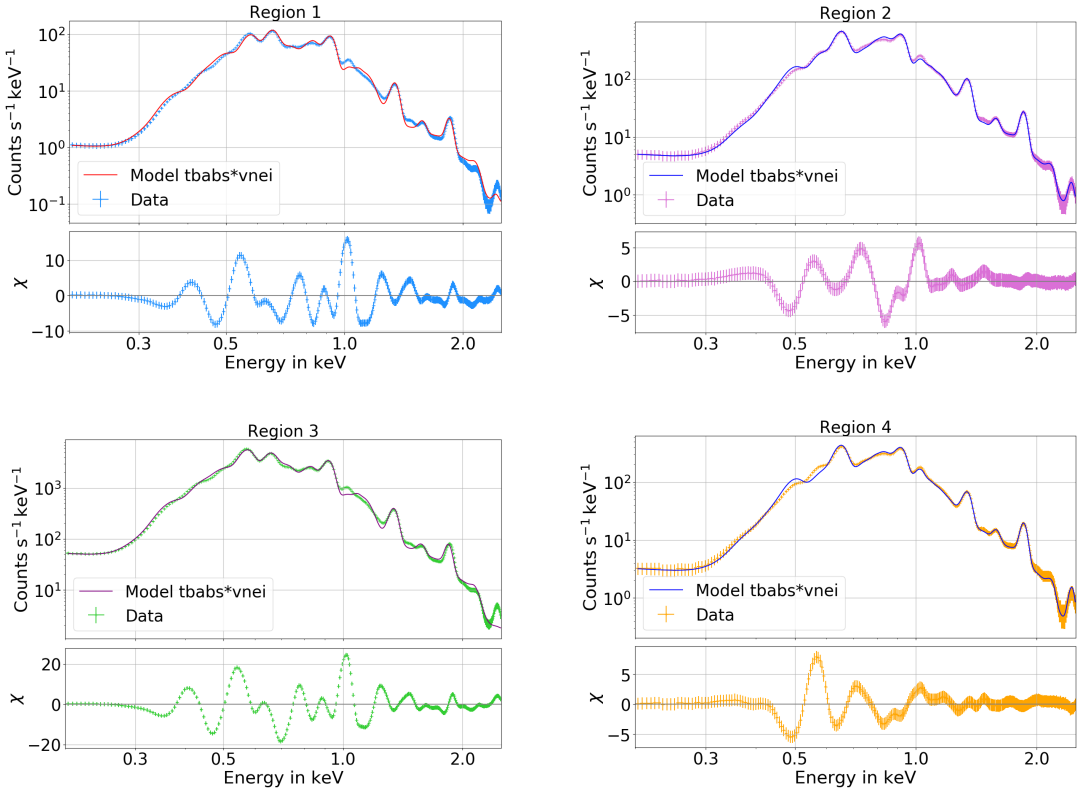

Figure 53: Synthetic X-ray spectra generated from model 3.5 in the regions 1-4 marked in Fig. 50. All spectra were fitted in Xspec with the model `tbabs*vnei`.

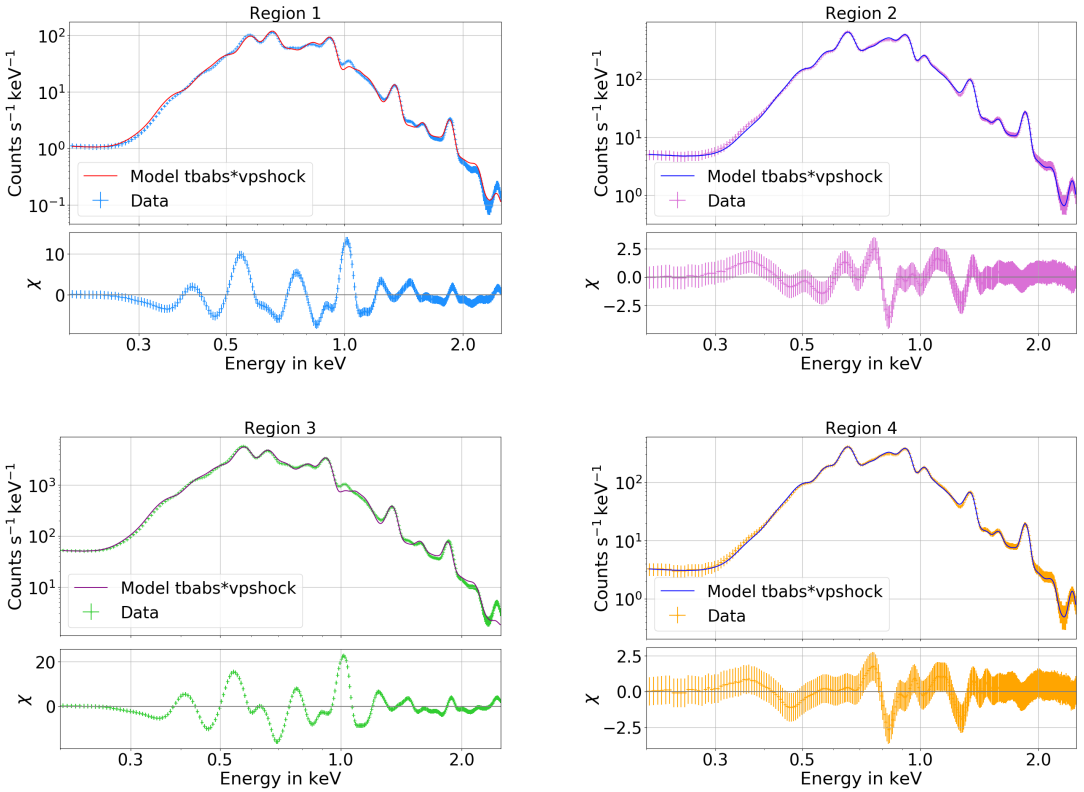

Figure 54: Synthetic X-ray spectra generated from model 3.5 in the regions 1-4 marked in Fig. 50. All spectra were fitted in Xspec with the model `tbabs*vpshock`.

6. Summary and outlook

In this work, a hydrodynamic model of the Galactic core-collapse SNR Puppis A is developed using PLUTO, a numerical code designed by Mignone et al. (2007) for computational astrophysics and fluid dynamics simulations involving flows with high Mach numbers. The aim for the model is to reproduce the observables of Puppis A as best as possible, specifically with respect to the X-ray morphology, to draw conclusions about the explosion parameters of the SN and the structure of the surrounding ISM.
From X-ray observations with the Chandra X-ray observatory and XMM-Newton (Dubner, G. et al., 2013), as well as the eROSITA X-ray telescope (Mayer et al., 2022), it is evident that Puppis A exhibits a very peculiar, almost rectangular shape in X-rays. A similar trend is observed at radio wavelengths (Aruga et al., 2022). In the north-eastern part of the remnant, where a flat border is visible in both X-ray and radio images, Puppis A is believed to be interacting with a compound of atomic and molecular clouds (Aruga et al., 2022).
Based on multi-wavelength observations, the model setup developed in this work consists of a higher density cloud implemented as an elliptical torus at a distance of 10 pc of the spherical ejecta region. Different model geometries are tested throughout this work, as well as different parameters of the SN, such as the kinetic explosion energy, the ISM density, the density distribution in the cloud, and finally the initial pressure in the ejecta region.
Ultimately, the best results are obtained with a kinetic explosion energy of 1.5×10^{51} erg after a simulation time of ~ 5000 yrs. While the explosion energy is consistent with what is found in literature (e.g. Mayer et al. (2022)), the age exceeds the common estimate of ~ 4000 yr. The ejecta mass in the final model setup is fixed to $5\,M_\odot$ and the mass of the surrounding ISM up to a radius of 10.6 pc is normalised to $85\,M_\odot$ based on Mayer et al. (2022). Additionally, a power law density profile $\sim r^{-2}$ is implemented in the ISM to account for the stellar wind of the progenitor. The cloud is described as a partial elliptical torus covering an angle of $\frac{2}{3}\pi$ around the spherical ejecta region. The radial density profile in the ejecta region follows the density profile for core-collapse SNe presented by Chevalier (2005). In both the ejecta and the ISM, random cell-by-cell density variations following Orlando et al. (2012) are superimposed on the respective density profiles to make the simulations more realistic and help hydrodynamical instabilities to form. In the cloud, bigger clumps are implemented with a radius of 5 cells each and a random density distribution within the interval $\rho_0 \cdot 10^{[-2,2]}$, with $\rho_0 \approx 200\,\mathrm{cm}^{-3}$ based on estimates for the cloud density by Aruga et al. (2022).
The resulting X-ray map in the 0.3-10 keV band created from the simulated data resembles the observed X-ray morphology of Puppis A very well, especially with respect to the north-eastern part of the remnant. Most notably, the simulated X-ray map shows a bright feature in the south-east of the remnant, which developed self-consistently in the simulations. A similar feature known as the Bright Eastern Knot is visible in real observations of Puppis A (Hwang et al., 2005). The X-ray morphology in the south-western part of the remnant shows less similarities. In the simulation, the X-ray emission

is relatively uniform, while in the real observations the entire remnant is characterised by brighter filaments. A remarkable resemblance is found between the total observed spectrum and simulated spectrum in the 0.2-5 keV band. Especially at higher energies above 0.7 keV, the spectral shape matches the observations very well. Below 0.7 keV, an excess in counts is found for the synthetic spectrum. However, it is very likely that this is due to variations in the absorbing column density and could be fixed by increasing the n_{H} in the model. Despite the resemblance of the total spectra, recovering the plasma temperature and ionisation time scale from fitting spectra extracted from several smaller regions of the simulated data has proven to be difficult. As of right now, the model is also not able to reproduce the exact plasma conditions as derived from the observations. Even though the electron temperature peaks around 0.7 keV, similar to the observations, the overall temperature range is broader. The same is true for the ionisation timescale. A more extended exploration of the model parameters might be necessary to refine the results.
To further improve the model, one idea would be to first simulate a stellar wind bubble created by the progenitor star. If the SNR evolves within the environment shaped by the wind of a massive star, this would simultaneously raise the emission measure and create the filamentary structures evident in the X-ray images of Puppis A (Martin Krause, priv. conv.). Moreover, moving to MHD simulations might improve the model, as it has been shown that magnetic fields can cause a rectangular morphology in SNRs by Meyer et al. (2022).

Altogether, the current model setup for Puppis A shows very promising results, and even though there is still room for improvement, the model proves that the morphology and the observed spectrum can be approximately recreated by the interaction of the remnant with an atomic and molecular cloud on the north-western side of Puppis A.

References

Arendt, R. G., Dwek, E., Blair, W. P., Ghavamian, P., Hwang, U., Long, K. S., Petre, R., Rho, J., and Winkler, P. F. (2010). Spitzer Observations of Dust Destruction in the Puppis A Supernova Remnant. *Astrophysical Journal*, 725(1):585–597.

Aruga, M., Sano, H., Fukui, Y., Reynoso, E. M., Rowell, G., and Tachihara, K. (2022). Molecular and Atomic Clouds Associated with the Gamma-Ray Supernova Remnant Puppis A. *Astrophysical Journal*, 938(2):94.

Borkowski, K. J., Lyerly, W. J., and Reynolds, S. P. (2001). Supernova Remnants in the Sedov Expansion Phase: Thermal X-ray emission. *Astrophysical Journal*, 548(2):820.

Borkowski, K. J., Sarazin, C. L., and Blondin, J. M. (1994). On the X-Ray Spectrum of Kepler's Supernova Remnant. *Astrophysical Journal*, 429:710.

Chandra X-ray Center (2019). The Clumpy and Lumpy Death of a Star. `https://chandra.harvard.edu/photo/2019/tycho/` [Accessed: 2025-07-06].

Chevalier, R. A. (2005). Young Core-Collapse Supernova Remnants and Their Supernovae. *Astrophysical Journal*, 619(2):839–855.

Dubner, G., Loiseau, N., Rodríguez-Pascual, P., Smith, M. J. S., Giacani, E., and Castelletti, G. (2013). The most complete and detailed X-ray view of the SNR Puppis A⋆. *Astronomy and Astrophysics*, 555:A9.

Dullemond, C. and Springel, V. (2011). Lecture Numerical Fluid Dynamics: Equations of hydrodynamics. `https://www.ita.uni-heidelberg.de/~dullemond/lectures/num_fluid_2011/Chapter_1.pdf` [Accessed: 2025-07-06].

eROSITA Collaboration (2024). eROSITA Data Release 1 Documentation. `https://erosita.mpe.mpg.de/dr1` [Accessed: 2025-07-30]. Max-Planck-Institut für extraterrestrische Physik (MPE).

Greco, E., Miceli, M., Orlando, S., Olmi, B., Bocchino, F., Nagataki, S., Sun, L., Vink, J., Sapienza, V., Ono, M., Dohi, A., and Peres, G. (2022). Additional evidence for a pulsar wind nebula in the heart of sn 1987a from multiepoch x-ray data and mhd modeling. *Astrophysical Journal*, 931(2):132.

Hamilton, A. J. S., Sarazin, C. L., and Chevalier, R. A. (1983). X-ray line emission from supernova remnants. I - Models for adiabatic remnants. *Astrophysical Journal, Supplement*, 51:115–147.

Hwang, U., Flanagan, K. A., and Petre, R. (2005). Chandra X-Ray Observation of a Mature Cloud-Shock Interaction in the Bright Eastern Knot Region of Puppis A. *Astrophysical Journal*, 635(1):355–364.

Katsuda, S., Hwang, U., Petre, R., Park, S., Mori, K., and Tsunemi, H. (2010). Discovery of X-ray-emitting O-Ne-Mg-rich Ejecta in the Galactic Supernova Remnant Puppis A. *Astrophysical Journal*, 714(2):1725–1732.

Katsuda, S., Mori, K., Tsunemi, H., Park, S., Hwang, U., Burrows, D. N., Hughes, J. P., and Slane, P. O. (2008). Discovery of Fast-Moving X-Ray-Emitting Ejecta Knots in the Oxygen-Rich Supernova Remnant Puppis A. *Astrophysical Journal*, 678(1):297–302.

LeVeque, R., Mihalas, D., Dorfi, E., and Müller, E. (1998a). Nonlinear conservation laws and finite volume methods. In *Computational Methods for Astrophysical Fluid Flow*, pages 1–160. Springer Berlin, Heidelberg.

LeVeque, R., Mihalas, D., Dorfi, E., and Müller, E. (1998b). Simulation of astrophysical fluid flow. In *Computational Methods for Astrophysical Fluid Flow*, pages 343–494. Springer Berlin, Heidelberg.

Liedahl, D. A., Osterheld, A. L., and Goldstein, W. H. (1995). New Calculations of Fe L-Shell X-Ray Spectra in High-Temperature Plasmas. *Astrophysical Journal, Letters*, 438:L115.

Mayer, M., Becker, W., Patnaude, D., Winkler, P. F., and Kraft, R. (2020). The Proper Motion of the Central Compact Object RX J0822-4300 in the Supernova Remnant Puppis A, Revisited. *Astrophysical Journal*, 899(2):138.

Mayer, M. G. F., Becker, W., Predehl, P., Sasaki, M., and Freyberg, M. (2022). A global view of shocked plasma in the supernova remnant Puppis A provided by SRG/eROSITA. *Astronomy and Astrophysics*, 661:A31.

McKee, C. F. and Ostriker, J. P. (1977). A theory of the interstellar medium: three components regulated by supernova explosions in an inhomogeneous substrate. *Astrophysical Journal*, 218:148–169.

Meyer, D. M.-A., Velázquez, P. F., Petruk, O., Chiotellis, A., Pohl, M., Camps-Fariña, A., Petrov, M., Reynoso, E. M., Toledo-Roy, J. C., Schneiter, E. M., Castellanos-Ramírez, A., and Esquivel, A. (2022). Rectangular core-collapse supernova remnants: application to Puppis A. *Monthly Notices of the Royal Astronomical Society*, 515(1):594–605.

Mignone, A., Bodo, G., Massaglia, S., Matsakos, T., Tesileanu, O., Zanni, C., and Ferrari, A. (2007). PLUTO: A Numerical Code for Computational Astrophysics. *Astrophysical Journal, Supplement*, 170(1):228–242.

Mignone, A., Zanni, C., Tzeferacos, P., van Straalen, B., Colella, P., and Bodo, G. (2012). The PLUTO Code for Adaptive Mesh Computations in Astrophysical Fluid Dynamics. *Astrophysical Journal, Supplement*, 198(1):7.

Neugebauer, G., Habing, H. J., van Duinen, R., Aumann, H. H., Baud, B., Beichman, C. A., Beintema, D. A., Boggess, N., Clegg, P. E., de Jong, T., Emerson, J. P., Gautier,

T. N., Gillett, F. C., Harris, S., Hauser, M. G., Houck, J. R., Jennings, R. E., Low, F. J., Marsden, P. L., Miley, G., Olnon, F. M., Pottasch, S. R., Raimond, E., Rowan-Robinson, M., Soifer, B. T., Walker, R. G., Wesselius, P. R., and Young, E. (1984). The Infrared Astronomical Satellite (IRAS) mission. *Astrophysical Journal, Letters*, 278:L1–L6.

Orlando, S., Bocchino, F., Miceli, M., Petruk, O., and Pumo, M. L. (2012). Role of Ejecta Clumping and Back-reaction of Accelerated Cosmic Rays in the Evolution of Type Ia Supernova Remnants. *The Astrophysical Journal*, 749(2):156.

Orlando, S., Miceli, M., Pumo, M. L., and Bocchino, F. (2015). Supernova 1987a: A template to link supernovae to their remnants. *Astrophysical Journal*, 810(2):168.

PLUTO Team (2021). PLUTO User's Guide. `https://plutocode.ph.unito.it/userguide.pdf` [Accessed: 2025-02-27].

PLUTO Team (2024). The PLUTO Code. `https://plutocode.ph.unito.it/` [Accessed: 2025-02-07].

Pringle, J. E. and King, A. (2007). The basic fluid equations. In *Astrophysical Flows*, page 1–16. Cambridge University Press.

Reynoso, E. M., Cichowolski, S., and Walsh, A. J. (2016). A high-resolution H i study towards the supernova remnant Puppis A and its environments. *Monthly Notices of the Royal Astronomical Society*, 464(3):3029–3039.

Reynoso, E. M., Green, A. J., Johnston, S., Dubner, G. M., Giacani, E. B., and Goss, W. M. (2003). Observations of the neutral hydrogen surrounding the radio-quiet neutron star RX J0822–4300 in Puppis A. *Monthly Notices of the Royal Astronomical Society*, 345(2):671–677.

Saintonge, A. (2025). The interstellar medium.

Sasaki, M. (2022). *Interstellar Medium Lecture Notes*.

Sato, T., Hughes, J. P., Williams, B. J., and Morii, M. (2019). Genus Statistic Applied to the X-Ray Remnant of SN 1572: Clues to the Clumpy Ejecta Structure of Type Ia Supernovae. *Astrophysical Journal*, 879(2):64.

Sedov, L. I. (1959). *Similarity and Dimensional Methods in Mechanics*.

Seward, F. D. and Charles, P. A. (2010a). Supernova explosions and their remnants. In *Exploring the X-ray Universe*, page 97–122. Cambridge University Press, 2 edition.

Seward, F. D. and Charles, P. A. (2010b). X-ray absorption and scattering in the interstellar medium. In *Exploring the X-ray Universe*, page 51–59. Cambridge University Press, 2 edition.

Truelove, J. K. and McKee, C. F. (1999). Evolution of Nonradiative Supernova Remnants. *Astrophysical Journal, Supplement*, 120(2):299–326.

Ustamujic, S., Orlando, S., Greco, E., Miceli, M., Bocchino, F., Tutone, A., and Peres, G. (2021). Modeling the mixed-morphology supernova remnant IC 443. Origins of its complex morphology and X-ray emission. *Astronomy and Astrophysics*, 649:A14.

Vink, J. (2020). *Physics and Evolution of Supernova Remnants*. Springer International Publishing, Cham.

Wilms, J., Allen, A., and McCray, R. (2000). On the Absorption of X-Rays in the Interstellar Medium. *Astrophysical Journal*, 542(2):914–924.

Winkler, P. F., Tuttle, J. H., Kirshner, R. P., and Irwin, M. J. (1988). Kinematics of Oxygen-Rich Filaments in Puppis A. In Roger, R. S. and Landecker, T. L., editors, *IAU Colloq. 101: Supernova Remnants and the Interstellar Medium*, page 65.

Wolschin, G. (2021). Astrophysikalische Hydrodynamik. In *Hydrodynamik*, pages 149–158. Springer Berlin Heidelberg, Berlin, Heidelberg.

A. Acknowledgements

First and foremost I would like to thank my supervisor, Manami Sasaki, for making this work and the collaboration with the observatory in Palermo possible, as well as for all the advice and support provided throughout the last few months/years.
Second of all, I want to express special thanks to Salvatore Orlando and Marco Miceli at the INAF Osservatorio Astronomico di Palermo for introducing me to PLUTO and providing the tools to create the X-ray maps, X-ray spectra, and histograms, as well as their general help, input, and support, especially during the three months I spent in Palermo working on this project. Thank you also to everyone else at the observatory in Palermo, who made this time really special for me.
Many thanks to Martin Mayer for the help and input from an observer's point of view and for providing the figures and data that were used to compare the simulation results to the eROSITA X-ray observations of Puppis A. On that note, a big thank you to everyone else at Remeis for the lovely working environment. I also want to thank Martin Krause (University of Hertfortshire) for his input on some of the simulation results.
Last but not least, thank you to my family (in particular: Mama, Papa und Simon) and friends for the ongoing support and proof reading, and especially to Martin for the coffee shop writing sessions (and everything else ;)), to Anna for making sure I actually get some work done all the way from Potsdam, and to Nora for being my language editor.

We acknowledge the SCAN HPC facility of INAF-Osservatorio Astronomico di Palermo for the availability of high performance computing resources and support.
This research has made use of data and/or software provided by the High Energy Astrophysics Science Archive Research Center (HEASARC), which is a service of the Astrophysics Science Division at NASA/GSFC.
The research leading to these results has received funding from the European Union's Horizon 2020 Programme under the AHEAD2020 project (grant agreement n. 871158).

B. Appendix

B.1. 3D Model 1

$5\,M_\odot$, 1×10^{51} erg, no radiative losses

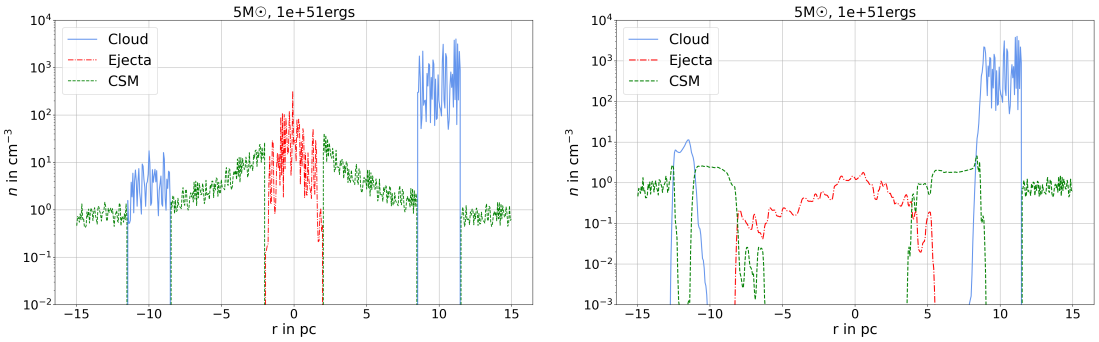

Figure 55: Initial (left) and final (right) density profiles. The simulation was run for ~ 4000 yrs.

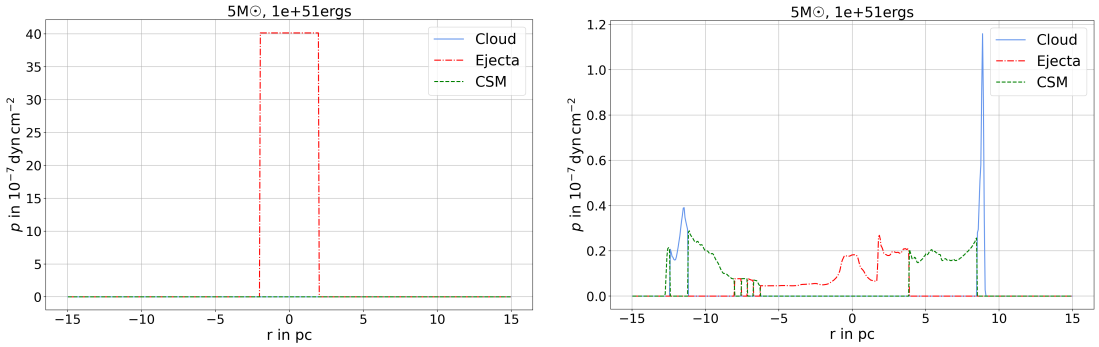

Figure 56: Initial (left) and final (right) pressure profiles. The simulation was run for ~ 4000 yrs. Blue, green and red mark the regions, where the respective tracer for cloud, CSM, and ejecta is >0.9.

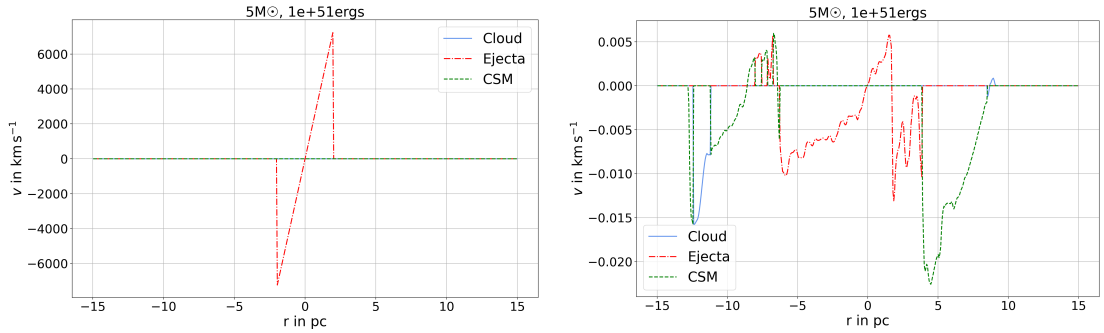

Figure 57: Initial (left) and final (right) velocity profiles. The simulation was run for ~ 4000 yrs. Blue, green and red mark the regions, where the respective tracer for cloud, CSM, and ejecta is >0.9.

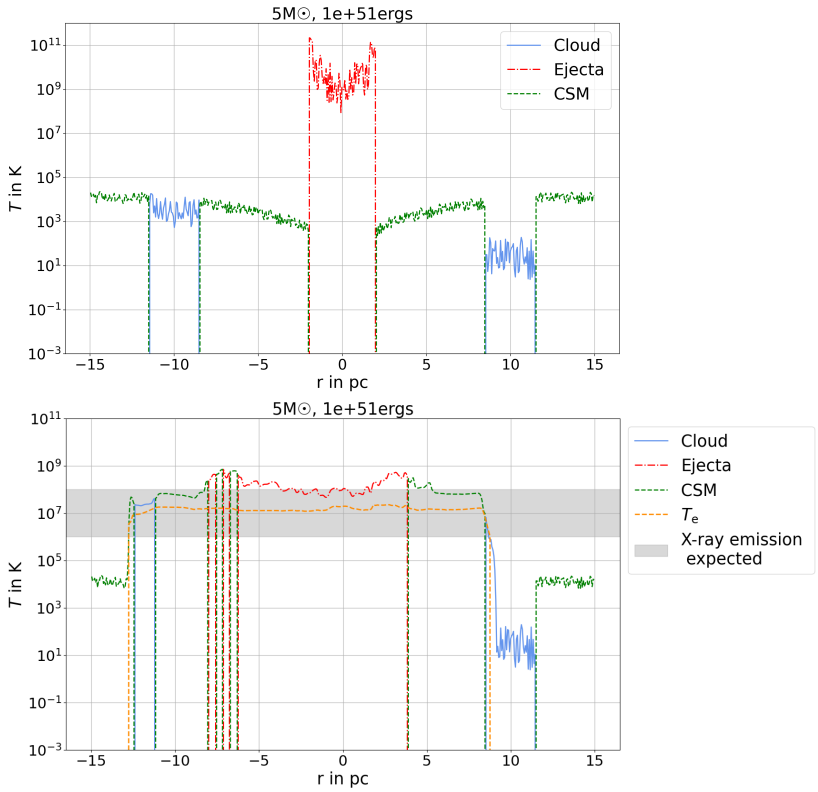

Figure 58: Initial (left) and final (right) temperature profiles. The simulation was run for ~ 4000 yrs. Blue, green and red mark the regions, where the respective tracer for cloud, CSM, and ejecta is >0.9. The shaded area marks the temperature range, in which thermal X-rays are expected.

$5\,M_\odot$, 1×10^{51} erg, with radiative losses

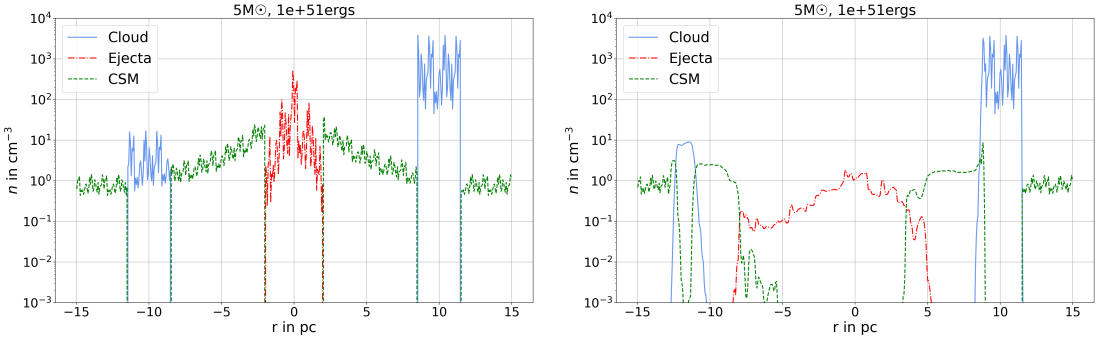

Figure 59: Initial (left) and final (right) density profiles. The simulation was run for $\sim 4000\,\mathrm{yrs}$.

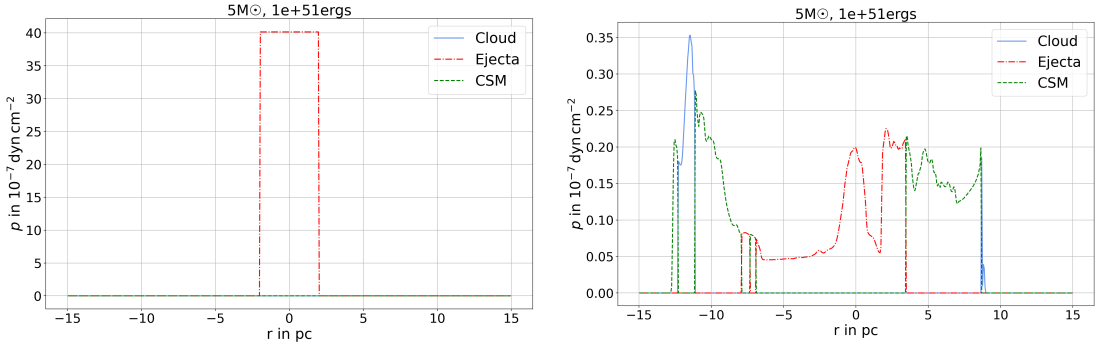

Figure 60: Initial (left) and final (right) pressure profiles. The simulation was run for $\sim 4000\,\mathrm{yrs}$. Blue, green and red mark the regions, where the respective tracer for cloud, CSM, and ejecta is >0.9.

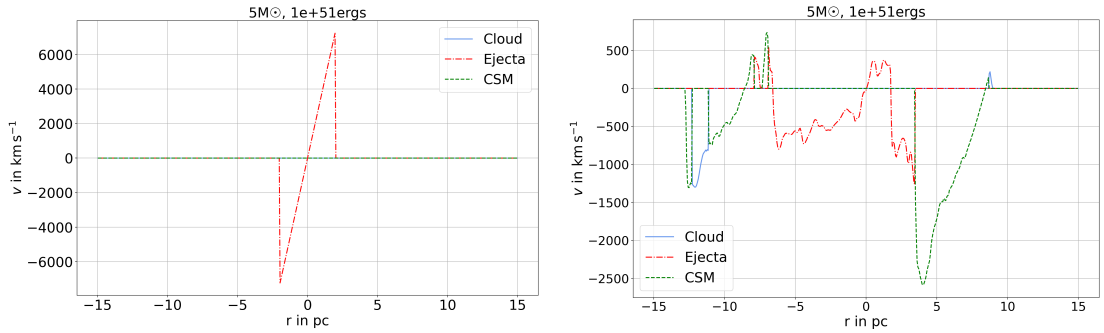

Figure 61: Initial (left) and final (right) velocity profiles. The simulation was run for ~ 4000 yrs. Blue, green and red mark the regions, where the respective tracer for cloud, CSM, and ejecta is >0.9.

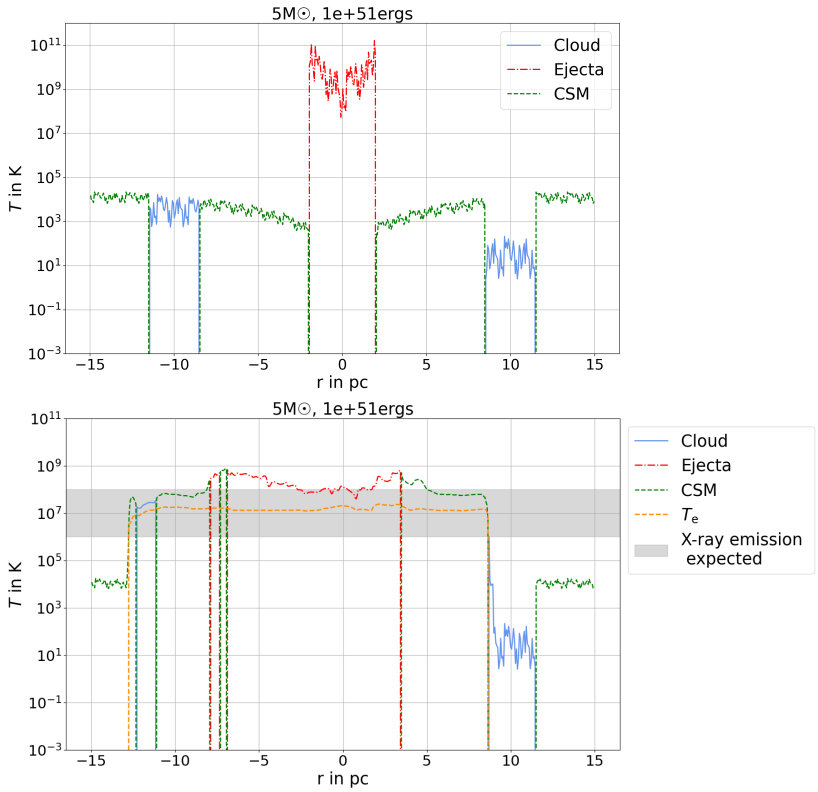

Figure 62: Initial (left) and final (right) temperature profiles. The simulation was run for ~ 4000 yrs. Blue, green and red mark the regions, where the respective tracer for cloud, CSM, and ejecta is >0.9. The shaded area marks the temperature range, in which thermal X-rays are expected.

B.2. 3D Model 2

$5\,M_\odot$, 1×10^{51} erg, with radiative losses

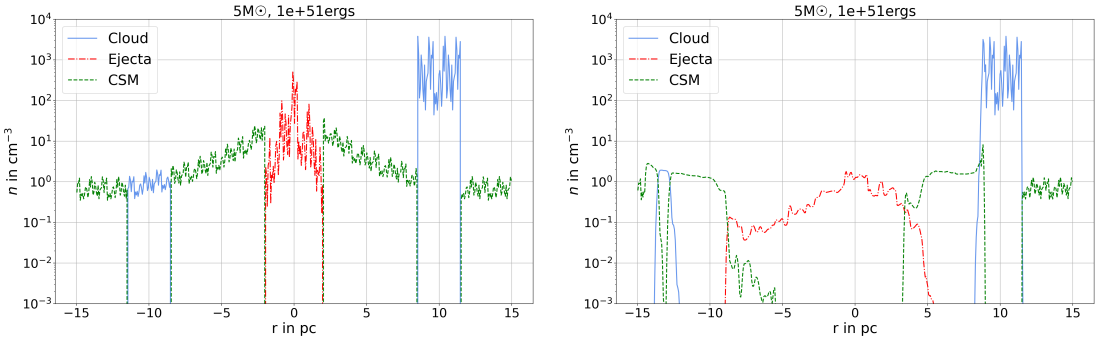

Figure 63: Initial (left) and final (right) density profiles. The simulation was run for $\sim 4000\,\mathrm{yrs}$.

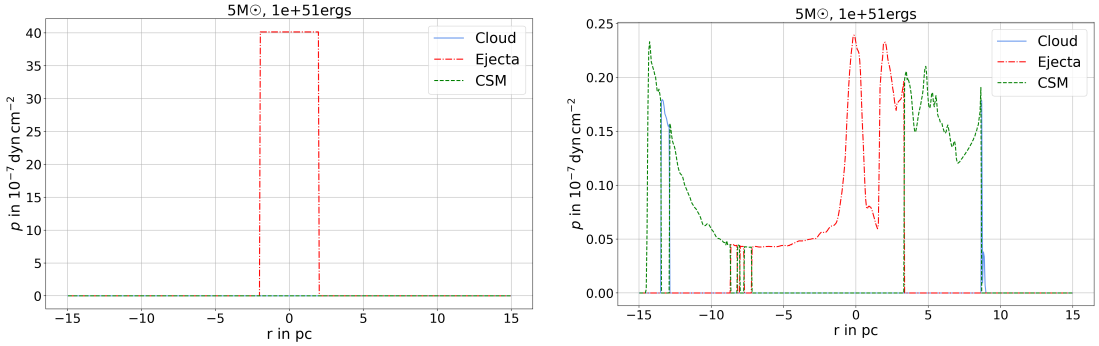

Figure 64: Initial (left) and final (right) pressure profiles. The simulation was run for $\sim 4000\,\mathrm{yrs}$. Blue, green and red mark the regions, where the respective tracer for cloud, CSM, and ejecta is >0.9.

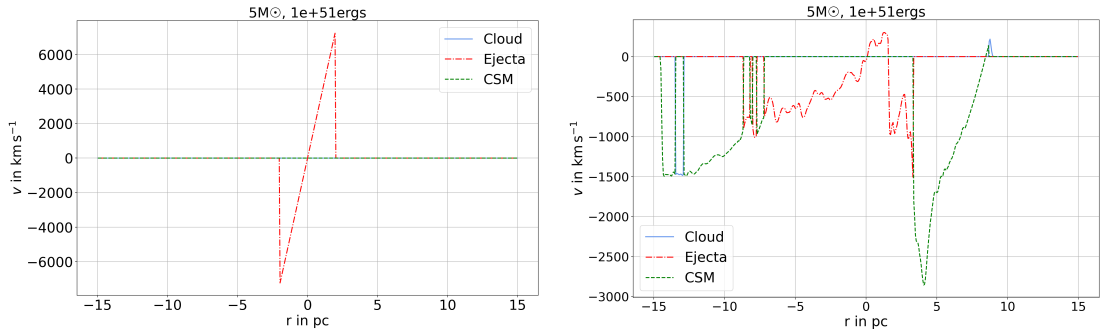

Figure 65: Initial (left) and final (right) velocity profiles. The simulation was run for ~ 4000 yrs. Blue, green and red mark the regions, where the respective tracer for cloud, CSM, and ejecta is >0.9.

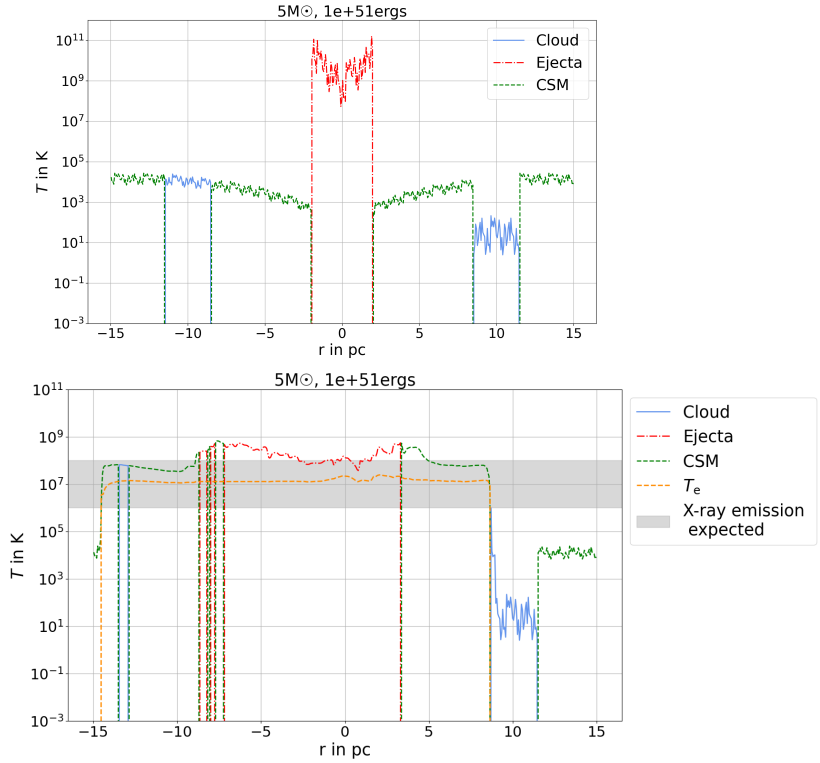

Figure 66: Initial (left) and final (right) temperature profiles. The simulation was run for ~ 4000 yrs. Blue, green and red mark the regions, where the respective tracer for cloud, CSM, and ejecta is >0.9. The shaded area marks the temperature range, in which thermal X-rays are expected.

B.3. 3D Model 3

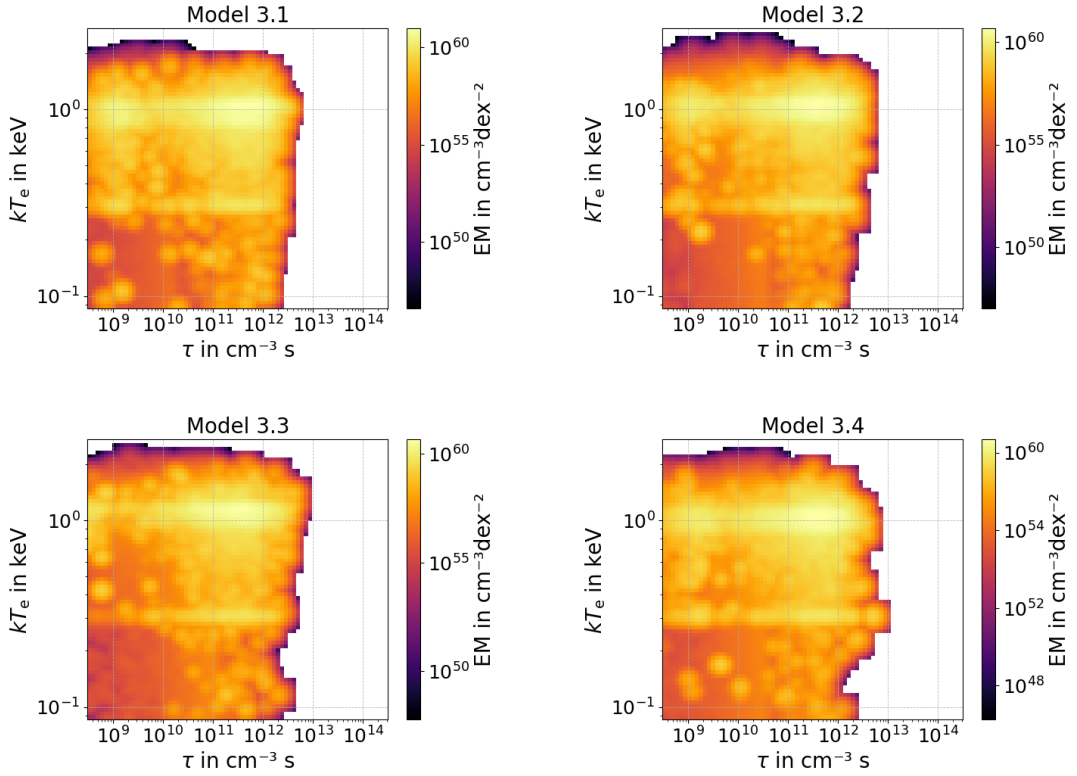

Figure 67: Histograms of the logarithmic distribution of emission measure EM with respect to the ionisation timescale τ and electron temperature kT_e for model model versions 3.1 (top left), 3.2 (top right), 3.3 (bottom left), and 3.4 (bottom right).

5 $M_\odot$, 1.5 $\times$ 10^{51} erg, with radiative losses

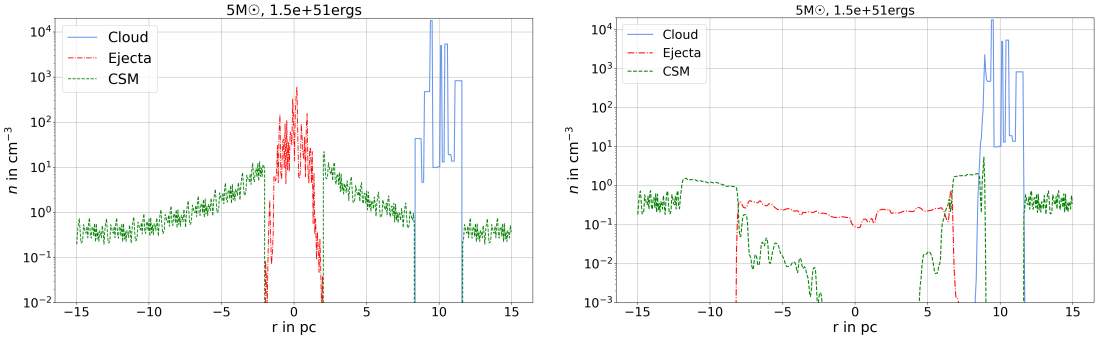

Figure 68: Initial (left) and final (right) density profiles. The simulation was run for $\sim$ 5000 yrs.

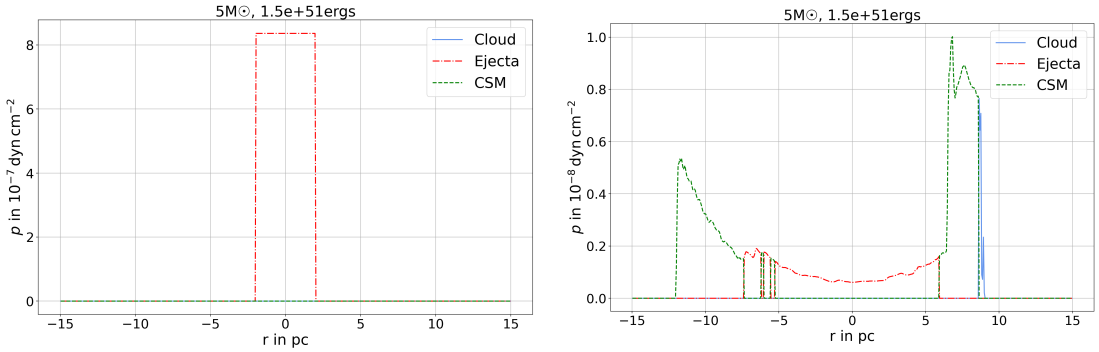

Figure 69: Initial (left) and final (right) pressure profiles. The simulation was run for $\sim$ 5000 yrs. Blue, green and red mark the regions, where the respective tracer for cloud, CSM, and ejecta is >0.9.

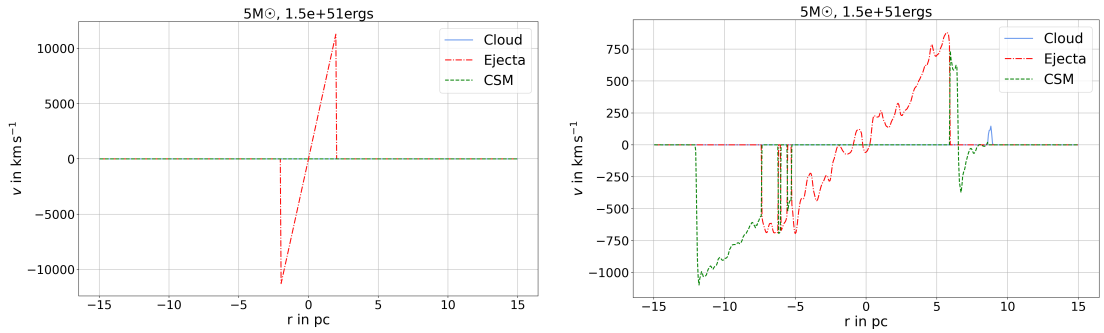

Figure 70: Initial (left) and final (right) velocity profiles. The simulation was run for ~ 5000 yrs. Blue, green and red mark the regions, where the respective tracer for cloud, CSM, and ejecta is >0.9.

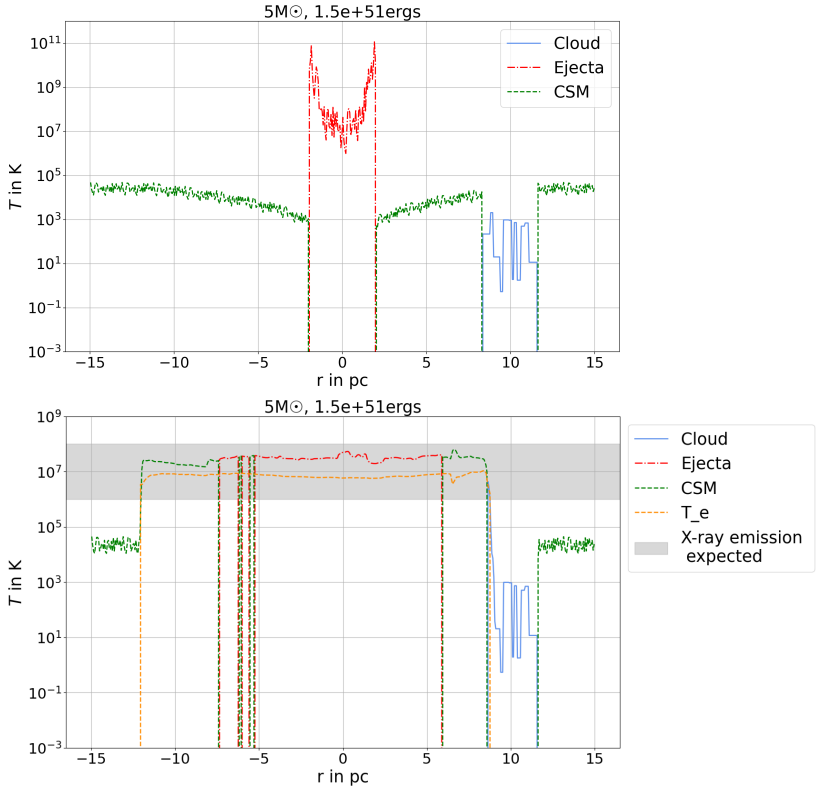

Figure 71: Initial (left) and final (right) temperature profiles. The simulation was run for ~ 5000 yrs. Blue, green and red mark the regions, where the respective tracer for cloud, CSM, and ejecta is >0.9. The shaded area marks the temperature range, in which thermal X-rays are expected.

C. Eigenständigkeitserklärung

Hiermit versichere ich, Marie Prucker (22514548), die vorgelegte Arbeit selbstständig und ohne unzulässige Hilfe Dritter sowie ohne die Hinzuziehung nicht offengelegter und insbesondere nicht zugelassener Hilfsmittel angefertigt zu haben. Die Arbeit hat in gleicher oder ähnlicher Form noch keiner anderen Prüfungsbehörde vorgelegen und wurde auch von keiner anderen Prüfungsbehörde bereits als Teil einer Prüfung angenommen. Die Stellen der Arbeit, die anderen Quellen im Wortlaut oder dem Sinn nach entnommen wurden, sind durch Angaben der Herkunft kenntlich gemacht. Dies gilt auch für Zeichnungen, Skizzen, bildliche Darstellungen sowie für Quellen aus dem Internet. Mir ist insbesondere bewusst, dass die Nutzung künstlicher Intelligenz verboten ist, sofern diese nicht ausdrücklich als Hilfsmittel von dem Prüfungsleiter bzw. der Prüfungsleiterin zugelassen wurde. Dies gilt insbesondere für Chatbots (insbesondere ChatGPT) bzw. allgemein solche Programme, die anstelle meiner Person die Aufgabenstellung der Prüfung bzw. Teile derselben bearbeiten könnten. Verstöße gegen die o.g. Regeln sind als Täuschung bzw. Täuschungsversuch zu qualifizieren und führen zu einer Bewertung der Prüfung mit „nicht bestanden“.

Ort, Datum	Marie Prucker